8-2012

Formation and Alteration of Basaltic Soils on Mars

Ian Oliver McGlynn
imcglynn@utk.edu

To the Graduate Council:

I am submitting herewith a dissertation written by Ian Oliver McGlynn entitled "Formation and Alteration of Basaltic Soils on Mars." I have examined the final electronic copy of this dissertation for form and content and recommend that it be accepted in partial fulfillment of the requirements for the degree of Doctor of Philosophy, with a major in Geology.

Christopher M. Fedo and Harry Y. McSween, Jr., Major Professor

We have read this dissertation and recommend its acceptance:

Jeffrey E. Moersch, Carol P. Harden

Accepted for the Council:

Carolyn R. Hodges

Vice Provost and Dean of the Graduate School

(Original signatures are on file with official student records.)

Formation and Alteration of Basaltic Soils on Mars

A Dissertation Presented for the
Doctor of Philosophy
Degree
The University of Tennessee, Knoxville

Ian Oliver McGlynn
August 2012

Acknowledgements

Results from this research have only been possible with the guidance, support, and patience of my co-advisors Dr. Christopher M. Fedo and Dr. Harry Y. McSween, Jr. I am immensely grateful for the opportunity they have provided to explore the desolate and arid plains of Mars with the twin Mars Exploration Rovers Spirit and Opportunity. I am also grateful to the committee members, Dr. Jeffrey E. Moersch and Dr. Carol P. Harden, whose time and effort has improved the quality of this dissertation. I am grateful to the MER operations and development trams and to the scientists and engineers at NASA and JPL who sent two explorers out into the unknown. Specific contributions were provided from the following individuals: D. M. Burr (Tennessee), R. Gellert (Guelph), K. E. Herkenhoff (USGS), O. Karahayit (OSU), R. Li (OSU), H. W. Nesbitt (Western Ontario), A. Patchen (Tennessee), A. D. Rogers (Stony Brook), E. Simpson (Kutztown), and R. J. Sullivan (Cornell).

To Karina my martian partner in crime, thank you for keeping the wonder and enthusiasm. We walk upon a world not of our own and ponder the differences, yet it is the similarities that are most striking. Wispy clouds high above in an atmosphere so thin and fragile, against a brilliant sky with a billion stars looking down, and grains of sand roll steadily in the breeze. Let's dream and explore together. I am forever indebted for the enduring support from family through the long days and nights, for kindling the spark and sustaining the ambition. Finally, I am appreciative for the mentorship of Dr. Gregory S. Okin (UCLA), Dr. John M. Hanchar (MUN), and Dr. Lin H. Chambers (NASA LaRC) who showed the way forward.

Abstract

The current surface of Mars is an arid inhospitable environment, dominated by aeolian processes, composed of largely volcanic rocks that have little apparent indication of pervasive aqueous chemical weathering, and blanketed by dust. Rocks are composed of basalts and the "soil" sediments appear to be largely basaltic-derived, and are chemically similar on a global scale. If the climate was once warmer and wetter during the Noachian period, with environmental conditions favorable to the development of life, physically weathered remnants, such as large quantities of phyllosilicate minerals, should remain. Basaltic soils provide a crucial constraint on chemical and physical weathering processes, and are critical for determining the environmental and climatic history of Mars. To understand the origin of sediments, this dissertation investigated the (1) textures of sedimentary grains at Gusev Crater, (2) the chemical and mineral compositions of sediments at the Mars Exploration Rover landing sites in Meridiani Planum and Gusev Crater, and evaluated the potential chemical alteration from weathering, and (3) applied mineral fractionation experiments of analog basalt sediment with implications for interpreting the sorting of sediments on Mars. Textural results indicate that soils are continuously transported and modified by aeolian conditions, and originate primarily from comminuted impacted bedrock. Soil chemical compositions resemble unaltered basalt but mixing of sulfates and phyllosilicates is permissible. Comminuted and grain size sorted basalt analog sediments demonstrate the potential for significant compositional variations imposed by hydrodynamic sorting, an important determinant of soil compositions on Mars. Combined, these results show that soils on Mars are heterogeneous mixtures of comminuted locally derived rocks that have been minimally altered by chemical weathering from olivine dissolution, and are mixed with dust containing older phyllosilicates and sulfates.

Table of Contents

List of Tables

List of Figures

Chapter 2

Chapter 3

Chapter 4

Chapter 1

Introduction

1. Soil Sediments on Mars

Soils on the surface of Mars reside at the confluence of the lithosphere, atmosphere, hydrosphere, and potential biosphere, and the composition of soils reflects the contribution and interactions between each system. The surface of Mars, however, has not been static. Instead, dramatic shifts in climate have altered the interactions of each system [Bibring et al., 2006]. The early history of Mars known as the Noachian is broadly characterized by a period of cataclysmic high-intensity meteorite impacts [Head, 2001] and coincides with geomorphic evidence [Howard et al., 2005; Grant et al., 2010] of ancient river channels and stream networks that are now dry, widely seen as an indication of early stable and persistent liquid water [Malin and Edgett, 2003]. Clay minerals have been detected in deposits of this age [Poulet et al., 2005]. Cold arid conditions followed in the Hesperian period, marking a dramatic shift in the surface environment away from a stable hydrologic system and characterized by sulfate deposits from large-scale volcanic outgasing [Bibring et al., 2006]. For the past 3 billion years, the Amazonian period has been an arid, inhospitable landscape, far removed from the warm and wet conditions of the past.

The term “soil” in planetary geology is important, because it refers to the upper layer of unconsolidated regolith of rock fragments and comprises any possible additional components, regardless of composition or origin, including the deposition of fine grained (silt-sized) dust, volcaniclastic material, aeolian deposits from ripples or dunes, and clay minerals. Such a definition differs from the traditional soil science usage that includes the implied presence of organics that should not be implied for sediment on Mars.

Data returned from the Mars Exploration Rovers Spirit in Gusev Crater and Opportunity in Meridiani Planum provide an unprecedented level of detail from which to explore the surface of Mars and examine the origin, composition, and alteration of soils. If Mars' history parallels the Earth's in any way, then the composition of soil sediments from the early cataclysmic period that gave way to calmer times, should record the alteration effects of water that may have been present. This dissertation, broken into four parts, attempts to survey soils on Mars at the Mars Exploration Rover landing sites, to understand their origin, textures, compositions, and origin, as well as to characterize any alteration of soil sediments.

2. Mechanisms of Sediment Production

Chapter two presents a textural characterization of sediments at Gusev Crater, and the interpretation of soil comminution and transport by physical processes, and presents a new model for soil generation. Soil sediments are generated by physical interactions from meteorite impacts and aeolian abrasion, and by chemical interactions [Squyres et al., 2004; Grotzinger et al., 2011]. However, the influence of physical processes likely overwhelms any chemical effects. A large volume of sediment has been generated, possibly during a period that experienced a high rate of impacts necessary to generate sediment [Knauth et al., 205]. After basaltic bedrock was shattered by impacts, brecciated material became available for aeolian abrasion and subsequent transport. Brecciated units have been found at the MER landing sites including all the craters at Meridiani Plaum [Squyres et al., 2004] and as a sedimentary unit of transported impact material in Mawrth Vallis [Grotzinger et al., 2011]. Chemical processes are also implied from the presence of vugs imaged by the MER Microscopic Imager and located on rock surfaces formed

by sulfate dissolution [Squyres et al., 2004], but the magnitude of such processes must be evaluated.

3. Composition and Alteration of Sediment

Chapter three introduces normative mineralogy estimates of soils for both landing sites. It also integrates soil compositions with textures (from chapter 2) at Gusev Crater to evaluate the potential for compositional modification by chemical alteration. This chapter also explores the potential for compositional controls imposed by sorting, which has not been thoroughly investigated previously. Before the extent of chemical weathering can be considered, understanding the composition of sediments is required. Basalts are typically comprised of olivine, pyroxene, plagioclase, glass, and secondary minerals. The mineral composition of rocks can be estimated from chemistry using a normative approach, which assumes a series of idealized conditions, and generally approximates mineral proportions in rocks [McSween et al., 1999, 2006]. However sediment on the surface may not simply contain primary igneous minerals, but also include components from mixing by wind or other forms of compositional modification. Soils are also rich in SO_3 which correlates with an increase in Cl from volcanic outgassing [Yen et al., 2005] or evaporate salts [Squyres et al., 2004] that occurred earlier in the planet's history [Bibring et al., 2006]. Low concentrations of Ni have been interpreted as an addition of chondritic material (1 to 3 %) to soil compositions [Yen et al., 2005]. When combined with textural data, the competing forces of chemical weathering and physical sorting can be determined.

A comparison of the weathering pathways of terrestrial sediment with MER sediment provides a common perspective to explore sedimentary conditions on Mars. However, differences in sedimentary material, sediment production, environmental conditions, and sediment cycles between Earth and Mars are stark. Sediments on Mars are derived from basalt bedrock [McSween et al., 2010], unlike terrestrial sediment that, on global scale, is commonly derived from felsic continental crustal rocks [McLennan, 1993]. Sediment production on Mars is primarily initiated by bolide impacts, whereas terrestrial sediments are generated by chemical and physical weathering [Barlow, 2010]. Environmental conditions on the current surface of Mars are inhospitable, yet evidence of liquid water at the MER landing sites has been reported in the form of cross bedding, aqueous products, and hematite concretions [Christensen et al., 2004; Klingelhöfer et al. 2004; Squyres et al., 2004]. In contrast, abundant concentrations of olivine in martian rocks and soils [McSween et al., 2008, 2010], a mineral that reacts in the presence of water [Hausrath et al., 2008], indicate that the persistence of water was limited. Instead, acidic high-sulfur conditions [stable pH = 2.5 to 4.5; Olsen and Rimstidt, 2007], as suggested by the detection of jarosite [Klingelhöfer et al., 2004], may produce a distinct weathering pathway [Tosca et al., 2004; Hurowitz and McLennan, 2007]. Finally, without active plate tectonics, the volume of sediments has accumulated over time. An evaluation of soil sediment compositions linked with textures is needed to ascertain the potential extent of chemical weathering and to explore the importance of physically-induced changes in the martian sedimentary system.

4. Aeolian Reworking and Sorting

Chapter four presents further refinement of compositional modification controls from physical processes on terrestrial basaltic sediment analogs which are used to simulate the effects of comminution and sorting, with implications for interpreting the chemistry and mineralogy of planetary surfaces. Evidence of ripples [Sullivan et al. 2008], sandblasted surfaces [Greeley et al., 2004; Sullivan et al., 2005], winnowed bedform surfaces [Yen et al., 2005], and rounded grains [Sullivan et al., 2008] all indicate that aeolian processes have been present at many sites on Mars, and that the transport of sand-sized grains is feasible [Kok, 2010; Bridges et al., 2012]. Due to the overwhelming evidence of physical activity, the potential compositional effects resulting from selective sorting must be considered to accurately characterize the formation and alteration of sediments on Mars. Hydrodynamic sorting has been well documented in terrestrial studies [Nesbitt and Young, 1996; Young and Nesbitt, 1998; Fralick, 2003], resulting in density mineral separation and forming sedimentary layers with compositions distinct from the original source rock, all without chemical alteration. Given that sediments are available to be transported and that transport processes have been active, it is then reasonable to expect that compositional modification of sediments from mineral fractionation must play a role in the resulting sediment compositions.

5. Implications of Results

Views of the surface environments on Mars have been interpreted from the chemistry and mineralogy and from the inferred processes that alter surface materials. Years of *in situ* surface observations by the MER rovers and numerous remote-sensing platforms [Murchie et al., 2009;

Ehlmann et al., 2011] have provided significant insights into the composition and properties of surface rocks and conditions. However, basic constraints on the composition, formation, and alteration history of surface soils have largely not been addressed. The purpose of the conducted research has been to enhance the scientific return from the Mars Exploration Rover missions by introducing new methods of interpreting geochemical analyses of soils, and to study more complete models of soil formation. The principal chemical components of Martian soils were identified and used to explore implications of Martian weathering processes and petrology of the Martian crust. The research attempts to better interpret past environmental conditions on Mars by classifying major sediment "soil" types from their chemical compositions and textures and by placing their formation in a process-driven framework, identifying major constituent components that improve the NASA objective in understanding of the processes and history of climate on Mars. Soil composition cannot be examined in isolation without consideration of textural properties that are affected by alteration mechanisms of soil formation. This has been the first study to perform a detailed textural analysis of the soils, and the first study to examine complex linkages in chemical composition and grain size distributions meeting NASA's objective to determine the evolution of the surface of Mars. Critical insights into soil formation from basalt weathering have been used to interpret current and past environments, specifically from the identification of global heterogeneous soil types that are the product of weathering from chemically distinct parent material, and unique alteration conditions, such as pH and the availability of water, crucial for evaluating the biological viability and the variability of climate of Mars.

References

Barlow, N. G. (2010), What we know about Mars from its impact craters, *Geol. Soc. Am. Bull., 57*, 1338–1345, doi:10.1016/j.pss.2009.06.006.

Bibring, J. P., Langevin, Y., Mustard, J. F., et al. (2006), Global mineralogical and aqueous mars history derived from OMEGA/Mars express data, *Science, 312*, 400-404, doi:10.1126/science.1122659.

Bridges, N. T., Bourke, M. C., Geissler, P. E., et al. (2012), Planet-wide sand motion on Mars. *Geology, 40*, 31-34, doi:10.1130/G32373.1.

Christensen, P. R., et al. (2004), Mineralogy at Meridiani Planum from the Mini-TES experiment on the Opportunity Rover, *Science, 306*, 1733–1739, doi:10.1126/science.1104909.

Ehlmann, B. L., Mustard, J. F., Murchie, S. L., et al. (2011), *Nature, 479*, 53-60, doi:10.1029/2009je003339.

Fralick, P. W. (2003), Geochemistry of clastic sedimentary rocks: ratio techniques. In ed. D. Lentz, *Geochemistry of Sedimentary Rocks*. Geol. Assoc. Can.

Greeley, R., Squyres, S.W., Arvidson, R.E., et al. (2004), Wind-related processes detected by the Spirit rover at Gusev Crater, Mars. *Science. 305*, 810-813, doi:10.1126/science.1100108.

Grotzinger, J.P., Beaty, D., Dromat, G. et al., (2011), The sedimentary record of Mars. *The Sed. Rec.*, *9*, 4-8, doi:10.2110/sedred.2011.2.

Hausrath, E. M., Navarre-Sitchler, A. K., Sak, P. B., et al. (2008), Basalt weathering rates on Earth and the duration of liquid water on the plains of Gusev Crater, Mars, *Geology, 36*, 67-70, doi: 10.1130/g24238a.1.

Hurowitz, J. A. and McLennan, S. M. (2007), A ~3.5 Ga record of water-limited, acidic weathering conditions on Mars. *Earth Planet. Sc. Lett. 260*, 432-443, doi:10.1016/j.epsl.2007.05.043.

Howard, A. D., Moore, J. M., and Irwin, R. P. (2005), An intense terminal epoch of widespread fluvial activity on early Mars: 1. Valley network incision and associated deposits, *J. Geophys. Res., 110*(E12).

Klingelhöfer, M., et al. (2004), Jarosite and hematite at Meridiani Planum from Opportunity's Mossbauer spectrometer, *Science, 306*, 1740–1745, doi:10.1126/science.1104653.

Kok, J. F. (2010), Difference in the wind speeds required for initiation versus continuation of sand transport on Mars: Implications for dunes and dust storms, *Phys. Rev. Lett. 104*, 074502, doi:10.1103/PhysRevLett.104.074502.

Malin, M. C. and Edgett, K. S. (2003), Evidence for persistent flow and aqueous sedimentation on early Mars, *Science, 302*, 1931-1934.

McLennan, S. M. (1993), Weathering and global denudation, *J. Geol., 101*, 295-303.

McSween, H. Y., Murchie, S. L., Crisp, J. A. et al. (1999), Chemical, multispectral, and textural constraints on the composition and origin of rocks at the Mars Pathfinder landing site, *J. Geophys. Res, 104*(E4), 8679-8715.

McSween, H. Y., Wyatt, M.B., Gellert. R., et al. (2006), Characterization and petrologic interpretation of olivine-rich basalts at Gusev Crater, Mars. *J. Geophys. Res. 111*, E02S10, doi:10.1029/2005JE002477.

McSween H. Y., Ruff, S.W., Morris, R.V., et al. (2008), Mineralogy of volcanic rocks in Gusev Crater, Mars: Reconciling Mossbauer, Alpha Particle X-ray Spectrometer, and Miniature Thermal Emission Spectrometer spectra. *J. Geophys. Res. 113*, E06S04, doi:10.1029/2007JE002970.

McSween, H.Y., McGlynn, I.O., and Rogers, A.D., (2010), Determining the modal mineralogy of Martian soils, *J. Geophys. Res. 115*, E00F12, doi:10.1029/2010JE003582.

Murchie, S. L., Mustard, J. F., Ehlmann, B. L., et al. (2009), A synthesis of Martian aqueous mineralogy after 1 Mars year of observations from the Mars Reconnaissance Orbiter, *J. Geophys. Res. 114*, E00D06, doi: 10.1029/2009je003342.

Nesbitt, H. W. and Young, G.M. (1996), Petrogenesis of sediments in the absence of chemical weathering: Effects of abrasion and sorting on bulk composition and mineralogy. *Sedimentology. 43*, 341-358, doi:10.1046/j.1365-3091.1996.d01-12.x.

Olsen, A. A. and Rimstidt, J. D. (2007), Using a mineral lifetime diagram to evaluate the persistence of olivine on Mars, *Am. Min., 92*, 598-602.

Poulet, F., Bibring, J. P., Mustard, J. F., et al. (2005), Phyllosilicates on Mars and implications for early martian climate, *Nature, 438*, 623-627.

Squyres, S. W., Arvidson, R. E., Bell, J. F., et al. (2004), The Spirit Rover's Athena Science Investigation at Gusev Crater, Mars, *Science, 305*, 794-799

Squyres, S. W., Arvidson, R. E., Ruff, S. (2008), Detection of silica-rich deposits on Mars, *Science, 320*, 1063-1067, doi:10.1126/science.1155429.

Sullivan, R., Banfield, D., Bell., J. F., et al. (2005), Aeolian processes at the Mars Exploration Rover Meridiani Planum landing site, *Nature, 436*, 58–61, doi:10.1038/nature03641.

Sullivan, R., Arvidson, R. Bell, J. F., et al. (2008), Wind-driven particle mobility on mars: Insights from Mars Exploration Rover observations at "El Dorado" and surroundings at Gusev Crater. *J. Geophys. Res. 113*, E06S07, doi:10.1029/2008JE003101.

Tosca, N. J., McLennan, S. M. Lindsley, D. H. et al. (2004), Acid-sulfate weathering of synthetic Martian basalt: The acid fog model revisited, *J. Geophys. Res. 109*(E5), doi:10.1029/2003JE002218.

Yen, A. S., Gellert, R., Schroder, C., et al. (2005), An integrated view of the chemistry and mineralogy of martian soils, *Nature, 436*, 49-54, doi:10.1038/nature03637.

Young G. M. and Nesbitt, H. W. (1998), Processes controlling the distribution of Ti and Al in weathering profiles, siliciclastic sediments and sedimentary rocks. *J. Sediment. Res., 68*, 448–455.

Chapter 2

Origin of Basaltic Soils at Gusev Crater, Mars, by Aeolian Modification of Impact-Generated Sediment

A version of this chapter was originally published Journal of Geophysical Research Planets, 116 (2011), E00F22, doi:10.1029/2010JE003712.

Abstract

Textural properties of soils including grain size, sorting, modality, skewness, shape (quantified as sphericity and qualified as form), roundness, and grain size distribution, have been measured and calculated from Microscopic Imager (MI) high-resolution images from the Mars Exploration Rover (MER) Spirit in Gusev crater. Soil targets were classified by grain size into five groups: fine to medium sand dark soil, medium sand to very fine pebble bed form armor, and very fine to medium pebble lithic fragments, a bimodal mixed soil, and an excavated soil trench. The abundance of submature, very poorly sorted, bimodal mixed soils indicates incomplete sorting by soil type. Probability distributions of excavated subsurface soil match crushed sediment analogs, indicating impact comminution, while all other soils show no direct evidence of an impact origin. If soils were produced primarily by impacts, then the evidence from probability distributions, angular shapes, and agglutinates have been reworked by postimpact surface activity. Soils in Gusev crater are continuously modified, reworked, and sandblasted. Textures of surface sediments are disconnected from subsurface textures and only reflect modern surficial aeolian processes. Models to reconstruct physical and chemical soil formation properties should not assume a static three-dimensional structure. A three-step model, initiated by the formation of basaltic crust and its alteration, followed by bolide impact, and finally modification by aeolian reworking is envisioned for the formation of soils. Such a scenario accounts for the potential that surface sediments may be compositionally and texturally distinct from the subsurface.

1. Introduction

Observations of soils [Yen et al., 2005; Cabrol et al., 2008; Sullivan et al., 2008; Yingst et al., 2008] and aeolian bed forms, including ripples and sand dunes, along the Spirit rover [Squyres et al., 2004] traverse in Gusev crater [Arvidson et al., 2006, 2008] have demonstrated the importance of wind as a dominant abrasion and transport mechanism on Mars [Greeley et al., 2003, 2004]. Further, the importance of aeolian processes are related to the development of individual soil types in Gusev crater, with each type attributed to differences in sediment entrainment and transport [Yen et al., 2005; Sullivan et al., 2008]. However, other potentially significant soil formation mechanisms, such as comminution by impacts, have not been explored. Chemical weathering in the form of in situ leaching of soluble elements has been hypothesized to result in regional variations in soils [Amundson et al., 2008], but models have not discussed the role of physical processes in soil genesis. A model for the origin of Martian soils, constrained against textural data, is needed to resolve the complex physical history of soils.

Soils, as the uppermost unconsolidated layer of material, define a critical zone at the interface between the lithosphere, atmosphere, and hydrosphere. In this paper, the term Martian soil refers to the upper unconsolidated layer of dust, sand, and lithic fragments and excludes any organic component [Gellert et al., 2004] found in terrestrial soils. Changes in soil-atmosphere-hydrosphere interactions over time can be recorded by the alteration of soil compositions and the modification of textures. Sedimentary textures preserve the history of formational processes and have been used extensively to interpret the characteristics of flow types in terrestrial aqueous environments [Mulder and Alexander, 2001; Kleinhans, 2005], the extent of transport and origin

of aeolian loess [Yang and Ding, 2004], and the impact origin of lunar soils [King, 1977; Liu et al., 2008].

The origin, timing, and balance of processes in soil formation and alteration on planetary surfaces are varied. Sediments on the surface of Mars likely have a complex history of formation and subsequent transport [McLennan et al., 2005]. Planetary bodies such as the Moon have recorded bolide impacts that pulverized the surface, forming soils [King, 1977; Lucey et al., 2006]. Similar conditions also affected the entire inner solar system [Chyba, 1993], including Mars [Knauth et al., 2005]. However, the importance of impact gardening in soil production is difficult to decipher, given evidence for sedimentary reworking of the Martian surface [McLennan et al., 2005].

The purpose of this paper is to place constraints on the formative mechanisms of Martian soils in the Gusev plains and Columbia Hills through textural characterization and interpretation. For seven years, the Spirit rover has surveyed soil targets over long traverses in Gusev crater (Figure 2.1), and its Microscopic Imager (MI) [Herkenhoff et al., 2004] has produced very detailed images of surface materials. Quantified textural properties of soils are used to ascertain the conditions of soil formation including physical degradation and transport. Properties of soil textures including grain size [Stevens et al., 1996; Batt and Peabody, 1999; Kok, 2010], sorting, modality, skewness, shape (quantified as sphericity and qualified as form [Bridges et al., 2010]), and rounding [Gillette and Chen, 1999] are inherited from the source material, but also may be strongly modified from the abrasion and impact of grains during aeolian transport [Knoll et al., 2008; Laity and Bridges, 2009; Zimbelman et al., 2009]. Grain size distributions are evaluated

to determine if the range of soil types have distinct formation processes or represent homogenous soils later reworked by more recent physical processes. Our preferred model for soil formation begins with a compositionally varied surface that is disrupted by a bolide impact, which generates an extensive ejecta blanket. This blanket is subsequently modified by aeolian processes that produce thin reworked sedimentary deposits.

2. Methodology

2.1. Sample Selection

Over 6000 MI images have been collected at 344 sites in Gusev crater, creating a large inventory from which to study soils. It is possible to identify grains with diameters of ~100 μm in the high spatial resolution (~31 μm/pixel) MI images [Herkenhoff et al., 2004]. Soil targets in Gusev crater were selected based upon the availability of well focused MI images for grain analyses and corresponding mineralogical and chemical data for evaluations of chemical weathering [McSween et al., 2010; chapter 3]. Of 59 soil targets during the first 1360 sols, 25 soil targets (Figure 2.1) were suitable for full textural analysis on the basis of MI lighting and image focus, although 6 targets were composed entirely of dust and lacked measureable grains. One subsurface soil (Paso Dark) excavated in a trench by the rover wheel and compressed by the Mössbauer contact plate, was also measured to evaluate variations in grain distributions with depth for comparison to the undisturbed, in place, surface soils. Typically a stack of five or six MI images was taken for each target with minor changes in focal length distances. The image in the stack with the best focus of the soil grains

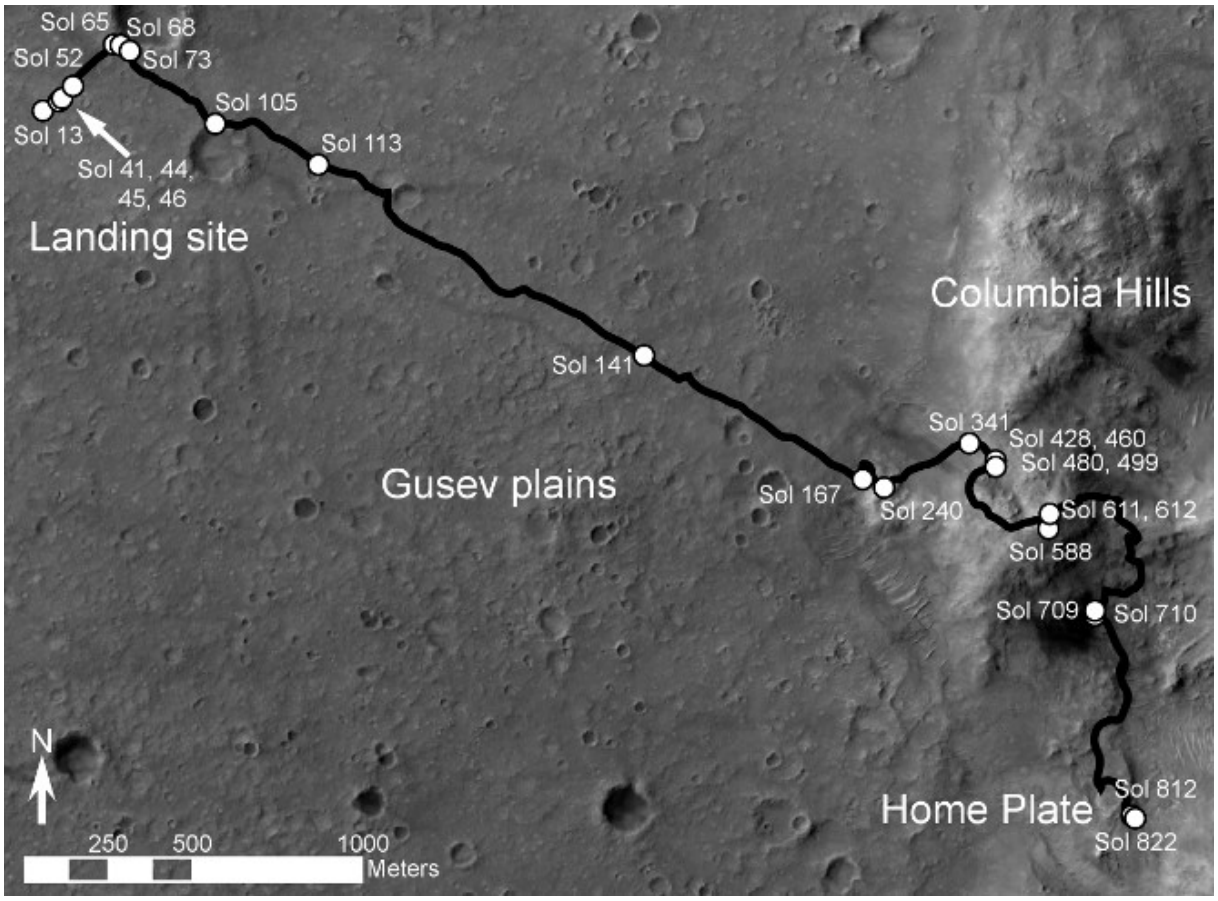

Figure 2.1. Location of measured soil targets along the Spirit rover traverse from the landing site in Gusev plains, Columbia Hills, from Columbia Memorial Station to Home Plate, HiRISE image PSP_001513_1655.

was then selected to represent each of the soil targets. In addition to the 26 quantifiably analyzed images, a survey of 45 additional soil targets along the Spirit rover transverse (Table 2.A in Appendix) was conducted to classify soil types and evaluate the distribution of soils observed in Gusev crater.

To ensure a random population of particles for analysis, a 20 × 20 grid was placed over each MI image to obtain a statistically significant sample of at least 400 point counts [e.g., van der Plas and Tobi, 1965; Ingersoll et al., 1984]. This approach represents a nearly 100% improvement in probable error at 95% confidence relative to using 100 counts per analysis as done in previous studies [e.g., Cabrol et al., 2008; Yingst et al., 2008]. Textural parameters for a total of 8200 points were measured (Table 2.1). Grid spacing was adjusted to be appropriate for the grain sizes in each image.

Due to the inability to measure the short, intermediate, and long axes on two-dimensional MI images, the apparent grain sizes must be estimated from two-dimensional data. Current semiautomated methods of digital size measurements [e.g., McGlynn and Okin, 2006] are unsuitable to accurately measure the size of sediment grains when applied to all MI images along the Spirit rover traverse. To characterize grain sizes in soil images, we employed a manual measuring method similar to petrographic digital image analysis [Saltikov, 1967; Buscombe et al., 2010; Strom et al., 2010], where the major axis is the longest measurable length between two points. Major axes were then converted to the standard logarithmic unit

phi (ϕ) where S is the major axis length and sedimentary grains are classified, using the

$$\phi = -\log_2 S\,(\text{mm}) \tag{1}$$

Wentworth scale [Folk, 1981], into major grain size groups such as silt (4 to 9 ϕ, 1/16 to 1/512 mm), sand (−1 to 4 ϕ, 2 to 1/16 mm), and gravel (<−1 ϕ, >2 mm). Individual grains smaller than very coarse silt (ϕ > 4) cannot be resolved in ~32 μm/pixel resolution MI images. The range, or difference between the largest and smallest grains (Δ ϕ), is used to qualify sorting of grains as <0.35 ϕ very well sorted, 0.35 ϕ − 0.5 ϕ well sorted, 0.5 ϕ − 0.7 ϕ moderately sorted, 0.5 ϕ − 0.7 ϕ poorly sorted, >2.0 ϕ very poorly sorted [Folk, 1981]. Empirical-based conversions of measured dimensions to sieve size distributions can also be applied [Harrell and Eriksson, 1979].

2.2. Textural Parameters

Particle morphology is described by shape and roundness [Blott and Pye, 2008]. Particle shape has 2 components, namely sphericity (a quantitative calculation) and form (a qualitative classification). Sphericity is a measure of how equal the three axis (long, intermediate, short) are in relation to a perfect sphere. Riley Sphericity (S_R), a two- dimensional representation, is

$$S_R = \sqrt[2]{\frac{D_i}{D_c}} \tag{2}$$

defined where D_i is the diameter in mm of the largest inscribed circle within a grain boundary and D_c is the diameter in mm of the smallest circumscribed circle outside a grain boundary (Figure 2.2). The shape of a grain is qualified as the form, and classified using sphericity as: <0.60 = very elongate, 0.60–0.63 = elongate, 0.63–0.66 = subelongate, 0.66–0.69 =

Table 2.1. Textural Summary of Soils with MI Images for Targets in the Gusev Plains and Columbia Hills

	Point Counts			Size					Shape		Roundness	
	Points	Size Counts	Roundness Counts	Mean (ϕ)	Median (ϕ)	Range	Sorting	Modality	Form	Reiley Sphericity S_R	Wentworth ρ	Powers
167	400	303	262	0.99	0.97	3.04	very poorly sorted	unimodal	equant	0.73	4.5	subrounded
341	400	322	217	1.23	1.16	3.66	very poorly sorted	unimodal	very equant	0.75	4.5	subrounded
709	400	348	337	1.54	1.51	2.70	very poorly sorted	unimodal	very equant	0.75	5.0	rounded
710	400	337	261	2.03	1.97	3.25	very poorly sorted	unimodal	equant	0.72	4.8	subrounded
mean				1.45	1.40	3.16				0.74	4.7	
bedform armor soils												
41	400	220	213	-0.38	-0.43	2.83	very poorly sorted	unimodal	very equant	0.80	5.2	rounded
45	400	143	143	-1.02	-1.01	2.20	very poorly sorted	unimodal	very equant	0.76	5.0	rounded
52	400	165	147	-0.47	-0.59	2.13	very poorly sorted	unimodal	very equant	0.79	4.4	subrounded
611	400	84	80	-0.66	-0.90	4.39	very poorly sorted	unimodal	very equant	0.80	4.0	subrounded
612	400	256	254	-0.84	-0.94	2.43	very poorly sorted	unimodal	very equant	0.80	4.2	subrounded
mean				-0.68	-0.77	3.26				0.79	4.6	
lithic fragments soils												
44	400	100	93	-2.37	-2.31	3.00	very poorly sorted	polymodal	subequant	0.72	4.9	subrounded
46	400	50	48	-2.16	-2.60	3.40	very poorly sorted	polymodal	subequant	0.71	5.0	rounded
105	400	66	66	-2.52	-2.53	1.84	poorly sorted	polymodal	intermediate shape	0.67	4.8	subrounded
113	400	39	37	-2.83	-3.26	4.45	very poorly sorted	polymodal	very equant	0.79	4.9	subrounded
mean				-2.45	-2.68	3.15				0.72	4.9	
bimodal mixed soils												
73	400	193	193	0.12	-0.16	3.87	very poorly sorted	unimodal	very equant	0.78	4.9	subrounded
460	400	339	202	-0.02	1.16	7.65	very poorly sorted	polymodal	subequant	0.72	4.1	subrounded
480	400	206	109	1.62	1.51	4.29	very poorly sorted	unimodal	equant	0.74	4.4	subrounded
499	400	365	265	0.26	-0.36	5.39	very poorly sorted	bimodal	very equant	0.77	4.2	subrounded
812	400	378	162	1.28	1.80	5.92	very poorly sorted	bimodal	subequant	0.71	4.8	subrounded
822	400	339	95	2.11	2.16	5.11	very poorly sorted	bimodal	subequant	0.69	4.7	subrounded
mean				0.90	1.02	5.37				0.73	4.5	

Table 2.1. (continued)

	Point Counts			Size					Shape		Roundness	
	Points	Size Counts	Roundness Counts	Mean (ϕ)	Median (ϕ)	Range	Sorting	Modality	Form	Reiley Sphericity S_R	Wentworth ρ	Powers
excavated subsurface soil												
428#1	200	178	106	1.87	1.97	4.36	very poorly sorted	unimodal	equant	0.72	4.0	subrounded
428#2	200	181	106	1.31	1.51	4.91	very poorly sorted	bimodal	equant	0.74	3.3	subangular
428#3	200	179	155	-0.47	-0.56	4.32	very poorly sorted	unimodal	equant	0.74	3.3	subangular
mean				0.90	0.97	4.53				0.73	3.6	

intermediate shape, 0.69–0.72 = subequant, 0.72–0.75 = equant, >0.75 = very equant [Folk, 1981].

Rounding (ρ), which is independent of sphericity, represents a visual estimation of the roughness of a grain surface and classified using the Power's roundness scale. Grains are visually classified from 1 to 6, with 1 being very angular and 6 being well rounded [Powers, 1953; Blott and Pye, 2008]. The results of textural analysis provide a comprehensive data set of parameters that includes grain size, grain size range, population modality, roundness, sphericity, and sorting, and the resultant statistical characterizations useful in interpretation of processes, which are essential in determining the extent of the physical weathering and transport processes that have affected the soils.

2.3. Grain Size Distribution

The distribution of grains in a soil sample can be described in terms of mean, median, range, sorting, modality, skewness, and kurtosis [e.g., Ibbeken, 1983; Cheetham et al., 2008]. Distributions can be further described by fitting a variety of mathematical functions such as lognormal, log-hyperbolic, and log-Laplace [McEwen et al., 1959; Purkait, 2006]. The method of distribution projection is not important to identify specific processes, but it must be consistent to enable comparisons between soils [Zobeck et al., 2003]. In this paper, we evaluate soils using standard cumulative percent distribution curves to facilitate comparisons of Gusev soils with other unconsolidated sediments on the Earth and Moon.

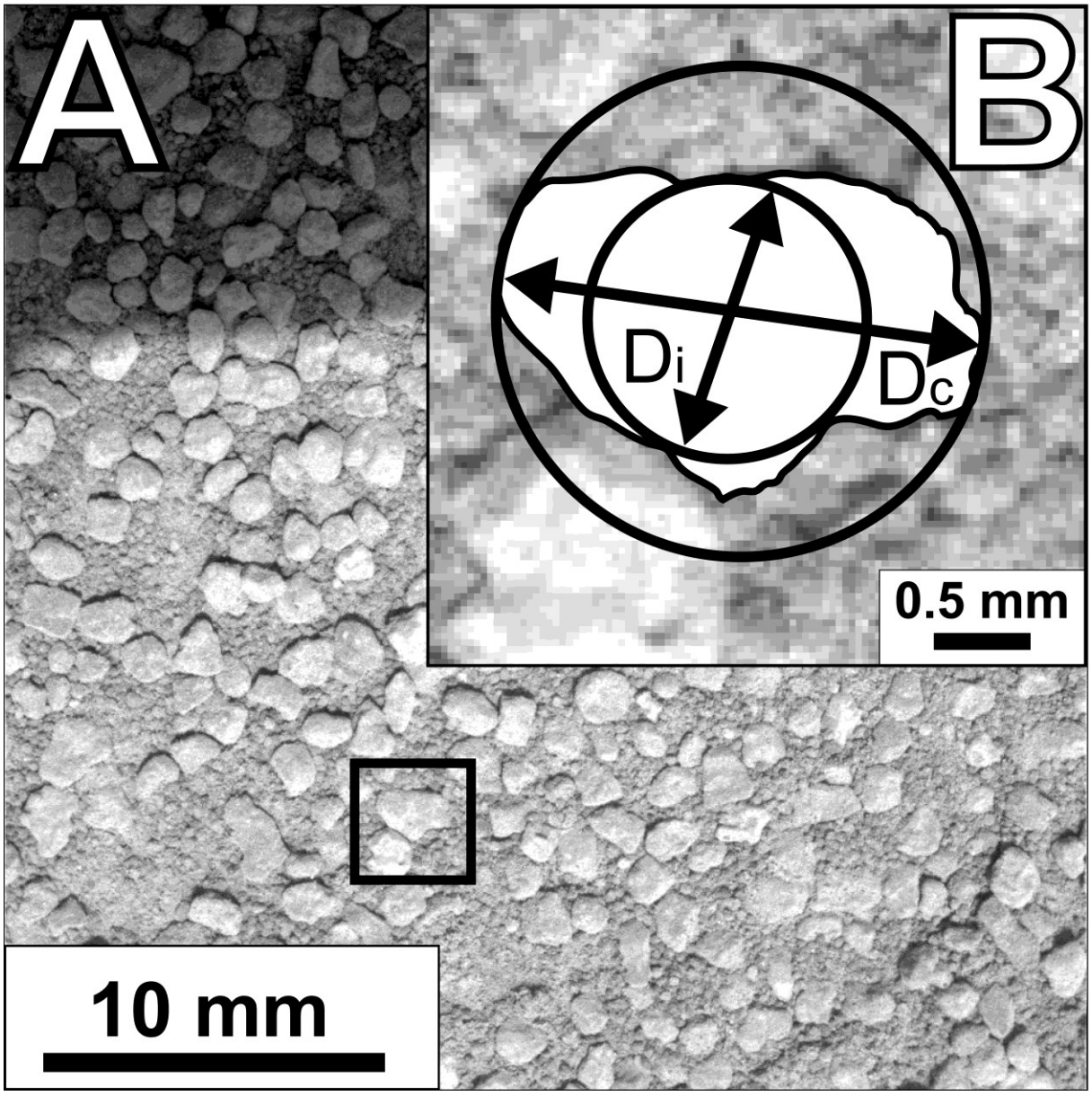

Figure 2.2. Demonstration of the measurements of Riley Sphericity applied to (a) Pequod Doubloon (sol 499). (b) Magnified grain to show measurements of D_c = 1.9 mm, D_i = 1.6 mm, and S_R = 0.9.

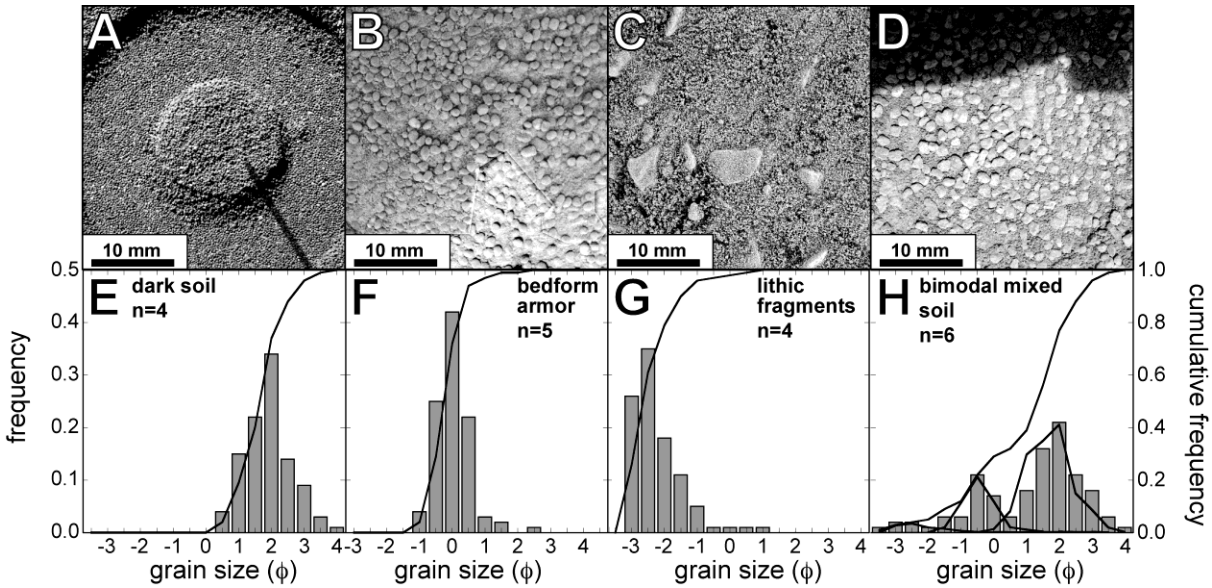

Figure 2.3. Major soil classes grouped by grain sizes and representative soil targets viewed by the microscopic imager (MI). Dust (< 100 μm) is present in most soils. (a) Dark soil (El Dorado shadow sol 709); (b) bed form armor (Arena Crest sol 41); the upper part of image has been adjusted to remove a shadow for clarity; (c) lithic fragments (Grande Flats Trout 1 sol 46); (d) bimodal mixed soil (Pequod Doubloon sol 499); (e) mean grain size histogram for dark soil; (f) mean grain size histogram for bed form armor soil; (g) mean grain size histogram for lithic fragment soil; (h) mean grain size distribution of bimodal mixed soil.

The asymmetry of non-Gaussian grain size frequency curves can be quantified as skewness, where an abundance of coarse grains in a grain size population is negatively skewed toward lower (or negative) ϕ sizes, or coarse skewed. Populations with an abundance of fine grains, skewed toward higher ϕ sizes, are positively, or fine skewed. Skewness is calculated as inclusive graphical skewness (SKt) from the 5, 16, 50, 84, and 95 percentile values from a cumulative distribution curve [Pettijohn et al., 1987], and then classified as: >0.30 = strongly fine skewed, 0.30 to 0.10 = fine skewed, +0.10 to −0.10 = near symmetrical, −0.10 to −0.30 = coarse skewed, <−0.30 = strongly coarse skewed.

3. Textural Characteristics of Gusev Soils

An initial survey of surface material in Gusev crater [Yen et al., 2005] classified soils into four major groups (Figures 2.3A–2.3D): (1) bright dust, (2) dark soil, (3) bed form armor, and (4) lithic fragments. Among the soil types, "bright dust" (sols 13, 65, 68, 141, 240, 588) is the uppermost surface layer. It is composed of grains with sizes below the MI detection limit (~100 μm) and thus we cannot study it as a textural class. Of the remaining classes, "dark soil" grains were identified as surface grains beneath the bright dust layer, with ~100 μm grains visible at the MI detection limit. Soils of 'bed form armor' were described as millimeter-sized, wind-deposited grains, and "lithic fragments" as coarse grains embedded into the surface. However, the presence of bimodal soils, having a variety of grain sizes, and discrete subsurface soil layers, indicates more complex transport histories and formations than previously considered. The characterization of two-dimensional imagery reveals no data in the vertical dimension, and thus, limits the understanding of soil formation to only the latest phase of surface activity and not the total picture, including the potential importance of impact gardening. Two new soil classes,

"bimodal mixed soil" and excavated "subsurface soil" in a trench, are included with the original four and are used to group soil samples and summarize broad trends in soil textural characteristics.

3.1. Dark Soil

3.1.1. Description

Four samples of dark soil (sols 167, 341, 709, 710) that were used in this analysis (Figure 2.3A) have measured grain sizes ranging from very fine to coarse sand. Fine silt size grains (≤100 μm) are also visible, but are too small to measure directly. Measured mean grain sizes vary from 0.98 ϕ (very coarse sand) to 2.01 ϕ (fine sand; Figures 2.3E, 2.4A, and Table 2.1), coarser than the 3 to 4 ϕ (very fine sand) originally identified [Yen et al., 2005]. Histograms of grain sizes reveal three individual soil samples with the same peak of medium sand (1.5 ϕ to 2.0 ϕ), and one sample (167) with a peak of coarse sand (0.5 ϕ to 1.0 ϕ). All dark soil samples are very poorly sorted with the greatest difference in grain sizes of 3.75 ϕ and the smallest difference of 2.70 ϕ. All dark soils have a unimodal distribution and all are fine or strongly fine skewed (Table 2.2). Cumulative percentage of sediments plotted exhibit a near-Gaussian distribution S-shaped curve (Figure 2.3E). Of the four samples, two are equant and two are very equant with mean sphericity ranging from S_R = 0.72 to 0.75. Grains range from angular to well rounded (mean ρ = 4.7; Figure 2.4C). The concentration of fine grains (> 0 ϕ) in dark soil (Figure 2.5A) is represented by steep slopes from 0 to 1 ϕ. Dark soils are primarily associated with ripples such as the large El Dorado ripple field [Sullivan et al.,

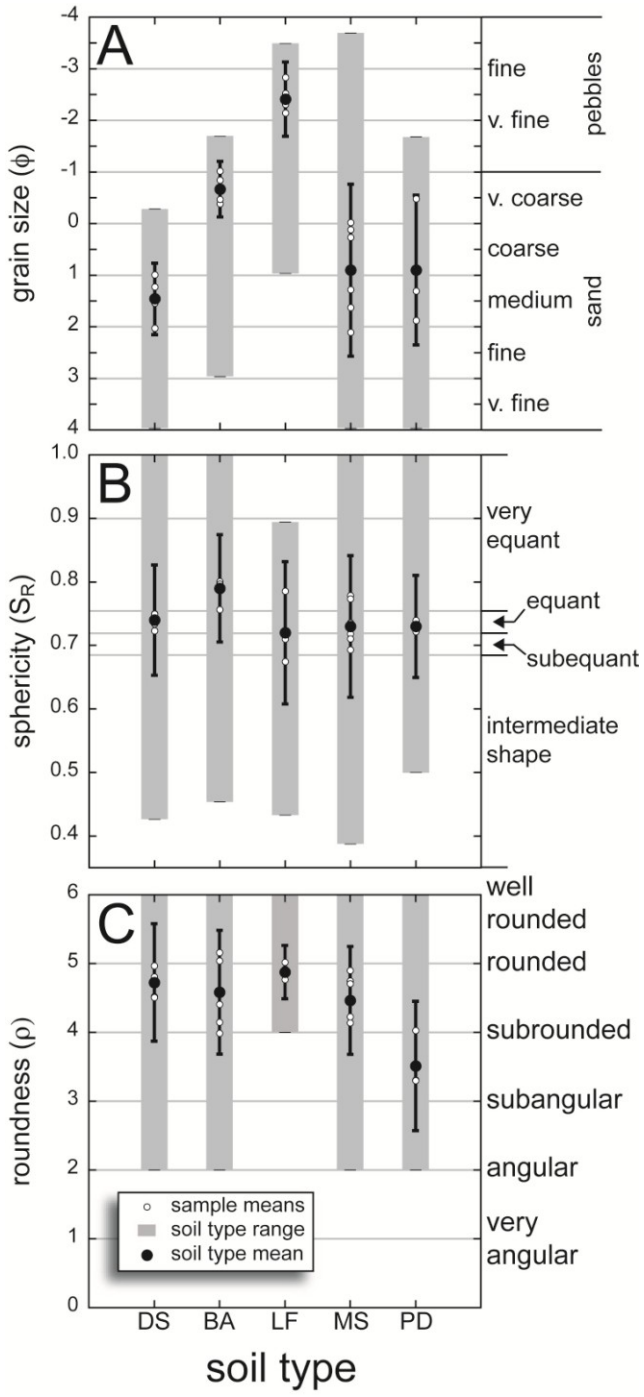

Figure 2.4. Mean (black dot), standard deviation (black bar), range (gray bar), and individual sample means (white dot) for (A) grain size (ϕ), (B) sphericity (S_R), and (C) roundness (ρ) grouped by soil type, where DS is dark soil, BA is bed form armor, LF is lithic fragments, MS is bimodal mixed soil, and PD is Paso Dark excavated soil. Soils are typically very poorly sorted and have similar sphericity and roundness.

Table 2.2. Gain-size Statistical Summary by Graphical Methods

	Graphical Mean, M_z	Inclusive Graphic S.D., σ_i	Inclusive Graphic Skewness, SK_i	Skewness
dark soils				
167	0.98	0.48	0.52	strongly fine skewed
341	1.57	0.80	1.84	strongly fine skewed
709	1.56	0.42	0.10	fine skewed
710	2.01	0.56	0.41	strongly fine skewed
bedform armor soils				
41	-0.40	0.34	0.16	fine skewed
45	-1.02	0.45	0.02	near symmetrical
52	-0.68	0.40	-0.07	near symmetrical
611	-0.61	0.84	2.78	strongly fine skewed
612	-0.85	0.33	0.05	near symmetrical
lithic fragment soils				
44	-2.31	0.49	-0.30	coarse skewed
46	-2.26	0.65	1.58	strongly fine skewed
105	-2.58	0.42	0.02	near symmetrical
113	-3.09	0.72	4.90	strongly fine skewed
bimodal mixed soils				
73	0.10	0.82	2.12	strongly fine skewed
460	0.03	2.15	-19.01	strongly coarse skewed
480	1.65	0.62	0.25	fine skewed
499	0.06	1.23	7.65	strongly fine skewed
812	0.98	1.85	-10.67	strongly coarse skewed
822	2.09	0.73	0.52	strongly fine skewed
excavated subsurface soil				
428#1	1.88	0.83	-0.18	coarse skewed
428#2	1.28	1.30	-1.84	strongly coarse skewed
428#3	-0.47	1.01	2.18	strongly fine skewed

2008], and are observed at middle elevations between ~20 to 70 m on the slopes of Columbia Hills and at Home Plate (Figure 2.6). Dark soils are also found extensively as deposits on exposed rocks at the base of Home Plate.

3.1.2. Interpretation

Dark soil samples (Figure 2.3A and Table 2.1) represent sand within ripple marks, and therefore are interpreted to be formed by saltation (Figure 2.7A). Grain sizes are fairly consistent within the dark soil class, with the lowest maximum range ($\Delta \phi = 3.75$) of soil classes. The grain size for saltation on Mars is theorized to be as small as 100 μm [Greeley et al., 1980], capable of moving very fine sand. Saltating grains move by long jumps, transferring momentum upon impact with the surface, and ejecting gains downwind. The saltation of grains has been implied for dune activity in Meridiani Planum [Chojnacki et al., 2011], for ≤ 300 mm sand in Gusev crater [Sullivan et al., 2008], and may be associated with dust devils [Greeley et al., 2006a], but are uncommon [Greeley et al., 2006b]. Wind velocities may rarely reach the saltation threshold [Parteli et al., 2009], although recent models indicate saltation can be sustained at low wind speeds [Kok, 2010].

Saltation can be an ideal transport process to remove very fine and fine sand (>2.0 ϕ) present in dark soils, but it would be insufficient to transport the small amounts of coarse sand that is also present. Modeling of saltation behavior under Martian conditions suggests that once saltation is initiated, large-scale impact velocities can propagate saltation and result in high erosion of Martian soils [Almeida et al., 2008]. Dark soils contain a distinct unimodal, fine

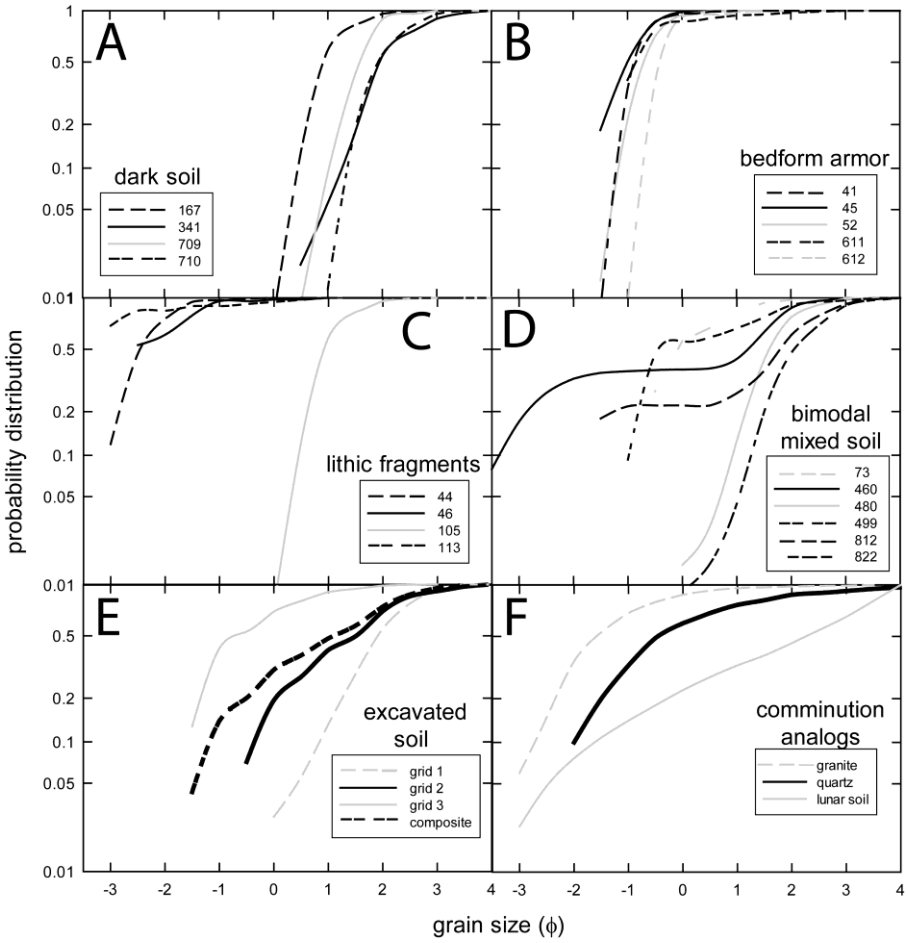

Figure 2.5. Grain size distributions presented as probability distribution curves. (A) Dark soil; (B) bed form armor soil; (C) lithic fragment soil, except for high dust cover in Bitterroot Flats (sol 105); (D) bimodal mixed soils that transition between dark soil (sols 480, 812), bed form armor (sols 73, 499), and lithic fragment (sols 460, 499) components; (E) multiple curves showing distribution of composite excavated Paso Dark soil. Light gray dashed line for grid 1 (n = 200) showing similarity with dark soil. Solid black line for grid 2 least resembles any common soil type but is similar to the composite curve (n = 600). Solid light gray line for grid 3 showing similarity with lithic fragment soil, particularly sol 44 (n = 400). Dashed black line showing composite of all three grids highlighting differences between individual components and the total population. Compare with comminuted material curves. (F) Crushed quartz (bold) and crushed granite sediments from Kittleman [1964], suggesting comminution by impacts. Apollo 11 soils formed from impacts renormalized from Mason [1971] are dissimilar to Gusev soils because of the biomal distribution from agglutinates which are not found on Mars. Soil types in Gusev crater are reworked and controlled by aeolian activity to sort and concentrate sediment and deviate from a comminution distribution. Numbers refer to the sol in which the soils were imaged by the MI.

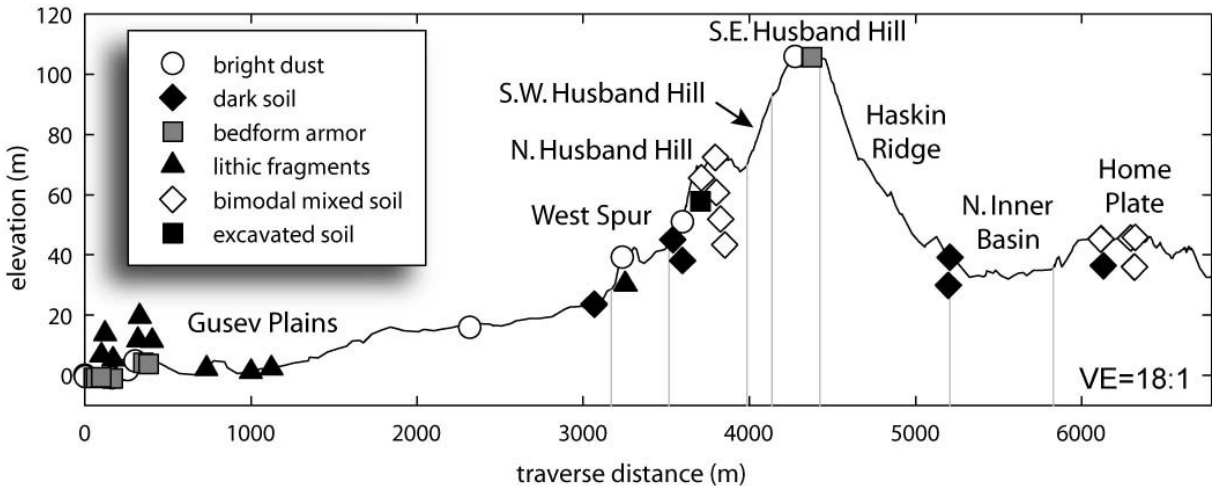

Figure 2.6. Survey of soil types classified along the Spirit rover traverse. Bright dust is present throughout the traverse and evidence of limited saltation; dark soils are concentrated in ripples between 20 to 70 m in elevation along the slopes of Columbia Hills and Home Plate. No clear spatial trend is observed for bed form armored soils, which are present near the landing site and at the top of Haskin Ridge but absent throughout most of Gusev plains. Lithic fragments and bimodal mixed soils are positioned throughout the traverse. Soil positions have stacked vertically in areas of high density. MI images are listed in Appendix Table 2.A.

skewed, grain size population that is clearly separate from bed form armor soils. With fine and finely skewed distributions (Table 2.2), the fine grains are suitable for saltation and partial removal from coarse components [Pye and Tsoar, 1990]. This indicates that saltation is sufficient to transport dark soil grains, with the exception of coarse grains observed in bed form armor, and provides an upper particle size limit for saltation conditions on Mars [e.g., Batt and Peabody, 1999]. In addition to saltation, armoring of dark soil grains is visible at Larry's Lookout (sol 494). All measured soils in Gusev crater are poorly and very poorly sorted (Table 2.1), which suggests aeolian transport is incomplete in separating grains by mechanical forces at present, as interpreted by the presence of dust on rock surfaces that would otherwise be removed in an active saltating environment [Greeley et al., 2004].

Similarities of equant and very equant forms in dark soil samples (Figure 2.4B) are likely to result from common composition in the source materials. Particles break along imperfections in bonding between constituent minerals and along cleavage planes and fractures within minerals, and fracture of glass between minerals, resulting in fragments of similar mineral proportions as the parent material. Sediments with similar compositions can retain similar shape from failures along cleavages or fracture [Benn and Ballantyne, 1993; Cho et al., 2006].

The high degree of rounding (mean $\rho = 4.7$; Figure 2.4C) of dark soils is a direct indication of abrasion from transport. Sediment rounding by the collision of particles during aeolian transport is 100 to 1000 times more effective than during movement by fluvial processes [Pettijohn et al., 1987]. In addition to the type of transport, greater distance of transport increases the duration of abrasion and increased transport increases roundness in all

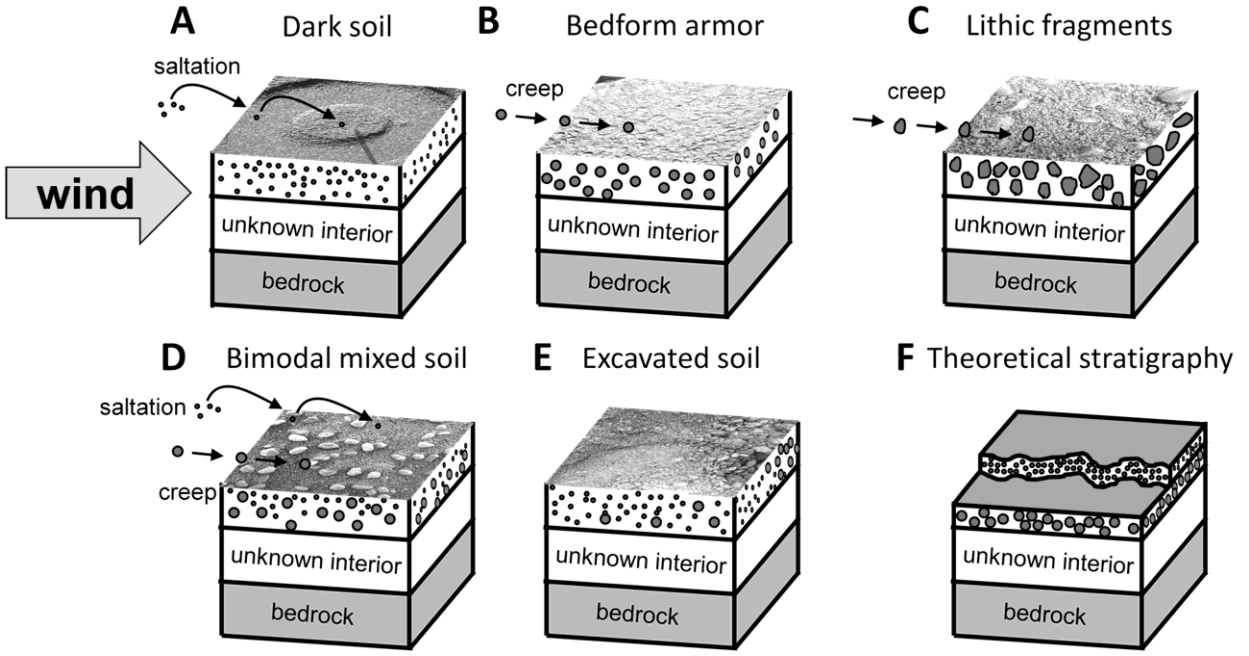

Figure 2.7. Imaged grains represent the uppermost layer of material without regard to variations in grain size distributions that may not be apparent from the surface. Soil classes in Gusev crater have surface textures modified and mixed by aeolian activity. In Figures 2.7A–2.7D, wind is from left to right. (A) Formation of dark soil by saltation; (B) formation of bed form armor soil by removal of fine sand by saltation and concentration of coarse sand by creep; (C) formation of lithic fragment soil by sandblasting and creep; (D) formation of bimodal mixed soils by saltation to remove fine sand and incomplete concentration of coarse sand; (E) coarse sand in Paso Dark subsurface soil is overlain by finer sand and not visible from the surface; (F) surfaces textures in all soils may not resemble subsurface sediment that can be compositionally or texturally distinct, such as in this theoretical stratigraphy where subsurface stratigraphy may be obscured by surface processes such as dust deposition or armoring.

environments. Collisions of grains during transport are also affected by the size and density of the grains and the velocity of the transporting medium. Small grains with low mass and momentum are less susceptible to collision-caused abrasion, and grains smaller than 50 μm are generally not further rounded [Cho et al., 2006]. A relationship between particle size and roundness, where roundness increases with increased particle size [Khalaf and Gharib, 1985; Bullard et al., 2007], is not observed. If dark soils were formed entirely by bolide impacts, grains would be angular, as observed in lunar soils [King and Butler, 1977]. The combined textural evidence of grain sizes and rounding suggests that dark soil samples have been strongly modified by saltation (Figure 2.7A). The observed position of dark soil sand may be an indication of sampling bias of the MI instrument. Dark soil sand may be more extensive throughout Gusev crater; however observations are limited by the availability of MI images.

3.2. Bed Form Armor

3.2.1. Description

Bed form armor soils (Figure 2.3B), measured in five samples (sols 41, 45, 52, 611, 612), contain larger grains (Figure 2.3F) than dark soils, with mean grain sizes (Table 2.1) of very fine pebbles (−1.02 ϕ) to very coarse sand (−0.38 ϕ). Bed form armor samples have a distinctly coarser grain size compared to dark soils. Most grains fall between −1.5 ϕ to 1.5 ϕ (medium sand to very fine pebbles; Figure 2.3F). Dust, which is not visibly present in dark soils, appears to be present in all bed form armor soils and forms noticeable clumps in Sugar T1 (sol 52). All bed form armor soils are very poorly sorted (Table 2.1), with the largest range between grain sizes of 4.39 ϕ (sol 611) and smallest range of 2.13 ϕ (sol 52). All five samples possess unimodal grain size distributions, but with different histogram peaks. Three of the soils (sols 45, 52, 612) have a

near symmetrical skewness (Table 2.2) and histogram peaks at −1.0 ϕ to −0.5 ϕ. The remaining soils are fine skewed (sol 41) and strongly fine skewed (sol 611), reflecting the presence of medium and fine sand. The presence of finer grains (>0 ϕ) is visible in the shallow-sloped cumulative distribution curve (Figure 2.3F). All bed form armor soils are very equant with mean sphericity from 0.75 to 0.80 (Figure 2.4B). Roundness varies (Figure 2.4C) from subangular (sols 611, 612), to rounded (sol 45), and to well rounded (sols 41, 52). Probability distributions of bed form armor soil samples (Figure 2.5B) are concentrated with curves between −2 to −1 ϕ, for the presence of coarse sand. Overall, soils with bed form armor are observed in 5 targets within 400 m of the landing site, but are not found elsewhere in the plains or on the slopes of Columbia Hills (Figure 2.6). Bed form armor is also observed in 2 images located at the top of Haskin Ridge.

3.2.2. Interpretation

Bed form armor soils are interpreted to be the concentration of creep-driven small-scale bedding structures such as inversely graded coarse sand (Figure 2.7B) into coarse ripples [Sullivan et al., 2008]. Very coarse sand and very fine pebbles in bed form soils are too coarse to be transported by saltation that formed dark soils [Greeley et al., 1980]. Momentum transfer from impacts of saltating particles also induces creep of larger very coarse sand grains [Zimbelman et al., 2009]. The transition between saltation and creep is gradual [Bagnold, 1941; Shao, 2000].

Uniformity in grain shape of very equant bed form armor samples (Figure 2.4B) is consistent with compositional similarity and common transport pathways [Pye and Tsoar, 1990].

Preferential development and survival of equant and very equant forms by fracture are common during transport and deposition [Benn and Ballantyne, 1993]. Changes in the maximum projection area of a particle (sphericity) with grain size do not appear to have resulted in sorting by settling separation. Generally, sphericity decreases with an overall increase in grain size, due to a higher probability of imperfections in the crystal structure of larger grains which increases the likelihood of fracturing [Cho et al., 2006]. In bed form armor samples, the change in sphericity is not statistically significant, and a narrow range of sphericities between 0.8 and 1.0 suggests similar original compositions or abrasion histories. The high sphericity would also be consistent with a lapilli source.

Bed form soils exhibit a range in roundness (Figure 2.4C) from well rounded (Figure 2.8A) to subangular (Figure 2.8B). Such differences likely reflect variations in transport distance of bed form grains. Two samples at the edge of the Lands End ripple (Lands End sol 611, Hang Two sol 612) in adjacent sites were more angular than the average (ρ = 4.0, 4.2; Figure 2.4C), which may point to different formation processes, or reduced transport. The distribution of grain sizes in Lands End and Hang Two are not distinct from other bed form soils, indicating that they have not fractured from extensive aeolian transport. Larger grains should exhibit greater rounding than smaller grains for the same amount of transport [Pettijohn et al., 1987]. Therefore, the two subangular bed form soils must have different transport histories with less attrition and abrasion than other bed form armor and dark soil samples. A profile of an armored surface overlaying finer sediment exposed by the rover wheel, demonstrates the concentration of coarse sand and very fine pebbles (Figure 2.8C). The source of armored sediment may be fallout from lapilli, and grains are similar in size and sphericity to rounded cemented grains observed in the layered

King George Island outcrop [Arvidson et al., 2008] and to the Superpesis target (sol 1209) at the base of Home Plate (Figure 2.8D). In addition, sandblasted rocks such as the exposed Pace target (sol 373) exhibit significant abrasion and is a likely source of coarse sand. We interpret that bed form armor soils are formed (Figure 2.7B) as creep transported and abraded grains that contain very coarse sand and very fine pebbles that are too coarse for saltation. The concentration of coarse sand from wind-related transport is observed in coarse sand ripples formed from creep-driven lateral transport throughout Gusev crater [Sullivan et al., 2008] with similar observations in Meridinai Planum [Jerolmack et al., 2006], deflation or aggradation, similar to terrestrial aeolian deflation lags [cf. Clemmensen and Abrahamsen, 1983, Figure 10B] may also serve as a minor mechanism to concentrate coarse sand.

3.3. Lithic Fragments

3.3.1. Description

The mean grain size of all four lithic fragment (Figure 2.3C) soils (sols 44, 46, 105, 113) exceeds other soil types, and ranges from −2.16 ϕ to −2.83 ϕ (Figure 2.4A). Most pebble clasts varied in size from −1 ϕ to −3 ϕ (very fine to fine pebbles). The largest grains measured in lithic fragment soils are medium pebbles. Minimum grain sized ranges from coarse (sols 46, 113) to very coarse sand (sol 44). Pebbles are exposed at the surface and partly buried into an upper layer of dust in all four samples. Grain shapes vary from

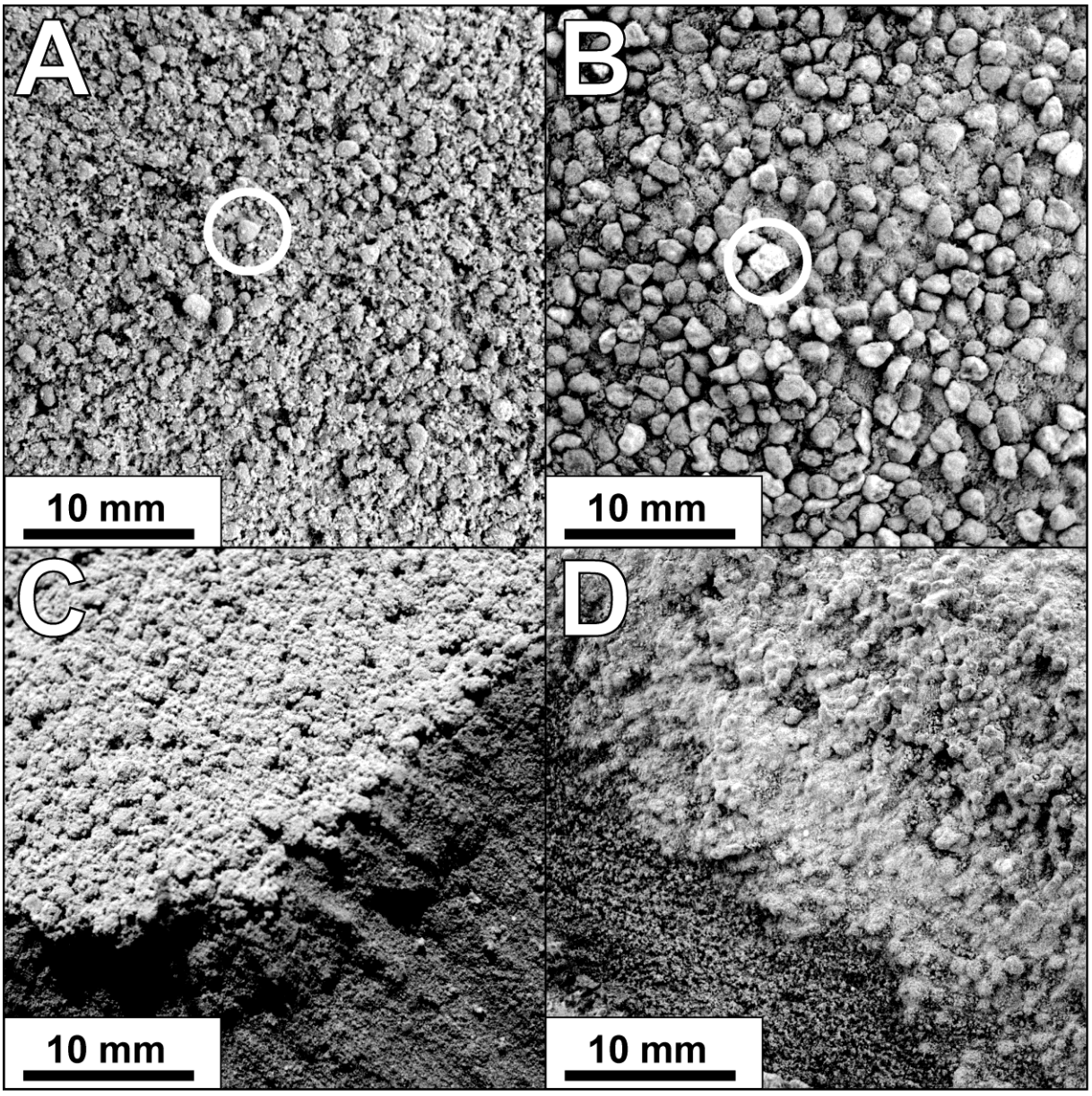

Figure 2.8. MI images showing differences in particle roundness in bed form armor soils. (A) Well-rounded grains in Sugar T1 (sol 52); (B) subangular grains in Hang Two (sol 612); (C) bed form armored surface at Bear Paw (sol 73) with finer grains below exposed by the rover wheels; (D) exposed outcrop of lapilli at the edge of Home Plate in the Superpesis target (sol 1209) are similar in size and may be a source of coarse sand found on armored surfaces. The lapilli image has been rotated 180° to facilitate viewing. Dust is present in all images.

intermediate shape to very equant (Figure 2.4B). Three of the soils (sols 44, 105, 113) are subrounded and one (sol 46) is rounded (Figure 2.4C). Lithic fragment soils range from poorly sorted to very poorly sorted (Table 2.1). Concentration of pebbles and a large range of grain sizes ($\Delta \phi > 4$) is observed in the probability distribution of lithic fragment soil (Figure 2.5C). Bitterroot Flats (sol 105) is distinct from other lithic fragment soil targets, as it is poorly sorted (Table 2.1), and it lacks medium pebbles. Lithic fragments are located throughout the traverse with no apparent spatial relationship, with nine observed in Gusev plains, three on the slope of West Spur and North Husband Hill, and one image in Home Plate (Figure 2.6).

3.3.2. Interpretation

Lithic fragment soils are interpreted to have a surface composed of creep-driven pebbles (Figure 2.7C) that have been abraded by sandblasting from exposure to saltating grains, consistent with observations of sandblasted rocks [Knoll et al., 2008] and soils [Greeley et al., 2004]. However, the abundance of dust indicates present aeolian activity was limited or intermittent. Pebble sizes in lithic fragment soils exceed the expected threshold for aeolian entrainment or saltation [Greeley et al., 2006b; Sullivan et al., 2008]. The transport of similarly sized grains by creep has been demonstrated in wind tunnel [Batt and Peabody, 1999] and field experiments [e.g., Davidson-Arnott et al., 1997; Nickling and McKenna Neuman, 2009] under terrestrial conditions at high threshold friction velocities, and creep may also be applicable to Mars conditions [e.g., Zimbelman et al., 2009].

3.4. Bimodal Mixed Soil

3.4.1. Description

Six samples (sols 73, 460, 480, 499, 812, 822), do not classify into the original established soil types of bright dust, dark soil, bed form armor, and lithic fragments of Yen et al. [2005], solely based on grain size. Bimodal mixed soils (Figure 2.3D) are grouped solely to facilitate interpretation and should not be interpreted as a single homogeneous group or process. Bimodal mixed soils are mostly located on flat ridges with 5 in North Husband Hill, 1 in Haskin Ridge, and 4 in adjacent targets in Home Plate (Figure 2.6), and are also present in a depression near the landing site.

3.4.2. Interpretation

Bimodal mixed soils have the greatest heterogeneity in grain shape among the major soil classes with subequant to very equant shape (Figure 2.4B), and are subangular to subrounded (Figure 2.4C). Mean grain sizes of bimodal mixed soils range from fine sand to very coarse sand (Figure 2.4A). A wide range of grain sizes is present from very fine sand to medium pebbles displaying a distinct bimodal distribution (Figure 2.3H). The near-horizontal slope between −1 ϕ to 1 ϕ in the mean cumulative distribution demonstrates the mixed population (Figure 2.5D). Two major groups of grains in bimodal mixed soils are identified: very fine to coarse sand (Figure 2.9A) and very coarse sand to medium pebbles (Figure 2.9B). Two bimodal mixed soils (sols 480, 822) are composed mostly of very fine to coarse sand, with histogram peak centers at 2.0 ϕ matching dark soils. Both soils also contain a small abundance of very coarse sand (sol 480) and very fine pebbles (sol 822) from bed form armor soils. Mawson (sol 812) also contains very fine to coarse

sand dark soil, but with a higher abundance of very coarse sand-sized bed form armor grains. Coarse sand from bed form armor grains is in higher abundance than fine to medium sand from dark soils in two samples (sols 73, 499), with histogram peaks of very coarse sand, and secondary peaks of coarse (sol 73) and medium sand (sol 499).

Unlike the rest of the bimodal mixed soils, the Almond Crumble sample (sol 460) does not contain very coarse sand that is common in bed form armor soils. Instead, the sample contains a mixture of grains matching the sizes of dark soil and lithic fragment soil. A maximum histogram peak at 1.5 to 2.0 ϕ matches the medium sand of dark soil and a secondary peak at -2.5 ϕ matches fine pebbles found in lithic fragment soil.

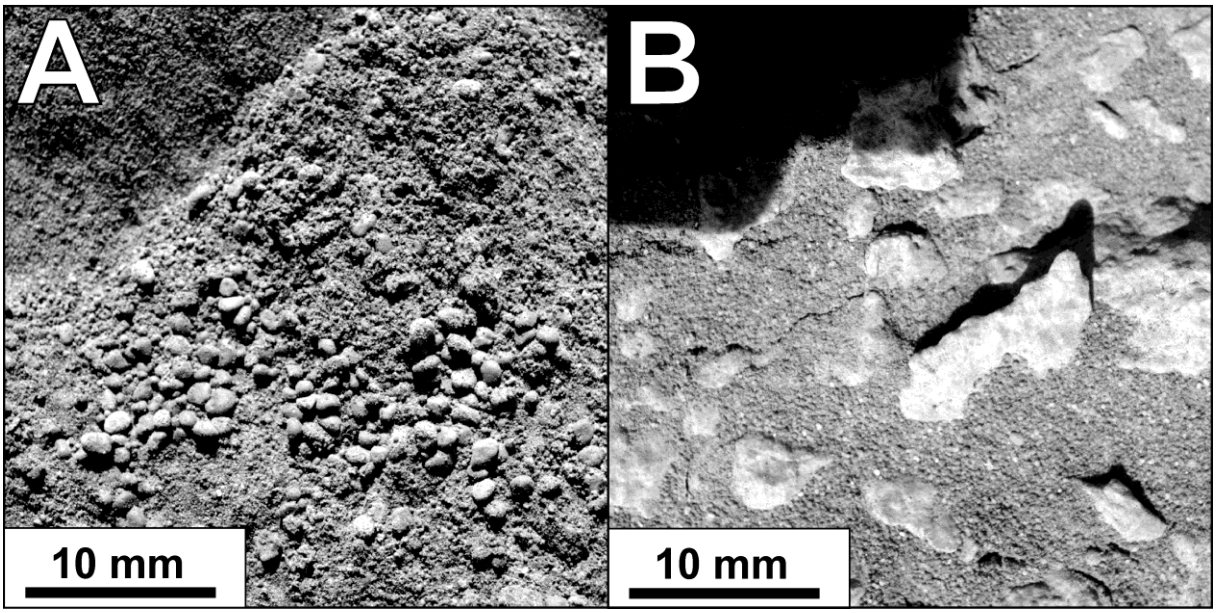

Figure 2.9. MI images of bimodal mixed soils. (A) Mixture of dark soil and bed form armor (Bear Paw, sol 73); (B) bimodal mixtures of dark soil and lithic fragment pebbles (Almond Crumble, sol 460). Saltation is insufficient to remove fine sand and the concentration of coarse sand by armoring is incomplete.

Bimodal mixed soils are interpreted as a combination of fine and coarse sand from dark soil and bed form armor soils that have not been sufficiently separated by saltation and creep (Figure 2.7D). Saltation alone was inefficient in removing dark soil sand, and deflation or aggradation was incomplete in concentrating an armored surface (Figure 2.7D). Grain size (Figure 2.3H), shape (Figure 2.10), and roundness of bimodal mixed soils (Table 2.1) exhibit inherited heterogeneity that we interpret as the mixing of several populations. The mean grain size distribution of bimodal mixed soils can be reconstructed (Figure 2.3H) by combining the mean distributions of other soil classes, in the proportions of 70% dark soil, 25% bed form armor, and 5% lithic fragments. Most bimodal mixed soil samples (sols 73, 480, 499, 812, 822) contain fine to medium sand from the dark soil and coarse sand from bed form armor classes. The relative abundances of dark soil and bed form armor grains vary among samples.

In addition to grain sizes (Figure 2.3H), the shapes of grains in bimodal mixed soils also correspond to the shapes of grains in dark soil, bed form armor, and lithic fragment soil classes. Grains of each bimodal mixed soil were separated into coarse ($\geq 0\ \phi$) and fine ($<0\ \phi$) grains to account for differences in grain sizes and shapes (Figure 2.10). The mean sphericity of the coarse and fine groups are used to represent the bimodal distributions present in bimodal mixed samples and are compared to the mean grain size, form, and sphericity [Anthony and Héquette, 2007; Bullard et al., 2004; Blott and Pye, 2008] of dark soil, bed form armor, and lithic fragment soils. The fine fraction ($< 0\ \phi$) of grains in bimodal mixed soils consists of medium sand grains with equant form similar to dark soils. Two samples (sols 812, 822) are subequant with lower sphericity than the mean sphericities of dark soils. The mixture of dark soil and bed form amour soils is supported by the shape of very coarse sand and very fine pebbles in five (sols 73, 480,

499, 812, 822) bimodal mixed soils. The coarse fraction ($\geq 0\ \phi$) of the five bimodal mixed soils samples have the same very equant form as all bed form armor soils (Figure 2.10). Very coarse sand to medium pebble grains in Almond Crumble (460) have the lowest sphericity of all bimodal mixed soils with intermediate shape, similar to clasts in lithic fragment soils.

Roundness estimates of grains in bimodal mixed soils are variable ($\rho = 4.1$ to 4.9) with the same range in rounding observed with soil types (Figure 2.4C). Bimodal mixed soils reflect source material with more than one mode, or the mixing of sediments from different sources. Each mode is identified by grain size range and sphereicity (Figure 2.10) which is interpreted to represent the incomplete separation of fine dark soil type sand by saltation and the concentration of creep-driven bed form armor type coarse sand (Figure 2.7D).

3.5. Excavated Subsurface Soil

3.5.1. Description

Images of most soils only represent the uppermost surface grains, providing a perspective of the surface area, but not the three-dimensional volume perspective from which to examine the vertical distributions of textural variations [cf. Clemmensen and Abrahamsen, 1983, Figure 10A]. As observed in armored soils (Figure 2.8C), surface textures that are reworked by aeolian transport and abrasion may be distinct from subsurface material. Textural data collected from subsurface grains provide insight beyond only surficial activity. A vertical soil profile in Gusev crater, at sol 428, was examined from an exposed slope with a depth

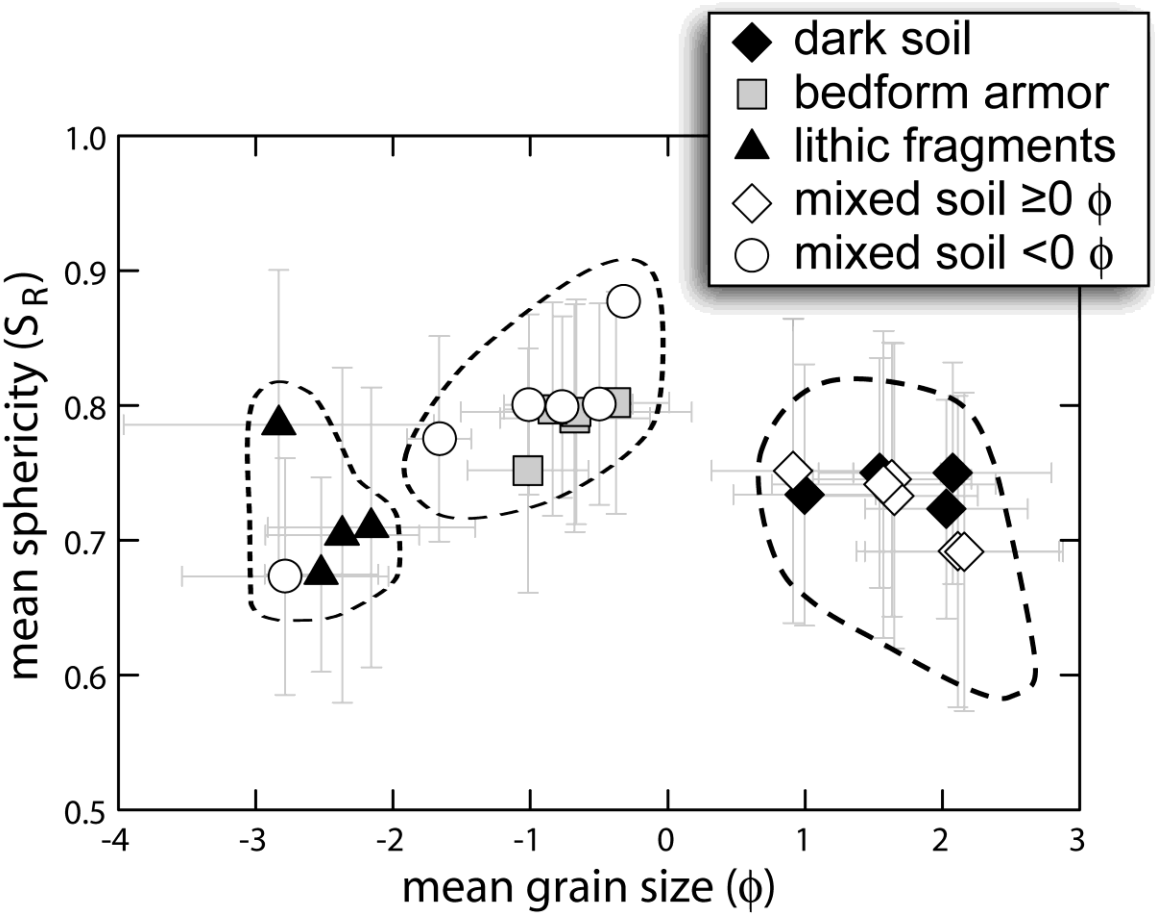

Figure 2.10. Mean fine (≥0 ϕ) and coarse (<0 ϕ) fractions of bimodal mixed soil particles are separated to compare against other soil types. The sphericities and grain sizes of bimodal mixed soils are similar to three groups: dark soil, bed form armor, and lithic fragment soils, denoted by dashed fields. Error bars represent one standard deviation.

equivalent of < 10 mm. In one image (Figure 2.11A), grains were measured at three areas of the Paso Dark [Lane et al., 2008; Morris et al., 2008; Parente et al., 2009; Wang et al., 2008] subsurface soil target, corresponding to a depressed layer compacted by the Mössbauer contact plate, with few pebble size clasts and with void spaces filled by subrounded fine sand (grid 1; Figure 2.11C), an upper unconsolidated layer of very poorly sorted, subangular, very fine to very coarse sand (grid 2; Figure 2.11D), and a collapsed slope of subangular very fine pebbles with large void spaces between grains (grid 3; Figure 2.11E). Each subset is very poorly sorted with a grain size range from 4.32 to 4.91 ϕ. Mean sphericities in all three subsets are equant (S_R = 0.72 to 0.74, Table 2.1). The mean roundness of grains varies from subrounded (ρ = 4.0) in grid 1 to subangular (ρ = 3.3) in grids 2 and 3 (Figure 2.4C).

When treating the portions of the image in isolation, based on mean grain size alone, each subset is dissimilar to the original soil types of Yen et al. [2005]. However, when incorporating the shape of the grain size distribution with mean grain size, each subset begins to resemble other soil types. Based on histogram peaks, the depressed and surface layers (grid 1, grid 2) with medium sand would be classified as dark soils (Figure 2.11C). The cumulative frequency distribution of dark soil is similar to the depressed layer (grid 1), with the disturbed soil distribution shifted with a higher proportion of finer sand. Grain sizes in the collapsed slope (grid 3), are similar in grain size and grain size distribution to lithic fragment soils. Very fine pebbles in grid 3 are coarser (−1 ϕ) than the typical peak center for bed form armor (0 ϕ) and do not have a bimodal distribution characteristic of bimodal mixed soils. Although

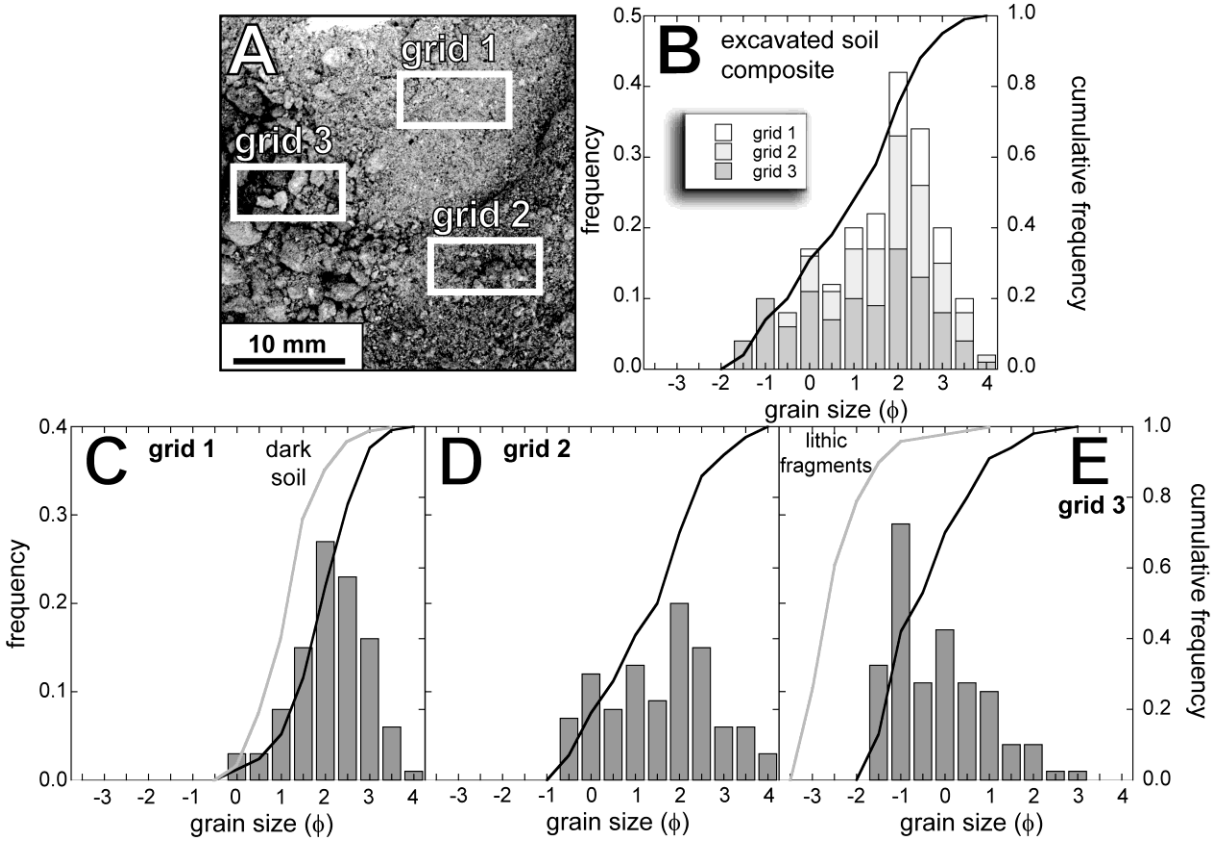

Figure 2.11. MI image and grain size histograms (frequency and cumulative frequency) for Paso Dark excavated soil. (A) Image of Paso Dark (sol 428) subsurface soil and location of three subsample grids (1–3); (B) composite soil histogram for all three grids (note similarity with grid 2); (C) histogram for grid 1 (gray line represents cumulative frequency curve for dark soil for comparison); (D) histogram for grid 2; (E) histogram for grid 3 (gray line represents cumulative frequency curve for lithic fragment soil for comparison).

each subset of the Paso Dark image is not homogeneous in grain size, each is similar in shape and sphericity (Figures 2.4B and 2.4C). A composite histogram (Figure 2.11B) formed by combining the three subsets, which includes subsurface material (grid 3), provides a more accurate grain size distribution of the Paso Dark soil than what would otherwise be observed with surface measurements (grid 2).

3.5.2. Interpretation and the Importance of Subsurface Textural Analysis

The purpose of examining the Paso Dark excavated subsurface soil is to (1) examine the disconnect between surface and subsurface textures, (2) demonstrate the transient nature between soil types, (3) provide a depth profile from which to better characterize the overall textures in soils that are typically obscured by surface dust or armoring (Figure 2.7E), and (4) compare the composite grain size distribution of subsurface soil with terrestrial and lunar analogs (section 4).

The occurrence of distinct soils (Figures 2.11C–2.11E), located within a small surface area (~10 mm), and with a small vertical separation (<10 mm) highlights small-scale stratigraphy and the variations of subsurface textures that are not represented from imaging surface textures only. Very coarse sand and very fine pebbles in grid 3 (Figure 2.11E) have been overlain by finer sand and are not visible in grids 1 and 2; this demonstrates the disconnect between surface grains reworked by more recent aeolian transported material (grid 2) and subsurface material (grid 3). Vertical variations in grain sizes are also observed elsewhere, such as in armored soils (Figure 2.8C), where surface textures, reworked by aeolian transport, are distinct from subsurface material.

Soil types are largely controlled by the intensity and duration of aeolian activity and transitions between soil types are expected, as observed in the abundance of bimodal mixed soils throughout the Sprit rover traverse (Figure 2.6), and similarities in the disturbed soil subsets. Each subset of the disturbed soil is interpreted to represent physical formation processes similar to processes associated with dark soil and lithic fragment soil classes. Sand in grid 1 is transported and abraded by saltation similar to dark soils. Grid 2 also contains a saltation transported sand component in addition to creep driven very coarse sand. Grid 3 represents creep driven very coarse sand to very fine pebbles in addition to a finer sand saltation component. Compared to undisturbed surface soil, the subrounded disturbed soil represents a reduction in the degree of aeolian transport, and is possibly sheltered from sandblasting abrasion by burial. Textural differences between the disturbed soil subsets, in such close proximity, are the result of the most recent aeolian event to transport and abrade soil grains.

The lack of a complete vertical profile in Gusev soils highlights the need for a future landed mission to disturb soils and expose more vertical range. Stirring the upper tens of cm of sediment could provide a future basis for vertical soil analysis. Such subsurface soils would represent formation processes for current soils, but also represent past formation mechanisms that cannot currently be evaluated. The interpretation of soil textures can be limited by modern aeolian processes, but mixing surface and subsurface material (Figures 2.7F and 2.11B) can provide a direct method to evaluate a fuller spectrum of grains within a volume of soil.

4. Soil Formation in Gusev Crater

A three-step model, initiated by the formation of basaltic crust and its alteration, followed by bolide impact, and lastly modification by aeolian reworking is envisioned for the formation of soils.

4.1. Step 1: Surface Formation

Despite some uncertainties in the age, textural, and compositional characteristics of soil component source material, the genesis and modification of Martian soils can be directly evaluated from textural properties of soils in Gusev crater. Although not discussed in detail here, basalt is considered to represent the primary bedrock source material [Yen et al., 2006; McSween et al., 2009, 2010]. A growing body of evidence indicates that chemical weathering affected the basaltic crust leading to the generation of at least some phyllosilicates [e.g., Hamilton et al., 2005; Clark et al., 2007; Bishop et al., 2008; Ehlmann et al., 2009; McKeown et al., 2009], in addition to evaporates [Yen et al., 2005]. Volcaniclastic material [Bibring et al., 2006] may have formed part of the crust as well as ejecta from a history of previous impacts, all adding to form a complex bedrock template from which Gusev crater soils were derived (Figure 2.12A).

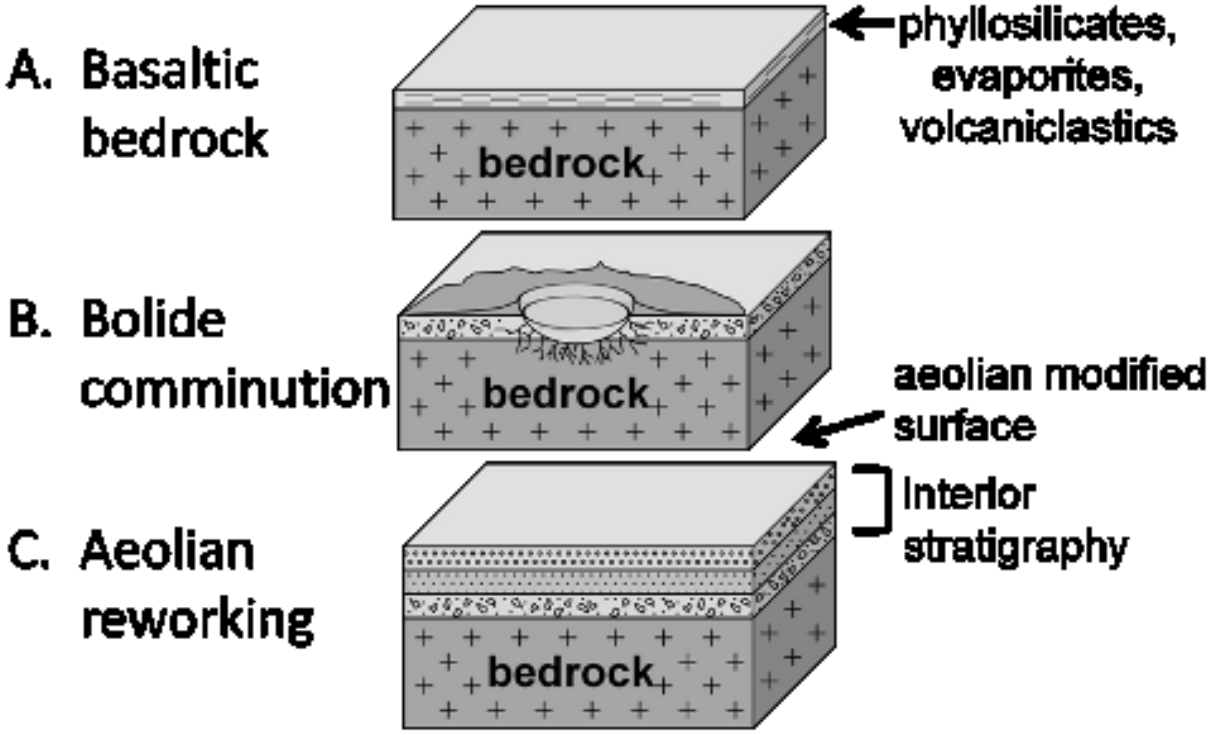

Figure 2.12. Sequence of formation for soils in Gusev crater. (A) Bedrock template consisting of basaltic crustal material with chemically weathered components, evaporates, volcaniclastic material, and older impact ejecta; (B) surface comminution by bolide impacts, creating angular unconsolidated material with a Rosin grain size distribution; (C) aeolian reworking of crushed detritus becomes rounded and transported on the surface, concentrating and sorting grains into different soil types.

4.2. Step 2: Comminution

The surfaces of most bodies in the solar system including Mars [Knauth et al., 2005; Barlow, 2010], bear the scars of repeated bolide impacts. If Gusev soils were produced entirely from impact comminuted basaltic material, then soils might match the grain size distributions of angular sediments as lunar soils [King, 1977]. Lunar soils in Apollo 11, 12, 14, 15, and 16 core tubes [Duke et al., 1970; King and Butler, 1977] provide direct measurements of soils from another body and a basis from which to compare the distribution of Gusev soils, and have a characteristic grain size distribution that [Duke et al., 1970] does not conform to a single Rosin distribution [King and Butler, 1977]. Poorly and very poorly sorted lunar soils ($\Delta\phi$ = 1.99 to 3.73) from very coarse silt to coarse sand (0 ϕ to 4.76 ϕ) plot in agreement with a Rosin Distribution, but smaller grains of coarse to medium silt exhibit a steeper slope (Figure 2.5F) that deviates from a Rosin distribution. The bimodal samples yield clues to the origin of lunar soils: destructive comminution forces of meteorite impacts have decreased the mean size of soil grains, while constructive forces of impacts have produced agglutinates and increased the size of particles [Duke et al., 1970; King and Butler, 1977]. Coarse clasts of rock fragments and agglutinates comprise the modality of coarse grains (1 ϕ to 4 ϕ) that conform to a Rosin distribution.

Grain size distributions of measured Gusev soils (Figures 2.5A–2.5D) are not similar to the clear bimodal grain size distributions in lunar soils (Figure 2.5F). Bimodal patterns in lunar soils are not diagnostic of an impact origin, but also reflected the nature of igneous materials melted by impacts and the fragmentation of lithic clasts. Fine agglutinates of glassy particles found on the Moon might be present in Martian soil, but they are not visible in the available MI images

[Sullivan et al., 2008]. The apparent absence of visible agglutinates in Martian soil may indicate post-Noachian weathering and burial, or the presence of a limited atmosphere to prevent micrometeorite impacts necessary for agglutinate formation. The absence of bimodal populations of grains with agglutinates, and the presence of mostly rounded grains indicate Gusev soils were not exclusively derived from impacts like the lunar counterparts.

Sediments produced solely from physical crushing, such as bolide impacts, have a characteristic grain size distribution conforming to the Weibull (Rosin) Distribution [Rosin and Rammler, 1933], that can be replicated and applied regardless of source material composition or crystal size [McEwen et al., 1959; Kittleman, 1964; Brown and Wohletz, 1995]. Crushed samples of granite and quartz (Figure 2.5F) are used here as analogs of bolide impacts, absent of agglutinates, to be compared with Gusev soils (Figures 2.5A-E). Size frequency distributions for crushed samples were determined from published analyses of crushed sediments collected by Kittleman [1964]. The probability distributions of experimentally crushed sediments (Figure 2.5F) differ from those of all Gusev surface soils. Dark soil and bed form armor soil distributions (Figures 2.5A and 2.5B) lack the coarse fraction $<-1\ \phi$ of the analog samples, and have a concentrated range where 50% of grains are within $\Delta\phi = 1$. The lithic fragment samples have a high concentration of pebbles with few sand size grains (Figure 2.5C). The separation between the modes in bimodal mixed soil samples (Figure 2.5D) is not present in the unimodal analogs distributions.

Only the probability distribution of the excavated composite Paso Dark subsurface soil (Figure 2.5E), trenched by the rover wheel and compressed by the Mössbauer contact plate, approximates the distribution of crushed analogs. With the addition of coarse sand and pebbles from the exposed subsurface (Figure 2.12D), the probability distribution of the composite soil (bold dashed line, Figure 2.5E) is similar to a distribution produced from physical crushing (bold line, Figure 2.5F), such as from bolide impacts (Figure 2.12B). The probability distribution of all other measured soils in Gusev crater is distinct from crushed analogs, and indicates subsequent modification of impact generated sediment.

4.3. Step 3: Aeolian Modification

Unlike on the Moon, wind is a major surface process on Mars that can modify surface material that is well characterized in numerous reports [Greeley et al., 1999, 2003, 2004, 2006a; Sullivan et al., 2005, 2008]. After sediments are comminuted by bolide impacts (Figure 2.12B), loose soil material is reworked by aeolian activity as demonstrated with the interpretation of textures for each soil type in section 3, including saltation, creep, and abrasion. The reworking of surface textures by selective sorting, concentration into ripples, or burial by dust deposition alters the original grain size distributions from comminution. Differences in soil types at Gusev crater are the primary result of the intensity and duration of aeolian activity and do not reflect possible subsurface stratigraphy that is observed in exhumed soil (Figure 2.7E). Wind has been generally incomplete in sorting sediments within Gusev crater. Soils classifications are invariably irrelevant, with transitions between soils types transitory, dependent upon present aeolian conditions, and disconnected from potential subsurface stratigraphy (Figure 2.7F).

5. Conclusions

Soil samples imaged from surface deposits at Gusev crater suggest the presence of four distinct populations: a fine to medium pebble population of "lithic fragments" of basaltic clasts, a medium to very coarse sand "bed form armor" in coarse ripples, a fine to medium sand low-albedo "dark soil," and a high-albedo layer of ubiquitous "bright dust" containing an indeterminate amount of silt. The mixing of multiple sediment populations in bimodal mixed soils represents incomplete separation of sand by saltation and the incomplete concentration of coarse grains by creep.

Sedimentary textures of soils, on the surface of Mars, are independent from subsurface textures as observed in the trenched Paso Dark excavated subsurface soil, and are independent from subsurface strata that may have been formed and modified by depositional or erosional processes at different times since the formation of Gusev crater. Surface modification by wind occurs regardless of the subsurface distribution of sedimentary textures, or alteration mechanisms related to the physical and chemical weathering of bedrock and soil formation. An accurate assessment of chemical weathering and leaching of soil should involve a vertical profile, which itself indicates the potential value for depth analysis and volume investigations during future landed missions. Models to reconstruct soil properties should not assume a static surface, and surface textures should not be assumed to extend at depth.

Differences in soil types are the product of modern aeolian reworking of surface textures. Grain size variations primarily result from surface modification of textures by saltation, creep, and

selective sorting. As such, rock surface textures are not linked to soil formation processes other than recent abrasion and comminution by sandblasting. Despite potential exposure to aeolian transport for billions of years, wind in Gusev crater has been insufficient to produce well sorted soils in observed images.

An impact origin of comminution is supported by the grain size distribution of the composite Paso Dark subsurface soil, which is not observed in other soil samples throughout Gusev crater. Grains on the surface of Gusev crater are sandblasted, transported, and modified by aeolian processes, and have subsequently obscured evidence of an impact formation. If soils were produced primarily by impacts that reshaped the surface, evidence from probability distributions, angular shapes, and agglutinates have been reworked by postimpact surface activity. As such, wind acting as a geologic agent has obscured the comminution mechanism of soil formation in Gusev crater.

6. Acknowledgments

This work was partly supported by a NASA Mars Exploration Rovers grant through Cornell subcontract 39361–6446 to H.Y.M. The authors are grateful to the MER Athena Science team, including K. E. Herkenhoff for assistance in obtaining MI data and R. Li and O. Karahayit for contributions with the Spirit traverse map. We thank E. Simpson for making helpful suggestions on the manuscript. We thank two anonymous reviewers who gave helpful and constructive advice to improve the quality of this manuscript.

References

Almeida, M. P., E. J. R. Parteli, J. S. Andrade, and H. J. Herrmann (2008), Giant saltation on Mars, *Proc. Natl. Acad. Sci. U. S. A., 105*, 6222–6226, doi:10.1073/pnas.0800202105.

Amundson, R., et al. (2008), On the in situ aqueous alteration of soils on Mars, *Geochim. Cosmochim. Acta, 72*, 3845–3864, doi:10.1016/j.gca.2008.04.038.

Anthony, E. J., and Héquette, A. (2007), The grain size characterization of coastal sand from the Somme estuary to Belgium: Sediment sorting processes and mixing in a tide- and storm-dominated setting, *Sediment. Geol., 202*, 369–382, doi:10.1016/j.sedgeo.2007.03.022.

Arvidson, R. E., et al. (2006), Overview of the Spirit Mars Exploration Rover Mission to Gusev crater: Landing site to Backstay Rock in the Columbia Hills, *J. Geophys. Res., 111*, E02S01, doi:10.1029/2005JE002499.

Arvidson, R. E., et al. (2008), Spirit Mars Rover Mission to the Columbia Hills, Gusev crater: Mission overview and selected results from the Cumberland Ridge to Home Plate, *J. Geophys. Res., 113*, E12S33, doi:10.1029/2008JE003183.

Bagnold, R. A. (1941), *The Physics of Blown Sand and Desert Dunes*, 265 pp., Chapman and Hall, London.

Barlow, N. G. (2010), What we know about Mars from its impact craters, *Geol. Soc. Am. Bull., 57*, 1338–1345, doi:10.1016/j.pss.2009.06.006.

Batt, R. G., and Peabody, S. A. (1999), Threshold friction velocities for large pebble gravel beds, *J. Geophys. Res., 104*(D20), 24,273–24,279, doi:10.1029/1999JD900484.

Benn, D. I., and Ballantyne, C. K. (1993), The description and representation of particle shape, *Earth Surf. Processes Landforms, 18*, 665–672, doi:10.1002/esp.3290180709.

Bibring, J.-P., et al. (2006), Global mineralogical and aqueous mars history derived from OMEGA/Mars Express data, *Science, 312*, 400–404, doi:10.1126/science.1122659.

Bishop, J. L., et al. (2008), Phyllosilicate diversity and past aqueous activity revealed at Mawrth Vallis, Mars, *Science, 321*, 830–833, doi:10.1126/science.1159699.

Blott, S. J., and Pye, K. (2008), Particle shape: A review and new methods of characterization and classification, *Sedimentology, 55*, 31–63, doi:10.1111/j.1365-3091.2007.00892.x.

Bridges, N. T., Razdan, A. Yin, X. T., Greeley, R., Ali, S. and Kushunapally, R. (2010), Quantification of shape and texture for wind abrasion studies: Proof of concept using analog targets, *Geomorphology, 114*, 213–226, doi:10.1016/j.geomorph.2009.07.002.

Brown, W. K., and Wohletz, K. H. (1995), Derivation of the Weibull distribution based on physical principles and its connection to the Rosin-Rammler and lognormal distributions, *J. Appl. Phys., 78*, 2758–2763, doi:10.1063/1.360073.

Bullard, J. E., McTainsh, G. H., and Pudmenzky, C. (2004), Aeolian abrasion and modes of fine particle production from natural red dune sands: An experimental study, *Sedimentology, 51*, 1103–1125, doi:10.1111/j.1365-3091.2004.00662.x.

Bullard, J. E., McTainsh, G. H., and Pudmenzky, C. (2007), Factors affecting the nature and rate of dust production from natural dune sands, *Sedimentology, 54*, 169–182, doi:10.1111/j.1365-3091.2006.00827.x.

Buscombe, D., Rubin, D. M., and Warrick, J. A. (2010), A universal approximation of grain size from images of noncohesive sediment, *J. Geophys. Res., 115*, F02015, doi:10.1029/2009JF001477.

Cabrol, N. A., et al. (2008), Soil sedimentology at Gusev crater from Columbia Memorial Station to Winter Haven, *J. Geophys. Res., 113*, E06S05, doi:10.1029/2007JE002953.

Cheetham, M. D., Keene, A. F., Bush, R. T., Sullivan, L. A., and Erskine, W. D. (2008), A comparison of grain size analysis methods for sand-dominated fluvial sediments, *Sedimentology, 55*, 1905–1913, doi:10.1111/j.1365-3091.2008.00972.x.

Cho, G. Dodds, C. J., and Santamarina, J. C. (2006), Particle shape effects on packing density, stiffness, and strength: Natural and crushed sands, *J. Geotech. Geoenviron. Eng., 132*, 591–602, doi:10.1061/(ASCE)1090-0241(2006)132:5(591).

Chojnacki, M., Burr, D. M., Moersch, J. E. and Michaels, T. I. (2011), Orbital observations of contemporary dune activity in Endeavour crater, Meridiani Planum, Mars, *J. Geophys. Res., 116,* E00F19, doi:10.1029/2010JE003675.

Chyba, C. F. (1993), The violent environment of the origin of life: Progress and uncertainties, *Geochim. Cosmochim. Acta, 57*, 3351–3358, doi:10.1016/0016-7037(93)90543-6.

Clark, B. C., et al. (2007), Evidence for montmorillonite or its compositional equivalent in Columbia Hills, Mars, *J. Geophys. Res., 112*, E06S01, doi:10.1029/2006JE002756.

Clemmensen, L. B., and Abrahamsen, K. (1983), Aeolian stratification and facies association in desert sediments, Arran basin (Permian), Scotland, *Sedimentology, 30*, 311–339, doi:10.1111/j.1365-3091.1983.tb00676.x.

Davidson-Arnott, R. G. D., White, D. C., and Ollerhead, J. (1997), The effects of artificial pebble concentrations on eolian sand transport on a beach, *Can. J. Earth Sci., 34*, 1499–1508.

Duke, M. B., Woo, C. C., Bird, M. L., Sellers, G. A. and Finkelma, R. B. (1970), Lunar soil: Size distribution and mineralogical constituents, *Science, 167*, 648–650, doi:10.1126/science.167.3918.648.

Ehlmann, B. L., et al. (2009), Identification of hydrated silicate minerals on Mars using MRO-CRISM: Geologic context near Nili Fossae an implications for aqueous alteration, *J. Geophys. Res., 114*, E00D08, doi:10.1029/2009JE003339.

Folk, R. L. (1981), *Petrology of Sedimentary Rocks*, 2nd ed., 182 pp., Hemphill, Austin, Tex.

Gellert, R., et al. (2004), Chemistry of rocks and soils in Gusev crater from the Alpha Particle X-ray Spectrometer, *Science, 305*, 829–832, doi:10.1126/science.1099913.

Gillette, D. A., and Chen, W. N. (1999), Size distributions of saltating grains: An important variable in the production of suspended particles, *Earth Surf. Processes Landforms, 24*, 449–462, doi:10.1002/(SICI)1096-9837(199905)24:5<449::AID-ESP1>3.0.CO;2-E.

Greeley, R., Leach, R. White, B., Iversen, J., and Pollack, J. (1980), Threshold windspeeds for sand on Mars: Wind tunnel simulations, *Geophys. Res. Lett., 7*, 121–124, doi:10.1029/GL007i002p00121.

Greeley, R., et al. (1999), Aeolian features and processes at the Mars Pathfinder landing site, *J. Geophys. Res., 104(*E4), 8573–8584, doi:10.1029/98JE02553.

Greeley, R., Kuzmin,, R. O., Rafkin, S. C. R., Michaels, T. I. and Haberle, R. (2003), Wind-related features in Gusev crater, Mars, *J. Geophys. Res., 108*(E12), 8077, doi:10.1029/2002JE002006.

Greeley, R., et al. (2004), Wind-related processes detected by the Spirit rover at Gusev crater, Mars, *Science, 305*, 810–813, doi:10.1126/science.1100108.

Greeley, R., et al. (2006a), Gusev crater: Wind-related features and processes observed by the Mars Exploration Rover Spirit, *J. Geophys. Res., 111*, E02S09, doi:10.1029/2005JE002491.

Greeley, R., et al. (2006b), Active dust devils in Gusev crater, Mars: Observations from the Mars Exploration Rover Spirit, *J. Geophys. Res., 111*, E12S09, doi:10.1029/2006JE002743.

Hamilton, V. E., McSween, H. Y. Jr., and Hapke, B. (2005), Mineralogy of Martian atmospheric dust inferred from thermal infrared spectra of aerosols, *J. Geophys. Res., 110*, E12006, doi:10.1029/2005JE002501.

Harrell, J. A., and Eriksson, K. A. (1979), Empirical conversion equations for thin section and sieve derived size distribution parameters, *J. Sediment. Res., 49*, 273–280, doi:10.1306/212F7711-2B24-11D7-8648000102C1865D.

Herkenhoff, K. E., et al. (2004), Textures of the soils and rocks at Gusev crater from Spirit's Microscopic Imager, *Science, 305*, 824–826, doi:10.1126/science.3050824.

Ibbeken, H. (1983), Jointed source rock and fluvial gravels controlled by Rosin's law: A grain size study in Calabria, south Italy, *J. Sediment. Petrol., 53*, 1213–1231.

Ingersoll, R. V., Bullard, T. F.., Ford, R. L., Grimm, J. P., Pickle, J. D., and Sares, S. W. (1984), The effect of grain size on Detrital modes: A test of the Gazzi-Dickinson point-counting method, *J. Sediment. Petrol., 54*, 103–116.

Jerolmack, D. J., Mohrig, D., Grotzinger, J. P., Fike, D. A., and Watters, W. A. (2006), Spatial grain size sorting in eolian ripples and estimation of wind conditions on planetary surfaces: Application to Meridiani Planum, Mars, *J. Geophys. Res., 111*, E12S02, doi:10.1029/2005JE002544.

Khalaf, F. I., and Gharib, I. M. (1985), Roundness parameters of quartz grains of recent aeolian sand deposits in Kuwait, *Sediment. Geol., 45*(1–2), 147–158, doi:10.1016/0037-0738(85)90028-4.

King, E. A. (1977), The lunar regolith: Physical characterisics and dynamics, *Philos. Trans. R. Soc. London, A, 285,* 273–278, doi:10.1098/rsta.1977.0065.

King, E. A., and Butler, J. C. (1977), Rosin's law and the lunar regolith, *Moon, 17*, 177–178, doi:10.1007/BF00640907.

Kittleman, L. R. (1964), Application of Rosin's distribution in size frequency analysis of clastic rocks, *J. Sediment. Petrol., 34*, 483–502.

Kleinhans, M. G. (2005), Grain size sorting in grain flows at the lee side of deltas, *Sedimentology, 52*, 291–311, doi:10.1111/j.1365-3091.2005.00698.x.

Knauth, L. P., Burt, D. M., and Wohletz, K. H. (2005), Impact origin of sediments at the opportunity landing site on Mars, *Nature, 438*, 1123–1128, doi:10.1038/nature04383.

Knoll, A. H., et al. (2008), Veneers, rinds, and fracture fills: Relatively late alteration of sedimentary rocks at Meridiani Planum, Mars, *J. Geophys. Res., 113*, E06S16, doi:10.1029/2007JE002949.

Kok, J. F. (2010), Difference in the wind speeds required for initiation versus continuation of sand transport on Mars: Implications for dunes and dust storms, *Phys. Rev. Lett., 104*(7), 074502, doi:10.1103/PhysRevLett.104.074502.

Laity, J. E., and Bridges, N. T. (2009), Ventifacts on Earth and Mars: Analytical, field, and laboratory studies supporting sand abrasion and windward feature development, *Geomorphology, 105*, 202–217, doi:10.1016/j.geomorph.2008.09.014.

Lane, M. D., Bishop, J. L. Dyar, M. D., King, P. L. Parente, M., and Hyde, B. C. (2008), Mineralogy of the Paso Robles soils on Mars, *Am. Mineral., 93*, 728–739, doi:10.2138/am.2008.2757.

Liu, Y., Park, J. Schnare, D. Hill, E. and Taylor, L. (2008), Characterization of lunar dust for toxicological studies. II: Texture and shape characteristics, *J. Aerosp. Eng., 21*, 272–279, doi:10.1061/(ASCE)0893-1321(2008)21:4(272).

Lucey, P., et al. (2006), Understanding the lunar surface and space-Moon interactions, *Rev. Mineral. Geochem., 60*, 83–219, doi:10.2138/rmg.2006.60.2.

Mason, C. C. (1971), Nature of the Martian surface as inferred from the particle size distribution of lunar surface material, *Geol. Soc. Am. Bull., 82*, 2625–2630, doi:10.1130/0016-7606(1971)82[2625:NOTMSA]2.0.CO;2.

McEwen, M. C., Fessenden, F. W., and Rogers, J. J. W. (1959), Texture and composition of some weathered granites and slightly transported arkosic sands, *J. Sediment. Petrol., 29*, 477–492.

McGlynn, I. O., and Okin, G. S. (2006), Characterization of shrub distribution using high spatial resolution remote sensing: Ecosystem implications for a former Chihuahuan Desert grassland, *Remote Sens. Environ., 101*, 554–566, doi:10.1016/j.rse.2006.01.016.

McKeown, N. K., et al. (2009), Characterization of phyllosilicates observed in the central Mawrth Vallis region, Mars, their potential formational processes, and implications for past climate, *J. Geophys. Res., 114*, E00D10, doi:10.1029/2008JE003301.

McLennan, S. M., et al. (2005), Provenance and diagenesis of the evaporite-bearing Burns formation, Meridiani Planum, Mars, *Earth Planet. Sci. Lett., 240*, 95–121, doi:10.1016/j.epsl.2005.09.041.

McSween, H. Y., Taylor, G. J., and Wyatt, M. B. (2009), Element composition of the Martian crust, Science, 324, 736–739, doi:10.1126/science.1165871.

McSween, H. Y., McGlynn, I. O., and Rogers, A. D. (2010), Determining the modal mineralogy of Martian soils, *J. Geophys. Res., 115*, E00F12, doi:10.1029/2010JE003582.

Morris, R. V., et al. (2008), Iron mineralogy and aqueous alteration from Husband Hill through Home Plate at Gusev crater, Mars: Results from the Mössbauer instrument on the Spirit Mars Exploration Rover, *J. Geophys. Res., 113*, E12S42, doi:10.1029/2008JE003201.

Mulder, T., and Alexander, J. (2001), The physical character of subaqueous sedimentary density flows and their deposits, *Sedimentology, 48*, 269–299, doi:10.1046/j.1365-3091.2001.00360.x.

Nickling, W. G., and McKenna Neuman, C. (2009), *Geomorphology of Desert Environments*, 2nd ed., edited by A. J. Parsons and A. D. Abrahams, Springer, New York.

Parente, M., Bishop, J. L., and Bell, J. F. (2009), Spectral unmixing for mineral identification in pancam images of soils in Gusev crater, Mars, *Icarus, 203*, 421–436, doi:10.1016/j.icarus.2009.04.029.

Parteli, E. J. R., Almeida, M. P., Duran, O., Andrade, J. S., and Herrmann, H. J. (2009), Sand transport on Mars, *Comput. Phys. Commun., 180*, 609–611, doi:10.1016/j.cpc.2008.12.024.

Pettijohn, F. J., Potter, P. E., and Siever, R. (1987), *Sand and Sandstone*, 2nd ed., 553 pp., Springer, New York.

Powers, M. C. (1953), A new roundness scale for sedimentary particles, *J. Sediment. Petrol., 23*, 117–119.

Purkait, B. (2006), Grain size distribution patterns of a point bar system in the Usri River, India, *Earth Surf. Processes Landforms, 31*, 682–702, doi:10.1002/esp.1290.

Pye, K., and Tsoar, H. (1990), Aeolian Sand and Sand Dunes, 1st ed., 458 pp., Springer, New York.

Rosin, P., and Rammler, E. (1933), The laws governing the fineness of powdered coal, *J. Inst. Fuel, 7*, 29–36.

Saltikov, S. A. (1967), The determination of the size distribution of particles in an opaque material from a measurement of the size distributions of their sections, in *Proceedings of the 2nd International Congress for Stereology*, edited by H. Elias, pp. 163–173, Int. Union of Crystallogr., Chester, U. K.

Shao, Y. (2000), *Physics and Modelling of Wind Erosion*, 393 pp., Kluwer Acad., Dordrecth, Netherlands.

Squyres, S. W., et al. (2004), The Spirit Rover's Athena Science Investigation at Gusev crater, Mars, *Science, 305*, 794–799, doi:10.1126/science.3050794.

Stevens, R. L., Bengtsson, H., and Lepland, A. (1996), Textural provinces and transport interpretations with fine-grained sediments in the Skagerrak, *J. Sea Res., 35*, 99–110, doi:10.1016/S1385-1101(96)90739-X.

Strom, K. B., Kuhns, R. D., and Lucas, H. J. (2010), Comparison of automated image-based grain sizing to standard pebble-count methods, *J. Hydraul. Eng., 136*, 461–473, doi:10.1061/(ASCE)HY.1943-7900.0000198.

Sullivan, R., et al. (2005), Aeolian processes at the Mars Exploration Rover Meridiani Planum landing site, *Nature, 436*, 58–61, doi:10.1038/nature03641.

Sullivan, R., et al. (2008), Wind-driven particle mobility on mars: Insights from Mars Exploration Rover observations at "El Dorado" and surroundings at Gusev crater, *J. Geophys. Res., 113*, E06S07, doi:10.1029/2008JE003101.

van der Plas, L., and Tobi, A. C. (1965), A chart for judging reliability of point counting results, *Am. J. Sci., 263*, 87–90, doi:10.2475/ajs.263.1.87.

Wang, A., et al. (2008), Light-toned salty soils and coexisting Si-rich species discovered by the Mars Exploration Rover Spirit in Columbia Hills, *J. Geophys. Res., 113*, E12S40, doi:10.1029/2008JE003126.

Yang, S. L., and Ding, Z. L. (2004), Comparison of particle size characteristics of the Tertiary 'red clay' and Pleistocene loess in the Chinese Loess Plateau: Implications for origin and sources of the 'red clay', *Sedimentology, 51*, 77–93, doi:10.1046/j.1365-3091.2003.00612.x.

Yen, A. S., et al. (2005), An integrated view of the chemistry and mineralogy of Martian soils, *Nature, 436*, 49–54, doi:10.1038/nature03637.

Yen, A. S., et al. (2006), Nickel on Mars: Constraints on meteoritic material at the surface, *J. Geophys. Res., 111*, E12S11, doi:10.1029/2006JE002797.

Yingst, R. A., Crumpler, L. Farrand, W. H. Li, R., Cabrol, N. A., and Neakrase, L. D. (2008), Morphology and texture of particles along the Spirit rover traverse from sol 450 to sol 745, *J. Geophys. Res., 113*, E12S41, doi:10.1029/2008JE003179.

Zimbelman, J. R., Irwin, R. P., Williams, S. H., Bunch, ., Valdez, A., and Stevens, S. (2009), The rate of granule ripple movement on Earth and Mars, *Icarus, 203*, 71–76, doi:10.1016/j.icarus.2009.03.033.

Zobeck, T. M., et al. (2003), Aggregate-mean diameter and wind-erodible soil predictions using dry aggregate size distributions, *Soil Sci. Soc. Am. J., 67*, 425–436, doi:10.2136/sssaj2003.0425.

Appendix

Table 2.A. Survey of Soil Types from MI images

MI sol	target	feature	soil class	image
13	FirstSoil1Final		bright dust	2M127523611EFF0309P2930M2M1
15	FirstSoil1Final		bright dust	2M127691325EFF0309P2930M2M1
41	Crest	Arena	beform armor	2M130001239EFF0506P2943M2M1
43	Mimi_Tracks2	Mimi Tracks	beform armor	2M130169446EFF0514P2943M2M1
44	Soil1	Ramp Flats	lithic fragments	2M130267512EFF0700P2938M2M1
45	Halo_01	Angel Flats	beform armor	2M130356321EFF0800P2943M2M1
46	Trout 1	Grande Flats	lithic fragments	2M130463631EFF0900P2943M2M1
51	Soil2	Split Rock Flats	bright dust	2M130884921EFF1000P2953M2M1
52	SugarT_1	Sugar	bedform armor	2M130974259EFF1100P2953M2M1
54	Ridge1	Wrinkle	lithic fragments	2M131150911EFF1124P2953M2M1
63	Nail4	Plank	bright dust	2M131952603EFF1300P2957M2M1
65	Soil1	SugarLoafFlats	bright dust	2M132132632EFF1500P2958M2M1
68	Gobi1	deserts	lithic fragments	2M132401584EFF1800P2977M2M1
70	Gobi1	deserts	lithic fragments	2M132591324EFF1800P2977M2M1
73	Polar	Bear Paw	bedform armor	2M132842726EFF2000P2977M2M1
74	Polar	Bear Paw	bedform armor	2M132934919EFF2000P2977M2M1
75	Soil2	Patio	lithic fragments	2M133017098EFF2100P2977M2M1
105	Flats1	Bitterroot flats	lithic fragments	2M135687606EFF3000P2956M2M1
110	Soil1	Waffle Flats	lithic fragments	2M136126464EFF3400P2957M2M1
113	Mayfly	Big Hole	lithic fragments	2M136401334EFF3700P2957M2M1
141	Hells Kitchen	The Boroughs	bright dust	2M138892337EFF54CAP2956M2M1
164	Goldfin1	EndOfTheRainbow	dark soil	2M140930743EFF6904P2956M2M1
166	Goldstaub	FortKnox	dark soil	2M141110706EFF6962P2976M2M1
167	Jaws	Goldfinger	dark soil	2M141188638EFF6980P2976M2M1
240	GreenEyes	Tikal_Area	bright dust	2M147676880EFF8800P2976M2M1
258	GreenEyes	Tikal_Area	bright dust	2M149274786EFF8800P2976M2M1
259	Disturbance	Conjunction Junction	bright dust	2M149359510EFF8800P2960M2M1
279	Coffee	TakeAbreak	lithic fragments	2M151139145EFF8982P2979M2M1
281	Coffee	TakeAbreak	lithic fragments	2M151316310EFF8982P2959M2M1
341	Ds1	Penny	dark soil	2M156637810EFFA201P2957M2M1
372	3x1_TGT_2	Peace	bright dust	2M159394037EFFA2HPP2957M2M1
373	Equality	Peace	dark soil	2M159478927EFFA2HPP2957M2M1
428	Paso_Dark1	Paso Robles2	disturbed soil	2M164353852EFFA8B3P2997M2M1
431	Castoro	Paso Robles2	mixed soil	2M164621314EFFA8B3P2997M2M1
457	Sierra	Crumble	mixed soil	2M166938419EFFA9F4P2997M2M1
460	Almond	Crumble	mixed soil	2M167202206EFFA9F4P2977M2M1
477	Hoof	Jibsheet	mixed soil	2M168708459EFFAAACP2977M2M1

Table 2.A. (continued)

MI sol	target	feature	soil class	image
480	Bell	Jibsheet	mixed soil	2M168974673EFFAAACP2956M2M1
494	Hitting	Larry's Lookout	dark soil	2M170218789EFFAAEEP2976M2M1
499	Doubloon	Pequod	mixed soil	2M170661261EFFAAFQP2906M2M1
588	Hermann_Buhl	Lambert	bright dust	2M178562232EFFAE03P2977M2M1
607	Tubular	Cliffhanger	bedform armor	2M180252684EFFAEM9P2977M2M1
611	LandsEnd	Cliffhanger	bedform armor	2M180617778EFFAEM9P2956M2M1
612	HangTwo	Cliffhanger	bedform armor	2M180692664EFFAEM9P2936M2M1
707	Gallant Knight	ElDorado Scuff	dark soil	2M189124338EFFAL00P2957M2M1
709	Shadow	ElDorado Scuff	dark soil	2M189317905EFFAL00P2956M2M1
710	Edgar	ElDorado Scuff	dark soil	2M189393476EFFAL00P2956M2M1
812	Mawson		mixed soil	2M198449742EFFAR00P2936M2M1
822		Enderbyland	mixed soil	2M199339208EFFAR00P2956M2M1
842	EngTarget	Enderbyland	dark soil	2M201113145EFFAR00P2956M2M1
861	Brunt	Enderbyland	dark soil	2M202800241EFFAS00P2956M2M1
870	Progress3	Enderbyland	dark soil	2M203598957EFFAS00P2977M2M1
880	Brunt	Enderbyland	mixed soil	2M204486480EFFAS00P2956M2M1
908	Palmer	Palmer	dark soil	2M206972038EFFAS00P2939M2M1
913	Palmer2	Palmer2	dark soil	2M207415905EFFAS00P2959M2M1
930	Halley_Brunt	Enderbyland	mixed soil	2M208923479EFFAS00P2936M2M1
937	Palmer	Enderbyland	dark soil	2M209544890EFFAS00P2956M2M1
1007	Clast_1	Clasts	dark soil	2M215761379EFFAS00P2957M2M1
1008	Clast_3b	Clasts	mixed soil	2M215849921EFFAS00P2957M2M1
1008	Palmer	Enderbyland	dark soil	2M215850180EFFAS00P2957M2M1
1034	Clarence		dark soil	2M218159237EFFAS20P2956M2M1
1085	Londonderry	Troll	dark soil	2M222688344EFFASCGP2976M2M1
1198	Lefty Ganote	Gertrude Weise	mixed soil	2M232720233EFFATB4P2976M2M1
1230	Soil Observation		dark soil	2M232720233EFFATB4P2976M2M1
1239	Eileen_Dean	Eileen Dean	mixed soil	2M236359578EFFAUATP2976M2M1
1244	Eileen_Dean	Eileen Dean	mixed soil	2M236802483EFFAUATP2956M2M1
1246	Eileen_Dean2	Eileen Dean	mixed soil	2M236979348EFFAUATP2906M2M1
1251	Innocent_Bystander	Innocent Bystander	dark soil	2M237423384EFFAUCMP2976M2M1
1252	Innocent_Bystander	Innocent Bystander	dark soil	2M237511759EFFAUCMP2979M2M1
1277	StealingThird	Innocent Bystander	dark soil	2M239727497EFFAUCMP2979M2M1
1291	StealingThird	Innocent Bystander	mixed soil	2M240975685EFFAUCMP2956M2M1

Chapter 3

Soil Mineralogy at the Mars Exploration Rover landing sites: An Assessment of the Competing Roles of Physical Sorting and Chemical Weathering

A version of this chapter was originally published in Journal of Geophysical Research 117 (2012): E01006, doi:10.1029/2011JE003861.

Abstract

Soils in Gusev Crater and Meridiani Planum derive primarily from a surface dominated by basalt. The modal mineralogy of primary (igneous) and secondary (alteration) phases in the soils is estimated using Mössbauer, MiniTES, and APXS spectra. Primary minerals include plagioclase, pyroxene, and olivine with less common apatite, magnetite, and chromite. Secondary phases are dominated by sulfates, and include nanophase oxides, chlorides, hematite, and are assumed to include amorphous silica and phyllosilicates. Most soil chemical compositions overlap with basalts indicating that despite the presence of a secondary component in the soils, they have not been significantly chemically weathered. We modeled the significance of olivine dissolution by acid-S by iteratively removing the molar FeO_T + MgO component (olivine proxy) from the mean bulk compositions of the Gusev rock classes Adirondack, Algonquin, and Irvine until none remained. Regardless of modeling conditions, acid-S alteration cannot account for many soils in Gusev Crater that are either depleted or enriched in molar FeO_T + MgO, although it is a process capable of explaining some soil compositions. Results from a rock and mineral mixing model, supports our hypothesis for soil formation that consists of surface comminution by impact gardening, followed by compositional modification by hydrodynamic sorting and admixing of secondary components, including phyllosilicates and sulfates. Such a physical process can produce the range of molar FeO_T + MgO in soils by concentrating or depleting specific minerals. For example, dust and fine sands are enriched in molar FeO_T + MgO relative to coarse sand, which suggests accumulation of more mafic phases in finer grain fractions.

1. Introduction

Considerable interest has focused on the genesis of soils on Mars due to the potential for detecting chemical alteration, especially the potential for alteration involving water. Soils have the potential to record major environmental changes, such as the transition from an early humid and warm surface with a CO_2-rich atmosphere, to a late arid and cold surface with a low-CO_2 atmosphere [Squyres and Kasting, 1994; Carr and Head, 2010] by preserving the extent of chemical weathering. Derived primarily from basalt source material [Yen et al., 2005; McSween et al., 2009, 2010], soil compositions may differ from unaltered basalts with the addition of phyllosilicate mineral phases [e.g., Hamilton et al., 2005; Clark et al., 2007; Bishop et al., 2008; Ehlmann et al., 2009; McKeown et al., 2009], evaporates [Yen et al., 2005], and volcaniclastic material [Bibring et al., 2006]. Consequently, soils represent the bulk surface composition of the Martian crust [e.g., McSween et al., 2010].

Significant attention has been focused on the types of chemical alteration and conditions conducive to weathering. The prevailing model of soil formation on Mars involves a chemical weathering process of olivine dissolution [Tosca et al., 2004; Hurowitz and McLennan, 2007; Bandfield et al., 2011] under acidic, high-sulfur conditions. Another model involves in situ aqueous alteration with shallow soil profiles [Amundson et al., 2008]. However, little focus has been directed at considering compositional fractionation by physical processes such as hydrodynamic sorting [McLennan, 2000; McSween and Keil, 2000]. A thorough understanding of soil compositions is necessary to determine the extent to which basaltic bedrock is affected by

chemical weathering. In addition, compositional variations must incorporate detailed textural results [McGlynn et al., 2011] as a basis to evaluate physical fractionation processes [e.g., Nesbitt and Young, 1996; Young and Nesbitt, 1998].

The primary and alteration mineral compositions of Martian soils are not well understood despite extensive investigations from the Mars Exploration Rovers (MER) Spirit and Opportunity [e.g., Yen et al., 2005; Morris et al., 2006a, 2006b, 2008; Rogers and Aharonson, 2008]. The surface of Mars has been described as mostly basaltic [McSween et al., 2009], with rocks in Gusev Crater consisting mostly of variably altered basaltic lavas [McSween et al., 2008]. As demonstrated here and discussed by Yen et al. [2005], igneous minerals dominate the soils at both Mars Exploration Rovers sites. However, the effects of chemical weathering in soils seem to be reflected in their (1) sulfur enrichment, (2) chemical depletion in FeO_T + MgO interpreted as olivine dissolution from acid-sulfur alteration [Hurowitz and McLennan, 2007], (3) high abundance of SiO_2 [Yen et al., 2008] and opaline silica from hydrothermal alteration [Squyres et al., 2008; Schmidt et al., 2008], and (4) occurrence of salts [Yen et al., 2005] that may indicate a past hydrous environment. Notably absent from Martian soils are products of extensive chemical weathering from hydrolysis [Hurowitz and McLennan, 2007]. In addition to basaltic and alteration components, soils are mixed with detrital components, including a volcaniclastic additive of enriched S and Cl [Bibring et al., 2006; Morris et al., 2006a], a Ni-enriched meteorite fraction [Yen et al., 2006], and a poorly characterized, ubiquitous [Tomasko et al., 1999; Bell et al., 2000] magnetic [Madsen et al., 2009] dust component comprised of carbonate [Bandfield et al., 2003], sulfate, pyroxene, olivine, and framework silicates, including feldspar or zeolite [Hamilton et al., 2005].

Resolving the mineralogy of soils in Gusev Crater and Meridiani Planum is essential to evaluate the extent of chemical weathering. Estimating the proportion of components with high chemical weathering potential, such as olivine and glass, and inferring the abundance of secondary alteration components (phyllosilicate minerals), places constraints on the minimum and maximum range of chemical alteration. Compositional variations in soils may also result from accessory mineral sorting [McSween and Keil, 2000] through physical processes such as impact gardening [Knauth et al., 2005; Barlow, 2010], aeolian transport [Greeley et al., 2004, 2006, 2008; Sullivan et al., 2005, 2008; Parteli et al., 2009], and possibly fluvial [e.g., Burr, 2010] transport. Examining the chemistry and mineralogy of MER soil compositions, when combined with textural characteristics [McGlynn et al., 2011] can resolve the role of accessory mineral sorting on soil composition.

This paper has a three-part purpose. First, we present comprehensive mineralogy estimates for soils at both MER landing sites by combining Alpha Particle X-Ray Spectrometer (APXS) [Rieder et al., 2003], Mössbauer spectrometer (MB) [Klingelhöfer et al., 2003], and Miniature Thermal Emission Spectrometer (MiniTES) [Christensen et al., 2003] data, using a normative mineralogy estimate for igneous rocks [McSween et al., 2008] that has been modified for soils [McSween et al., 2010]. Second, with the establishment of a mineralogy baseline, we evaluate the effects of chemical alteration based on comparisons of APXS soil and bedrock chemistry, which forms a guide to evaluate potential soil protoliths in Gusev Crater. Third, the potential of physical processes capable of compositional modification by mineral fractionation is also considered, particularly in the context of diverse textural relationships in Martian soils [McGlynn

et al., 2011]. By integrating physical attributes with compositional data, we develop new model to explain soil composition, largely driven by physical processes, which stands in contrast to existing aqueous alteration models [Hurowitz and McLennan, 2007; Amundson et al., 2008] for soil formation.

2. Methods

2.1. Sample Selection and Composition Inputs

Soil samples were selected based upon the availability of chemical (APXS), mineralogical (MB, MiniTES), and textural (MI) data for the Gusev Crater and Meridiani Planum landing sites. APXS chemistry [Rieder et al., 2003] for Gusev Crater was compiled from published results [Gellert et al., 2006; Ming et al., 2008] through sol 1360 and corresponding MB spectra through sol 1411 [Morris et al., 2006a]. Soil mineralogy in Meridiani Planum was calculated from APXS results through sol 928 [Yen et al., 2006] and MB through sol 557 [Morris et al., 2006b]. MiniTES estimates of a high-silica phase, interpreted as secondary amorphous silica or glass, and phyllosilicates, modeled as a 1:1 ratio of montmorillonite and beidellite for Meridiani soils [Rogers and Aharonson, 2008] and Gusev soils [McSween et al., 2010] are incorporated to quantify alteration phases in soils. The inclusion of a phyllosilicate component improves least squares modeling of MiniTES spectra that have been detected in some soil targets, but should not be interpreted as direct evidence for the presence of montmorillonite and beidellite in MER soils.

Major sedimentary trends in physical weathering and inferred chemical alteration are evaluated from a microscopic investigation of soil textures [McGlynn et al., 2011] using the high-resolution Microscopic Imager on the Spirit rover [Herkenhoff et al., 2003]. The addition of

grain-size data provides the basis to evaluate principles of physical and chemical soil weathering [e.g., Nesbitt and Young, 1996; Young and Nesbitt, 1998] at a level not before possible on Mars. The use of mean grain sizes may not fully characterize the textural variation within poorly and very poorly sorted soils, but can distinguish between broad groupings [e.g., Yen et al., 2005] of dust (bright dust), sand (dark soil, bed form armor), and pebbles (bed form armor, lithic fragments, and bimodal mixed soils).

2.2. Mineralogy Calculations

MB spectra for Fe-bearing minerals provide one basis for soil modal mineralogy estimates. The wt. % (weight percents) of Fe-bearing minerals (olivine, pyroxene, ilmenite, magnetite, hematite, and nanophase ferric oxides) were calculated from the proportions of MB subspectral areas for soils in Gusev Crater [Morris et al. 2006a, 2008] and Meridiani Planum [Morris et al., 2006b] by modeling the concentrations of Fe in each phase [McSween et al., 2010]. To account for Fe-free minerals (plagioclase, apatite, chromite), normative calculations were based on APXS chemistry [Gellert et al., 2006; Ming et al., 2008]. The distribution of iron phases (FeO and Fe_2O_3) for each sample was calculated from reported MB Fe^{3+}/Fe_T ratios for Gusev [Morris et al., 2006a, 2008] and Meridiani soils [Morris et al., 2006b].

Normative mineralogy calculations are typically applied to Martian igneous rocks [McSween et al., 2008] but not soils, due to the possible presence of secondary alteration components. To account for alteration components, a series of assumptions, based on the reported detections of secondary minerals, and the known limitations of such data sets, are applied. Two approaches have been developed to remove quantities of S and Cl [McSween et al., 2010]. Model 1 removes

all S as $(Mg,Ca)SO_4$ and Cl as (Na,K)Cl in a 1:1 ratio from APXS bulk soil chemistry. Concentrations of S and Cl are assumed to be added as salts [King and McLennan, 2010], with S detected as sulfate by MiniTES [Rogers and Aharonson, 2008], and Cl is assumed as chloride. In this model, nanophase ferric oxides are assumed to be hematite. Model 2 assumes S and Cl were added from volcanic outgassing [Bibring et al., 2006] and removes all S as SO_3 and Cl from APXS bulk soil chemistry, without associated cations. Nanophase ferric oxides are treated as a 2:1 ratio of schwertmannite $Fe_8O_8(OH)_6SO4 \cdot nH_2O$ [Tosca et al., 2008] and akaganeite $FeO(OH)_{1-x}Cl_x$ [Bell et al., 2000]. In both models, phyllosilicates and silica, detected from MiniTES spectra are also removed from bulk APXS chemistry.

In both models, phyllosilicates are subtracted as a 1:1 ratio of montmorillonite ($Na_{0.2}Ca_{0.1}Al_2Si_4O_{10}(OH)_2 \cdot 10H_2O$) and beidellite ($Na_{0.3}Fe^{3+}{}_2Si_3AlO_{10}(OH)_2 \cdot 4H_2O$) of 4 wt. % in Gusev Crater [McSween et al., 2010], and 5 wt. % in Meridiani Planum [Rogers and Aharonson, 2008]. While smectite clays have been detected on Mars from orbit in locations including Mawrth Vallis [Bishop et al., 2008; McKeown et al., 2009] and Nili Fossae [Ehlmann et al., 2009], their quantities have not been constrained, and are only assumed. Additional Fe-Mg clays may be suitable alteration products, but have not been detected. Silica as opal [Schmidt et al., 2008] or silica glass in soils is subtracted at 8 wt. % in Gusev Crater [McSween et al., 2010] and 10 wt. % in Meridiani Planum [Rogers and Aharonson, 2008]. The quantity and composition of clay minerals, thought to represent chemical alteration, only represent estimates using the best available data from a limited survey of soil targets [Rogers and Aharonson, 2008; McSween et al., 2010] to constrain the potential for silica and phyllosilicate minerals inferred to be present in

all soils. MiniTES spectra, needed for the detection of phyllosilicates and silica, are not available for all soil samples. To overcome these limitations, soils are assumed to contain a constant phyllosilicate and silica composition, as outlined with assumptions and constraints by McSween et al. [2010], and the results are assumed to be homogeneous for all soils in the respective MER landing sites. Estimates using this approach should not be interpreted as evidence of the direct detection of silica and phyllosilicates. Additionally, the detection of smectite phyllosilicates in MER soils [Rogers and Aharonson, 2008; McSween et al., 2010] has not been independently supported or verified. The assumed presence of phyllosilicates is only used to constrain the resulting mineralogy, establish the potential for chemical alteration, and provide a rationale to evaluate chemical alteration by weathering. A sensitivity test of potential clay content is demonstrated in section 4.4.2 using a chemical mixing model from APXS data. We prefer mineral estimates from model 1 due to the retention of excess cations not otherwise accounted for with the removal of S and Cl in model 2. Such values are misleading [e.g., Fedo et al., 1995] and yield results for higher concentrations of CaO, Na_2O, Al_2O_3, SiO_2, and therefore higher estimates of pyroxene than are likely.

Soil chemistry is renormalized to 100% after the subtraction of phyllosilicates, silica, and S and Cl as sulfate and chloride, or as SO_3 and Cl. Basaltic igneous mineralogy estimates were then calculated using a CIPW normative procedure. Finally, Fe-free minerals (plagioclase, apatite, chromite) from the normative calculations were combined with Fe-bearing minerals, and the resulting mineral proportions were renormalized to 100 wt. %. McSween et al. [2010] described the model in detail, and provided a worked calculation.

3. Results

3.1. Soil Mineralogy Estimates

Calculated modal mineralogy estimates for soils analyzed at the MER landing sites are given in Table 3.1. The two models used to calculate mineralogy may bracket the range of possible soil compositions [McSween et al., 2010]. A detailed breakdown for model 1 (Table 3.A-1 in Appendix) and model 2 (Table 3.A-2 in Appendix) results is also provided in the auxiliary material. Results for primary minerals including olivine, plagioclase, magnetite, chromite, and apatite are broadly similar in both models. Pyroxene results in model 2 are ~ 11 wt. % greater than model 1 due to the removal of MgO + CaO associated with sulfur, $Na_2O + K_2O$ with chlorine, and the subsequent increase in renormalized MgO, FeO, and Fe_2O_3 abundances. The inclusion of sulfates and chlorides in model 1, which are not present in model 2, increases the secondary mineral total, or total alteration, in model 1 by ~6 wt. %. The standard deviations for all results are greater using model 2. Limitations in the normative procedure cannot calculate mineral estimates for certain soils with high TiO_2 and FeO phases, the results for such soils are left blank (Tables 3.A-1 and 3.A-2).

Mineral proportions between the two landing sites are similar for both models. Soils in Gusev Crater are slightly enriched in olivine and plagioclase, and depleted in pyroxene relative to Meridiani soils (Table 3.1). Mineral proportions for individual soil samples show higher variability in mineral proportions within each landing site (Figures 3.1A–1D). Olivine in Gusev soils ranged from 16.9 to 9.0 ± 1.7 wt. % (Figure 3.1A, model 1) and 16.6 to 2.9 ± 2.5 wt. %

(Figure 3.1B, model 2), and in Meridiani Planum ranged from 16.8 to 11.8 ± 1.4 wt. % (Figure 3.1C, model 1) and 13.3 to 8.8 ± 1.3 wt. % (Figure 3.1D, model 2).

3.2. Grain Size Relationships with Chemical and Mineral Compositions

Concentrations of SO_3 soils are generally related to measured soil mean grain sizes (Figure 3.2A), which are represented as the standard logarithmic unit phi (ϕ), where S is the major axis length [Folk, 1981]:

$$\phi = -\log_2 S\,(\text{mm}) \tag{1}$$

Soils with coarse grains (0 to −3 ϕ, very coarse sand to fine pebbles) have larger SO_3 concentrations, while the lowest SO_3 concentrations are in fine-grained soils (0 to 3 ϕ, very fine to coarse sand). When grouped by soil type [McGlynn et al., 2011], lithic fragment soils, with the largest measured mean grain sizes are elevated in SO_3 relative to other soil types. Dark soils, with the smallest mean grain sizes are depleted in SO_3. Bed form armor soils and bimodal mixed soils contain intermediate concentrations of SO_3 and have grain sizes that fall between fine dark soils and coarse lithic fragment soils.

A general co-enrichment of SO_3 and Cl [e.g., Gellert et al., 2006; Morris et al., 2006a] has been observed in MER soils. The pattern of Cl concentrations with grain size (Figure 3.2B) is therefore similar to that of SO_3, where the coarser fraction (0 to −3 ϕ, very coarse sand to fine pebbles) has higher concentrations of Cl relative to soil with the finer fraction (0 to 3 ϕ, very fine to coarse sand). Although dark soils and lithic fragment soils are compositionally distinct from each other, clear compositional trends between grain size in bed form armor and bimodal mixed soils are not apparent. The general pattern of SO_3 and Cl with increasing grain size may not

represent igneous compositions. Instead, the correlation may [e.g., Gellert et al., 2006; Morris et al., 2006a] reflect additive components from volcanic outgassing of volatiles [Yen et al., 2006] during an intense period of early activity [Bibring et al., 2006], precipitate cements formed by fluid interaction [Hurowitz and McLennan, 2007], or surface coatings that are proportionally higher in small grains due to increased surface area. A further evaluation of the nature of SO and Cl concentrations as an additive dust component is presented in section 3.3.

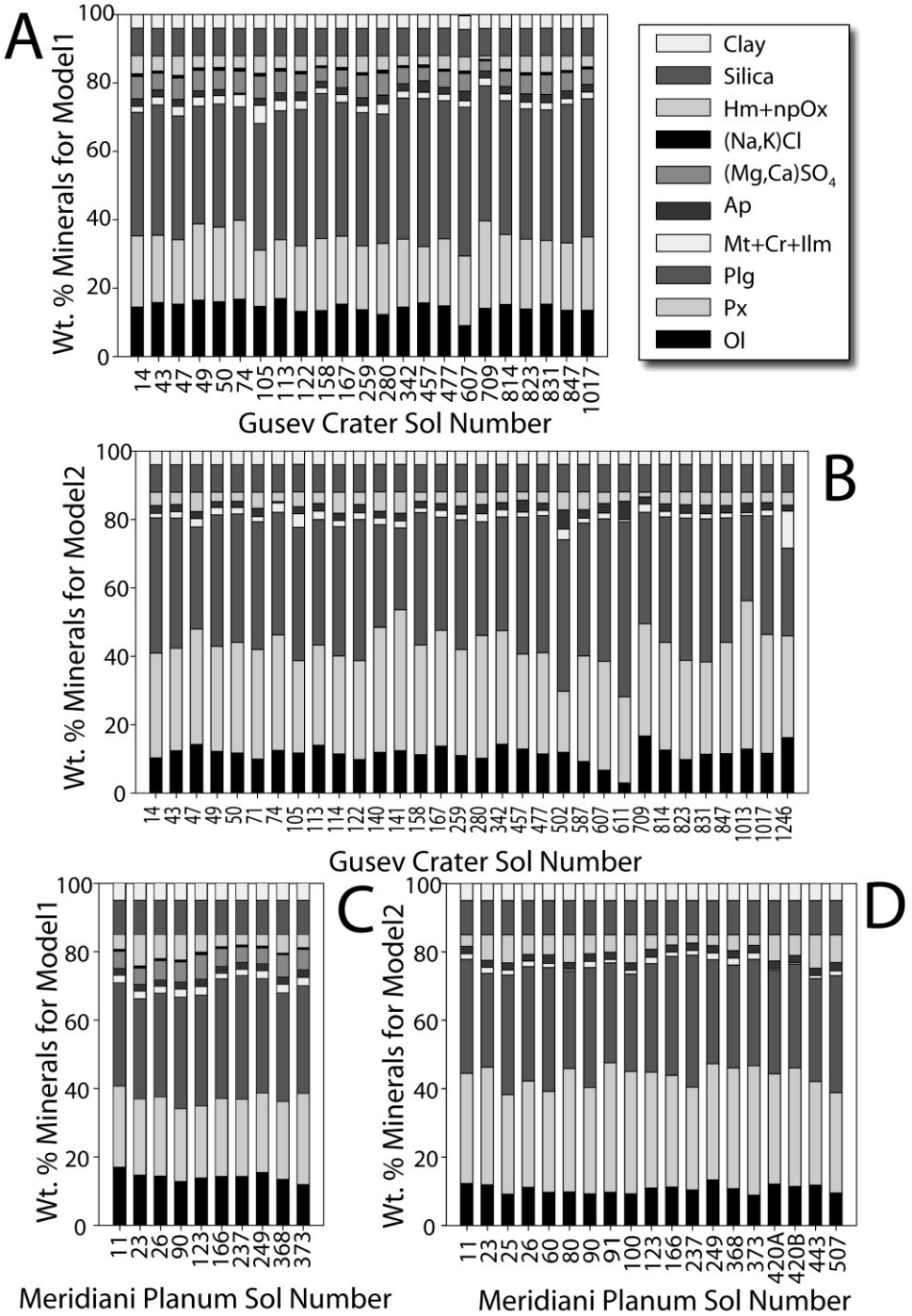

Figure 3.1. Mineralogy estimates for soils in Gusev Crater, with corresponding APXS Sol analysis dates, based on (A) model 1 and (B) model 2, and estimates for soils in Meridiani Planum based on (C) model 1, and (D) model 2. Mineral abbreviations are Ol, olivine; Px, pyroxene; Plg, plagioclase; Mt, magnetite; Cr, chromite; Ap, apatite; Hm, hematite; npOx, nanophase ferric oxide; and Ilm, ilmenite. Clays are modeled as a 1:1 ratio of idealized montmorilonite and beidellite. Model 2 npOx is modeled as a 2:1 ratio of schwertmannite and akaganeite. Mineralogy is calculated from models by McSween et al. [2010].

Table 3.1. Mean soil mineralogy for Gusev Crater and Meridiani Planum

	MODEL 1				MODEL 2			
Mineral	Gusev Crater	SD	Meridiani Planum	SD	Gusev Crater	SD	Meridiani Planum	SD
Primary minerals (wt. %)								
Olivine	14.5	1.7	14.0	1.4	11.6	2.5	10.6	1.3
fo	49.2	3.7	40.4	4.5	57.7	8.3	59.7	17.4
Pyroxene	20.1	2.1	23.0	1.5	31.4	4.5	33.1	2.8
en	51.6	3.7	42.8	4.5	60.0	8.1	61.7	16.9
Plagioclase	38.8	2.6	32.3	2.2	36.6	5.7	32.0	3.0
an	38.9	4.4	48.7	3.6	36.9	4.2	40.6	6.1
Magnetite	1.6	0.8	1.6	1.5	1.6	1.5	0.8	0.4
Chromite	0.5	0.1	0.6	0.1	0.5	0.1	0.6	0.1
Apatite	2.1	0.5	2.0	0.1	2.4	0.9	2.1	0.1
Secondary minerals (wt. %)								
npOxide	3.5	1.0	3.8	1.0	3.4	1.1	3.1	1.7
Hematite	0.5	0.3	1.5	1.6	0.5	0.4	2.7	2.6
Sulfates	5.4	1.0	5.5	0.9				
Chlorides	0.7	0.1	0.6	0.1				
Silica	8		10		8		10	
Phyllosilicates	4		5		4		5	
Total alteration	22.1	2.0	26.4	2.4	15.8	1.1	20.8	2.2

Mineral abbreviations are fo, forsterite; en, enstatite; an, anorthite.

Concentrations of TiO_2 do not vary with grain size (Figure 3.2C). Most sand and pebbles have a similar range 0.4 to 1.2 wt. % TiO_2, although dark soils (medium sand) contain the lowest concentrations of TiO_2 (<0.8 wt. %) among measured soils in Gusev Crater. Bed form armor soils have a greater concentration in TiO_2 when compared to dark soils, lithic fragments, and most bimodal mixed soils. However, these apparent variations in TiO_2 are not statistically significant.

We evaluated normative soil mineral proportions to assess compositional and textural links that may result from chemical weathering or physical abrasion during hydrodynamic sorting (Figure 3.3). Olivine and plagioclase represent primary igneous minerals with high weathering susceptibility [Hausrath et al., 2008], and can be used to provide clues about soil alteration. The variation of modal olivine concentrations in soils is small, the abundance of which is invariant with grain size. Bed form armor soils possess the lowest proportion of olivine (Figures 3.3A and 3B) when compared to other soil types, although the sample size is too small to assess potential trends in compositional alteration. Potential physical mechanisms of compositional modification

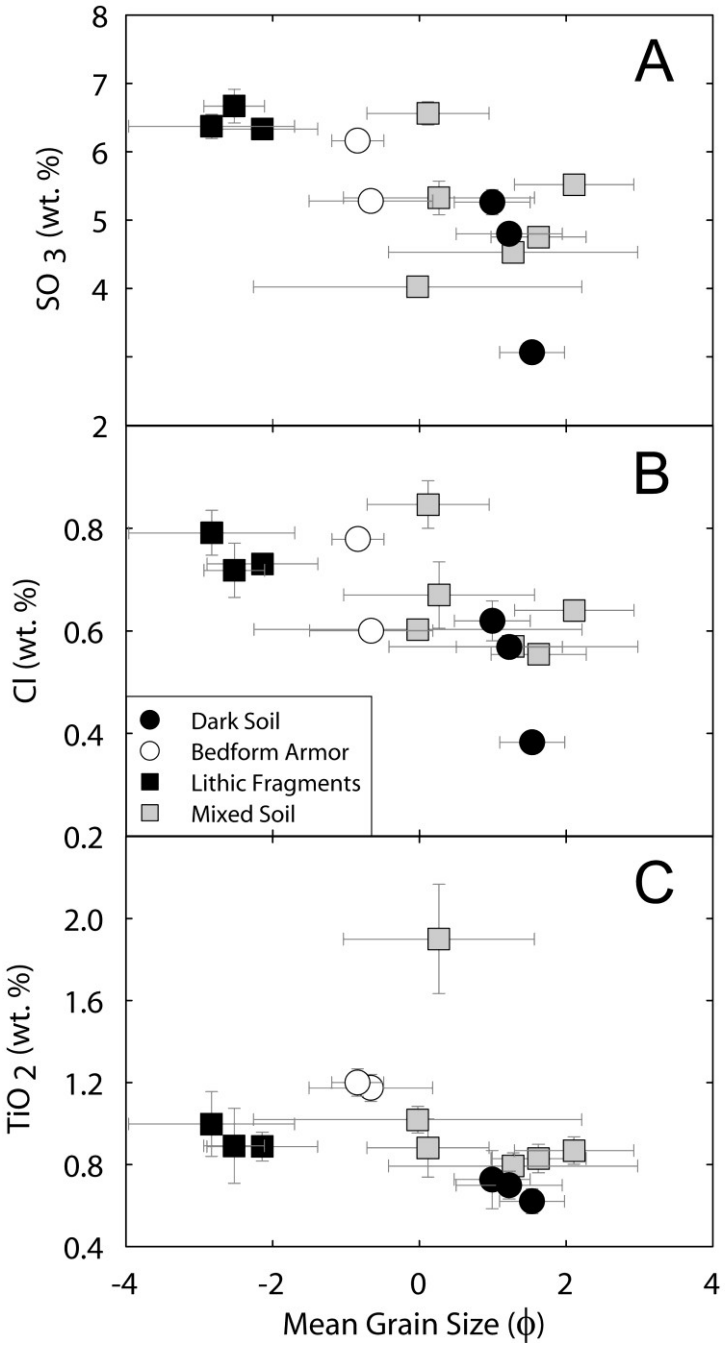

Figure 3.2. Chemical oxide compositions of Gusev soils compared to mean grain size for (A) SO_3 that increases with mean grain size, (B) an increase in Cl with increasing grain size, and (C) TiO_2 concentrations that are invariant with grain size. Vertical error bars are smaller than many data points, horizontal error bars represent the standard deviation of measured grain sizes from McGlynn et al. [2011].

are discussed in section 4.4. Variations in secondary alteration minerals (Figures 3.3E and 3.3F) including nanophase ferric oxides, hematite, sulfates, chlorides, silica, and clays are collectively referred to as "total alteration." Gusev soils are comprised of 17 to 25 wt. % alteration components based on model1 (Figure 3.3E) and comprised of 13 to 25 wt. % alteration components based on model 2 (Figure 3.3F). The proportions of alteration components are independent of grain size or soil type.

3.3. Dust Fraction Relationships with Chemical Compositions

Previously, the presence of dust on surface targets could only be generally inferred between high- and low-dust targets, without quantification of dust accumulation. To better understand the behavior of dust, sedimentary material that is too small (< 100 μm) to be resolved in MI images can be estimated as the ratio of unmeasureable counts to the total number of measured grains from point counting grids by McGlynn et al. [2011]. This approximation as a two-dimensional proxy for dust on the surface of soils is only used as an indication of the presence of fines, similar to the broad soil classifications of Karunatillake et al. [2010]. A test of this graphical approach is first evaluated against chemical concentrations of SO_3 and Cl, which are expected to be major components in dust [Yen et al., 2006]. Our graphical estimates of dust (Figures 3.4A and 3.4B) are consistent with a general compositional increase of SO_3 and Cl with increasing presence of dust, and support the viability of this method to estimate dust and a compositional component mixed in soils.

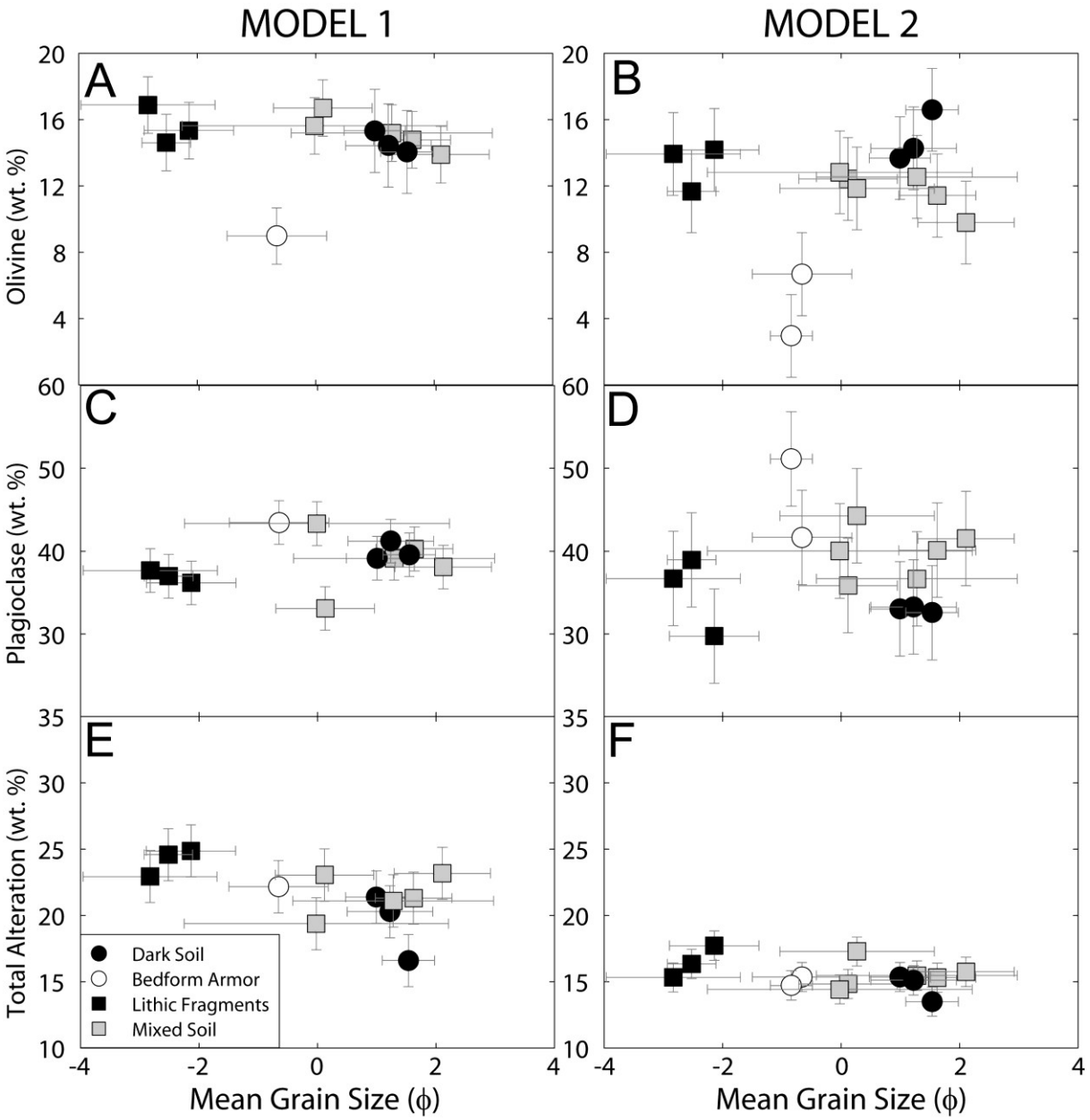

Figure 3.3. Primary and alteration mineralogy for Gusev soils plotted against soil mean grain size for two models ((left) model 1; (right) model 2) of (A, B) olivine depleted in bed form armor (medium to coarse sand) from possible fractionation when compared to fine to dark soil (medium sand), (C, D) plagioclase feldspar enrichment in bed form armor compared to dark soil, and (e, f) total alteration with assumed silica and phyllosiliate content in soils, estimated from both mineralogical models. Vertical error bars represent the standard deviation of soil mineralogy (Table 3.1).

Given the viability of the dust estimates depicted in Figures 3.4A and 3.4B, trends in chemical and mineral compositions with dust can be evaluated. The penetration depth of APXS spectra [Rieder et al., 2003] is similar to the micron-depth thickness of dust deposits on rocks and soils [Yen et al., 2005]. Although such deposits are often superficial coatings, dust can have compositional importance in APXS results. Samples with complete dust cover (bright dust) are not depleted or enriched in TiO_2 relative to other soils (Figure 3.4C) indicating that Ti-bearing minerals are not concentrated in dust. Proportions of major primary (olivine, Figures 3.5A and 3.5B; plagioclase, Figures 3.5C and 3.5F) and secondary (total alteration, Figures 3.5E and 3.5F) minerals do not vary systematically with dust cover. A general approximation between nanophase oxides and dust is observed (Figures 3.5G and 3.5H) with high dust samples (bright dust, lithic fragments) enriched by ~2 wt. % npOx over low dust (dark soil) samples. Although the mineralogy of nanophase ferric oxides has not been resolved, these findings are generally consistent with the observation that ferromagnetic phases are concentrated in dust at Gusev Crater [Bertelsen et al., 2004; Morris et al., 2006a] and also at the Phoenix landing site [Drube et al., 2010].

4. Processes Affecting Soil Compositions

Modal mineralogy estimates of olivine (from MB spectra) and the possibility of alteration components (phyllosilicates inferred from MiniTES spectra) place constraints on the extent of chemical weathering of soils at the MER landing sites. The potential for compositional alteration is assessed using chemical mixing models from APXS chemistry.

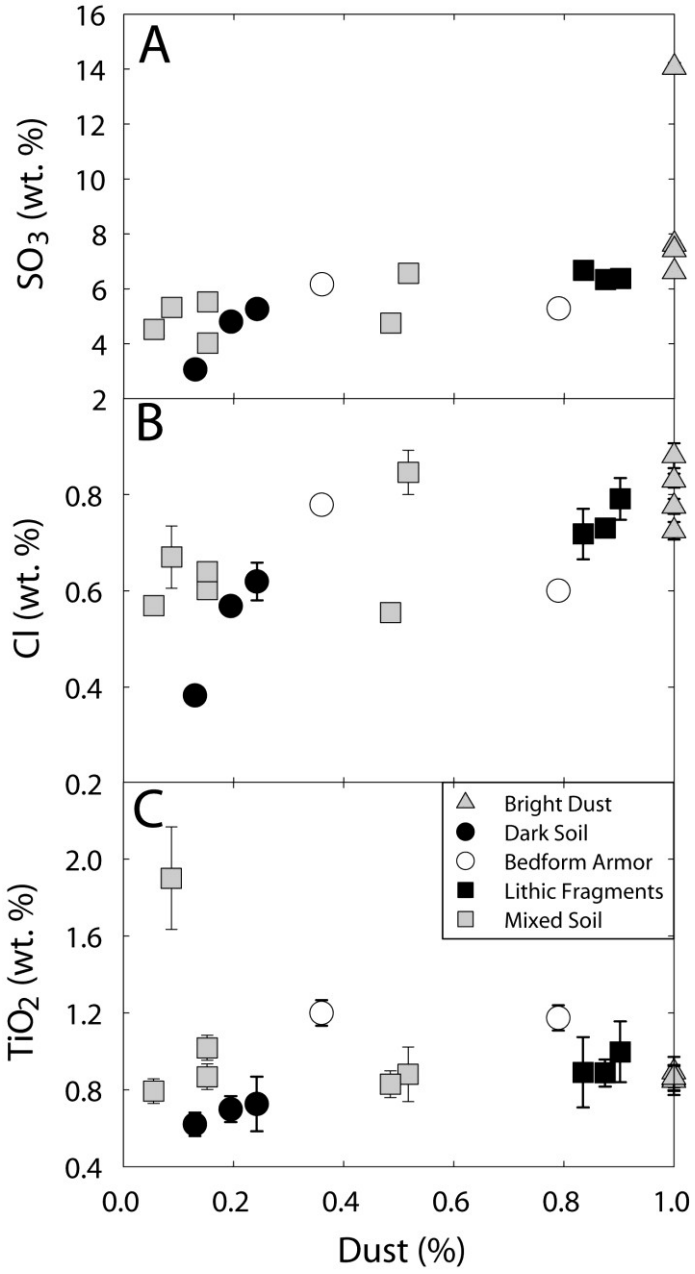

Figure 3.4. Gusev soils blanketed with fines (<100 μm) surface dust (bright dust) or with high dust cover (lithic fragments) are generally enriched in (A) sulfur (SO_3) and (B) chlorine (Cl) when compared to relatively dust free surfaces, confirming a SO_3 + Cl dust component. (C) Concentrations of TiO_2 are homogeneous, and are independent of dust fraction.

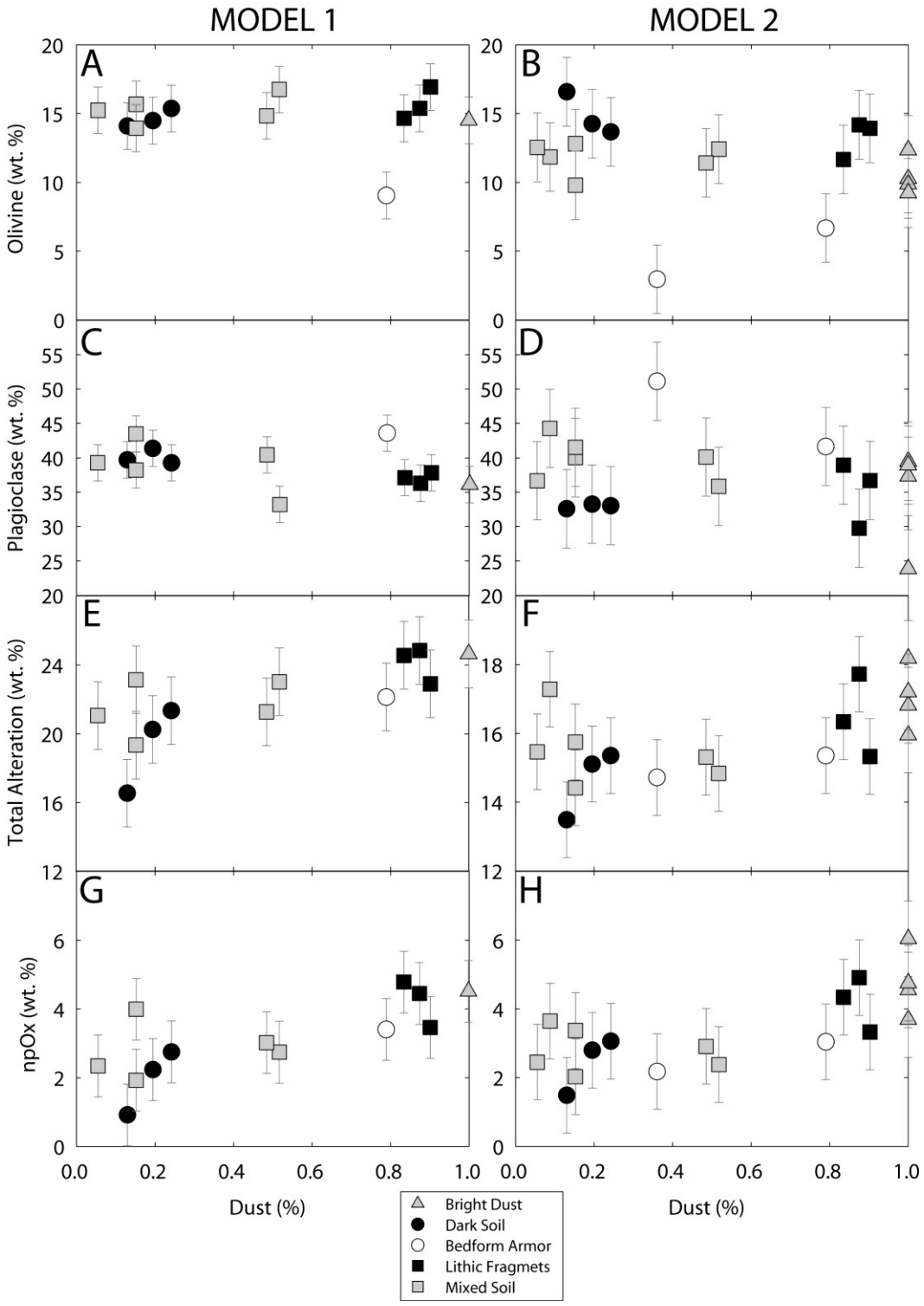

Figure 3.5. Primary minerals (A, B) olivine, (C, D) plagioclase, and (E, F) total alteration are not apparently controlled by dust cover for soils in Gusev Crater. (G, H) Concentrations of nanophase ferric oxides are elevated in high-dust soils.

4.1. Bedrock Composition

Before isolating possible mechanisms that effect soil compositions at the MER landing sites, it is critical to identify the compositional variation in the provenance bedrock from which the soils are derived. Volcanic rocks within Gusev Crater are compositionally heterogeneous, spanning a range of rocks types, including basalt, trachybasalt, tephrite, and picrobasalt in total alkali-silica (TAS) diagrams [McSween et al., 2006, 2008, 2009]. Figure 3.6A illustrates Gusev rocks (with SNC meteorites shown for reference) in a conventional AFM diagram using the relative wt. % for alkalis ($A = K_2O + Na_2O$), ferrous iron ($F = FeO_T$), and magnesium ($M = MgO$) to distinguish between tholeiitic and calc-alkaline trends. Most Gusev rocks plot in the tholeiitic series above the two differentiation trends, indicating iron enrichment with differentiation [McSween et al., 2006].

When projected in Al_2O_3, $CaO^* + Na_2O + K_2O$, and FeOT + MgO (A-CNK-FM) compositional space [Nesbitt and Young, 1989], Gusev basalts plot as a linear trend below and subparallel to the olivine-feldspar join (Figure 3.6B). Compositional heterogeneity of these rocks is demonstrated by their distribution as a linear spread along the olivine-feldspar-join, rather than as a single cluster. Such scatter documents the varying proportions of mineral phases that comprise Gusev basaltic rocks [McSween et al., 2006]. With the bedrock compositions established, it is possible to compare whether, or how much, soil compositions deviate from the bedrocks within Gusev Crater.

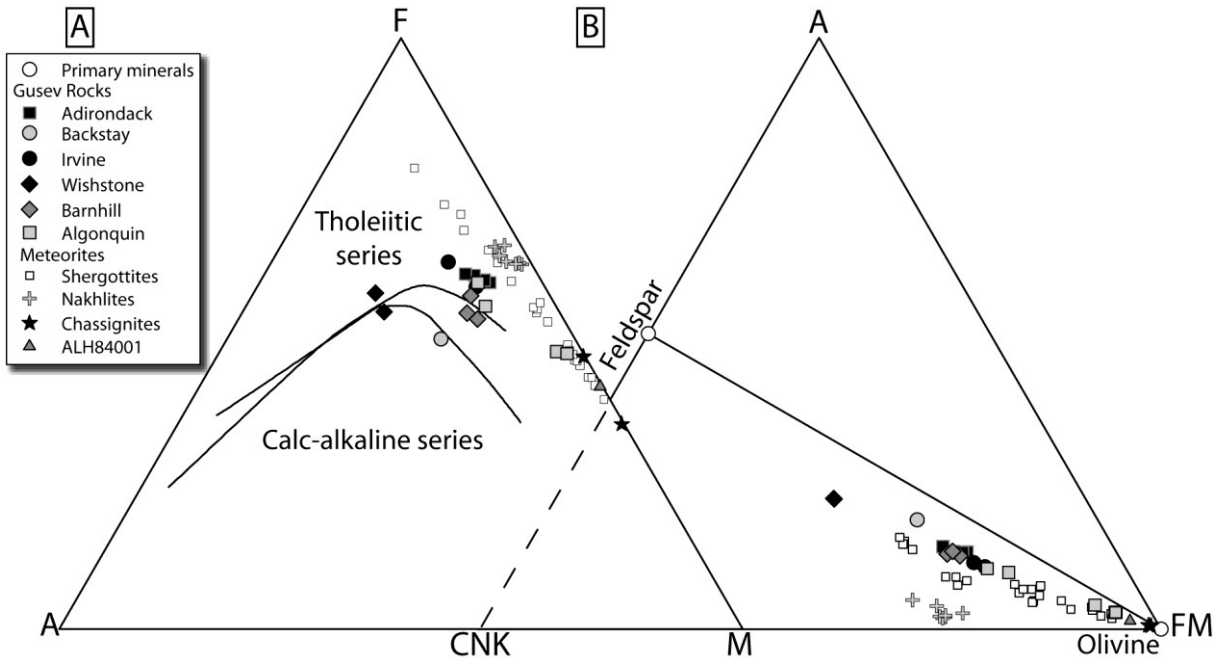

Figure 3.6. (A) Conventional AFM plot for Gusev basaltic rocks, with SNC meteorites for comparison. Gusev rocks grouped by class from McSween et al. [2008] plot in the tholeiite series. Upper series boundary from Kuno [1968], lower boundary from Irvine and Baragar [1971]. SNC meteorites include 23 shergottites [Lodders, 1998; Rubin et al., 2000; Barrat et al., 2001, 2002; Dreibus et al., 2002; Jambon et al., 2002; Shirai and Ebihara, 2004; Gillet et al., 2005; Ikeda et al., 2006; Anand et al., 2008; Lin et al., 2008; Sarbadhikari et al., 2009], 7 nakhlites [Lodders, 1998; Day et al., 2006; Treiman and Irving, 2008], 2 chassignites [Lodders, 1998; Beck et al., 2006], and ALH84001 [Lodders, 1998]. (B) A-CNK-FM projection for Gusev basalts showing considerable compositional heterogeneity along a trend subparallel and just below the olivine-feldspar join.

4.2. Alteration Components

4.2.1. Clay Production by Hydrolysis

Variations in soil chemistry that result in data plotting perpendicular to the olivine-feldspar join are minor, but likely represent important mixing or alteration processes. Given that liquid water is thought to have played an important role in the early history of Mars [Burr, 2010; Carr and Head, 2010] and leaves a distinct geochemical signature because of water-rock interactions [e.g., Nesbitt et al., 1996; Nesbitt and Markovics, 1997], it is necessary to explore whether hydrolysis was also an important process in soil formation on Mars, or whether older clays may have been reworked into present soils. Furthermore, the soil mineral estimates discussed above (Figure 3.1) indicate that ~5% clay is present. Terrestrial weathering processes provide an analogy with which to evaluate the abundance of secondary clay phases. Chemical weathering by hydrolysis reactions dominates terrestrial soil development, and results in the increasing production of clay minerals as weathering proceeds (Figure 3.7A). The extent of chemical weathering, and thus, clay production, can be expressed using the relative molar proportions of Al_2O_3, $CaO + Na_2O + K_2O$, and $FeO_T + MgO$ (A-CNK-FM) [Nesbitt and Wilson, 1992; Nesbitt et al., 1996], where weathering products are represented by the accumulation of insoluble clays (Al_2O_3), the preferential loss of plagioclase ($CaO + Na_2O$), and the loss of ferromagnesian minerals such as olivine and pyroxene ($FeO_T + MgO$).

A ternary plot of the terrestrial Baynton basalt weathering profile (suite "A") [Nesbitt and Wilson, 1992] (Figure 3.7A) demonstrates three stages of a typical basaltic weathering profile, which are determined by the order of weathering susceptibility of primary igneous mineralogy during weathering. First, olivine (plots on the $FeO_T + MgO$ apex) is most rapidly weathered

resulting in the movement parallel to the olivine-feldspar join away from the FM apex, which the first three samples represent (Figure 3.7A, segment 1). After the initial olivine loss, the weathering trajectory changes and crosses perpendicular to the olivine-feldspar join (Figure 3.7A, segment 2) because of the weathering of feldspar and glass to clays minerals accompanied by a net loss of CaO, Na_2O and K_2O. In advanced chemical weathering, the trajectory shifts again, moving along the A-FM join toward the A apex (Figure 3.7A, segment 3). This trend represents the accumulation of mature, increasingly aluminous clays, such as kaolinite.

If soils formed by chemical weathering, or contained a significant admixture of weathered components, then they would plot away from the olivine-feldspar join, following a trend toward the A-FM axis [e.g., Nesbitt and Wilson, 1992]. Unlike the terrestrial Baynton profile, sediments in Gusev Crater are not significantly enriched in Al_2O_3 or significantly depleted in FeO_T + MgO [Hurowitz and McLennan, 2007] relative to all local rocks (Figure 3.7A). A similar relationship is seen in rocks and soils from the Pathfinder landing site [McSween and Keil, 2000; McLennan, 2000]. Instead, Gusev soils plot directly on top of Gusev bedrocks, but with a smaller spread in the FM component. With the composition of soils falling within the compositional range of igneous rocks, we interpret the soils to mostly represent the composition of igneous material. Limited chemical weathering of soils in arid conditions [Hausrath et al., 2008] should result in the formation of secondary clay minerals that plot

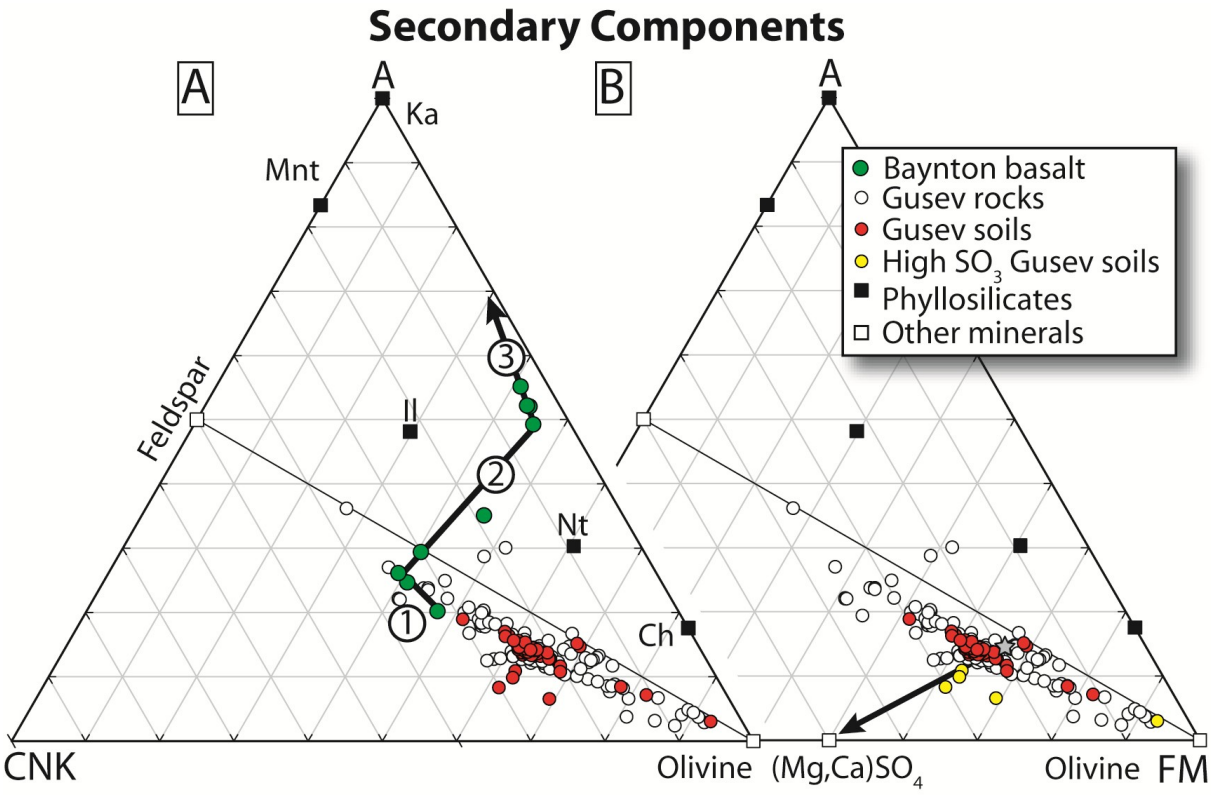

Figure 3.7. (A) Terrestrial Baynton basalt weathering profile analog, arrow 1 shows olivine loss and clay production, arrow 2 shows feldspar loss and clay production, and arrow 3 shows eventual accumulation toward Al_2O_3 apex from phyllosilicate accumulation. Baynton data from Nesbitt and Wilson [1992]. Gusev Crater soil chemical compositions vary primarily subparallel to the olivine-feldspar join, indicating an igneous composition, similar to local rocks, and lack significant phyllosilicate production by hydrolysis as seen in the Baynton analog. (B) Minor compositional variations perpendicular and below the olivine-feldspar join (arrow) can be attributed to additive components such as sulfate $(Mg,Ca)SO_4$ demonstrated by SO_3 enriched soils (yellow points) that trend from a hypothetical source rock (star) toward the sulfate end-member. Phyllosilicate abbreviations: Ka, kaolinite; Mnt, montmorillonite; Il, illite; Nt, nontronite; Ch, chamosite.

along a predictable weathering pathway as they accumulate. Without progressive movement toward the A-FM axis, soils cannot contain large quantities of clays and, therefore, are not the products of significant chemical weathering.

The presence of secondary phyllosilicates in soils has been suggested from thermal deconvolution [Rogers and Aharonson, 2008; McSween et al., 2010]. Our estimate here (Figure 3.1) suggests about 5%, which is little enough to not move the bulk chemistry of most Gusev soils far from unaltered basalt [McSween et al., 2008]. The absence of large quantities of clays requires water-limited conditions for soils at the MER landing sites as recognized by McLennan et al. [2005] and Hurowitz and McLennan [2007].

4.2.2. Sulfate Mixing

In addition to the presence of phyllosilicates, the addition of sulfates (Figure 3.1) represents another mechanism for soil compositions to deviate from bedrock. Sulfate addition to soil follows a path from any source composition to the position of $(Mg,Ca)SO_4$ in A-CNK-FM space (Figure 3.7B, arrow). Several very distinct soil compositions lay below the main data set. Four soil samples plot below the field of most soils (401, PasoRobles disturbed; 427, Paso light; 1013, Berkner Island1; 1098 Tyrone), and are elevated in SO3 ranging from 22 to 32 wt. %. These high-S soils plot along the mixing trajectory from bedrock (Figure 3.7B, star) to an idealized sulfate $(Mg,Ca)SO_4$ end-member (Figure 3.7B). Although a representative bedrock provenance is not known, most soils almost certainly derive from a composite of different basalts combined with other pre-existing mineral phases [e.g., McSween et al., 2010; McGlynn et al., 2011]. A

fifth high SO_3 sample (723, Arad Samra), with 38 wt. % SO_3, plots adjacent to the FM apex, and represents the accumulation of Fe-sulfate [Yen et al., 2008] rather than the accumulation of olivine or pyroxene. Further analysis of the implications of sulfate mixtures is presented in section 4.4.2.

4.3. Olivine Dissolution by Acid-Sulfur

The detection of jarosite at the Meridiani Planum landing site by MB [Klingelhöfer et al., 2004], and devonvolution of MiniTES spectra similar to jarosite in outcrops [Christensen et al., 2004], and high SO_3 from APXS [Rieder et al., 2004] spectrometers suggests that arid, oxidizing, acidic, and high-sulfate conditions [Elwood Madden et al., 2004] may play a prominent role in soil alteration [McLennan et al., 2005]. Olivine loss by acid-sulfur dissolution has been suggested as an important method of chemical weathering on Mars [Hurowitz and McLennan, 2007], an idea supported by the detection of alteration rinds thought to be associated with olivine dissolution. Under such conditions the preferential loss of olivine, relative to other major components, results in the depletion of FeO_T + MgO and can be represented by the compositional movement away from the FM apex along a trend parallel to the olivine-feldspar join in A-CNK-FM compositional space (Figure 3.8A, thick arrow). The extent of compositional alteration by acid-S-driven olivine dissolution has not been fully explored yet. Furthermore, it is unclear if weathering by acid-S forms the determinant compositional control of Martian soils.

In order to test the acid-S hypothesis, we first project rock and soil data in the A-CNK-FM plot (Figure 3.8A) onto the CNK-FM join (Figure 3.8B) to eliminate the variable

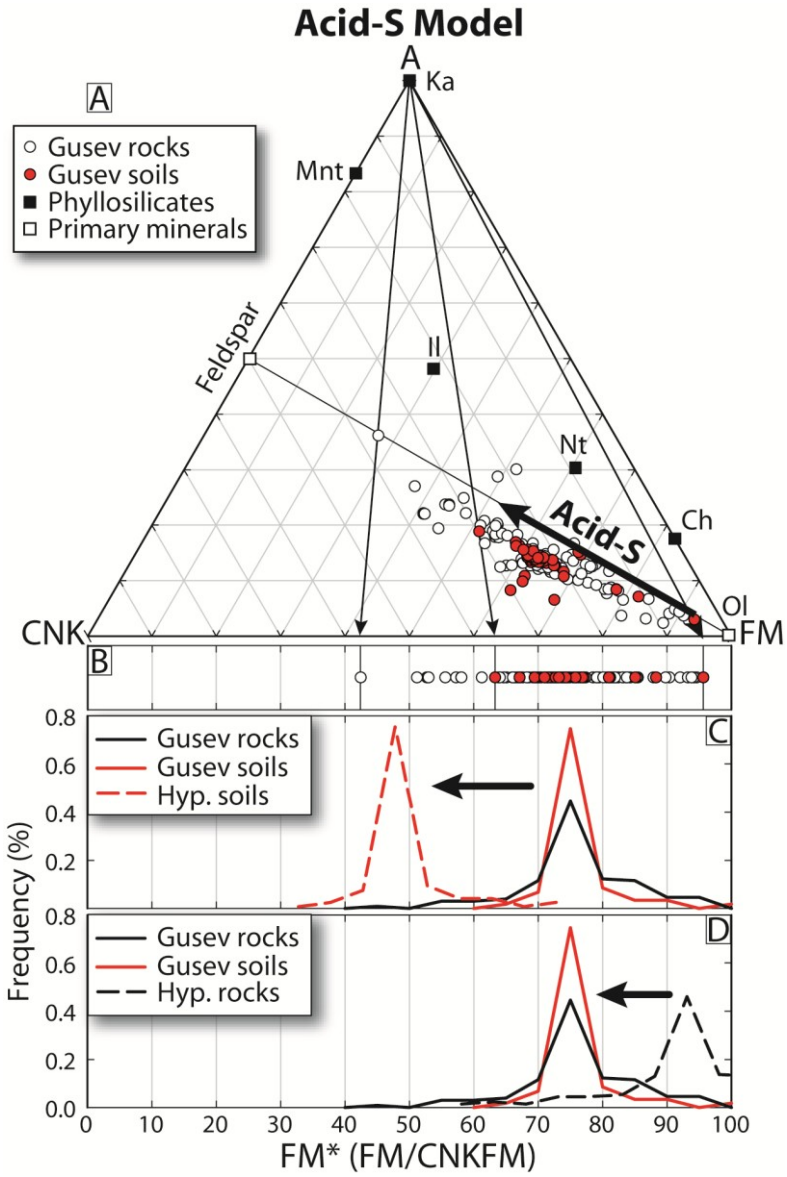

Figure 3.8. (A) Idealized alteration pathway for olivine dissolution by acid-S away from the FM (FeO_T + MgO) apex. However, (B) soils (n = 59) and rocks (n = 130) have similar compositions demonstrated by the molar proportions of FM* = FM/CNKFM (FeO_T + MgO / CaO + Na_2O + K_2O + FeO_T + MgO), expressed as histograms of soil and rock chemistry in C and D. If olivine dissolution was a significant mechanism of soil alteration, then (C) a population of hypothetical FM*-rich source rocks (black dashed line) would be required to explain the current composition of soils within Gusev Crater. (D) Alternatively, hypothetical soils altered from analyzed rocks within Gusev Crater should be relatively depleted in FM* (red dashed line). Instead, similarities in soil and rock compositions indicate minimal compositional alteration. Hypothetical positions are only a demonstration of the general direction expected from changes in FM* chemistry and do not correspond to actual modeled compositions. See Figures 3.1 and 3.6 for mineral abbreviations.

concentrations of Al_2O_3 from the sample set. Here we establish that projection as the quantity FM*, where FM* = molar FM/CNKFM. If soil compositions resulted from olivine dissolution by acid-S, then there should be recorded as a major change away from the FM* end-members. As seen in Figure 3.8B, soils have a narrow range of FM* values (FM* = 95–60%, average = 73.6%) when compared to rocks (FM* = 95–42% average = 73.6%). Frequency percent histograms for rocks and soils show that soils and rocks have similar distributions with identical peaks at FM* ≈ 75% (Figures 3.8C and 3.8D). Such overlap further supports the interpretation of compositional similarity between bedrocks and soils. If the current distribution of bedrocks within Gusev Crater form the source for soils, then soils altered by acid-S should have a lower FM* value when compared to local rocks (Figure 3.8C, dashed red line), although they clearly do not. Acid-S appears to play only a minor role in the development of soils on Mars. Alternatively, to account for the present compositional overlap between rocks and soils, bedrocks could have started at a higher FM* value (Figure 3.8D, dashed black line), then moved to lower FM* values as olivine dissolved through acid-S. However, the lack of abundant source rocks with greater FM* values (Figure 3.8D, solid black line) strongly suggest that soils did not form via this pathway.

We further approach determining the possible extent of compositional alteration in bedrock by olivine loss using linear chemical mixing models from three source rocks classes (Figure 3.9). The mean compositions of three rock classes, Algonquin, Adirondack, and Irvine [McSween et al., 2008] that have corresponding APXS and MB spectra were selected to provide a complete range of initial igneous compositions. First, an extreme case of weathering is modeled from the

complete removal of all olivine from the three rock end-members. Algonquin-class rocks have the highest proportion of olivine among all rocks within Gusev Crater. A mean proportion 58 wt. % olivine (Fo_{59}) from four samples (A660, Larrys Bench, A675, Seminole Abiaka, A688, Algonquin, A700, Comanche Palomino) creates a representative Algonquin-class end-member. Weathering of the compositional mean is modeled in Figure 3.9A starting from the Algonquin end-member (blue point) at 58 wt. % olivine to 0 wt. % olivine in 10% mixing increments (line with ten black points). The complete removal of olivine from the Algonquin-class mean source rock results in a decrease of −26.1% FM* (Figure 3.9B, dashed line), which exceeds the lowest FM* values for current soils. Instead, an Algonquin-class source would require a 50 to 80% mixing with the olivine-free end-member in order to match the chemical composition of most soils (Figure 3.9A). In addition to chemical modeling above, the mineralogy of rocks within Gusev Crater must also conform to soil mineralogy estimates. To match the proportion of olivine estimated in soils (Figure 3.10 and Table 3.1) a 32–47 wt. % loss of olivine for Algonquin-class rocks is required and would imply significant levels of chemical weathering, which would result in more than olivine dissolution. Once large water-rock interactions are involved with basalt weathering, the resulting soil compositions would move off the olivine-feldspar join as recognized by Hurowitz and McLennan [2007]. Consequently, this path is most unlikely without associated alteration phases.

With a mean proportion of 23 wt. % olivine (Fo_{46}), four Adirondack-class samples (A34, Adirondack, A60, Humphrey, A86 Mazatal, A100 Route 66) provide a second source rock to model olivine loss by acid-S alteration. Olivine loss is again modeled as mixing in 10%

increments away from the Adrindack-class mean source rock (Figure 3.9C, blue point). The complete destruction of olivine results in a decrease of −17.2% FM* and is too depleted to match the chemical composition of soils. Soils formed by the total removal of olivine would be significantly reduced in FM* (Figure 3.9D, dashed line) compared to the current soils. The current compositions of Adirondack rocks are generally equal to the average soil composition, and there is not a large abundance of lower-FM* soils that would have been altered by acid-S. A mixture of 0 to 40% olivine-free Adirondack rock end-member is required to match soils in Gusev Crater (Figure 3.9C), although this starting composition fails to meet any of the FM*-rich soils. A 10–13 wt. % olivine removal from Adirondack rocks (Figure 3.10) are needed to match the soil mineralogy but such a loss exceeds the FM* compositions of most soils. A removal of the initial olivine proportion by ~50% to match average soil olivine promotions would result in soils that are depleted in FM* relative to most soils. A source rock with similar Adirondack-type chemistry, but with a lower initial proportion of olivine would be needed to explain the current composition of soils by acid-S weathering.

Soils, as loose sediment, have the highest weathering potential due to the higher surface area when compared to the exposed surface area of basaltic rocks. Therefore soils would be expected to represent the most chemically weathered material on the surface of Mars. Instead, only a small amount of chemical alteration is present, either in the form of olivine dissolution by acid-S alteration, or from phyllosilicate production. With 12 wt. % olivine and

Figure 3.9. Maximum potential compositional alteration of soils modeled by the complete removal of olivine in 10% increments from the mean composition of three potential source rocks. (A) Alteration of Algonquin class with 48 wt. % initial olivine (Fo_{59}) (B) shifts modeled soils $\Delta FM^* = -26$ beyond analyzed soils. Only 40 to 80% mixing is permissible to match most soils. (C) Loss of olivine from Adirondack class at 23 wt. % olivine (Fo_{46}) plots beyond the position of analyzed soils, with a maximum mixing of 40% needed to create soils. (D) The $\Delta FM^* = -17$ shift in modeled soils is depleted relative to analyzed soils. (E) Modeled alteration from Irvine class with 6 wt. % olivine (Fo_{61}) cannot explain analyzed soil compositions. (F) The $\Delta FM^* = -3$ shift is too small to form Gusev soils.

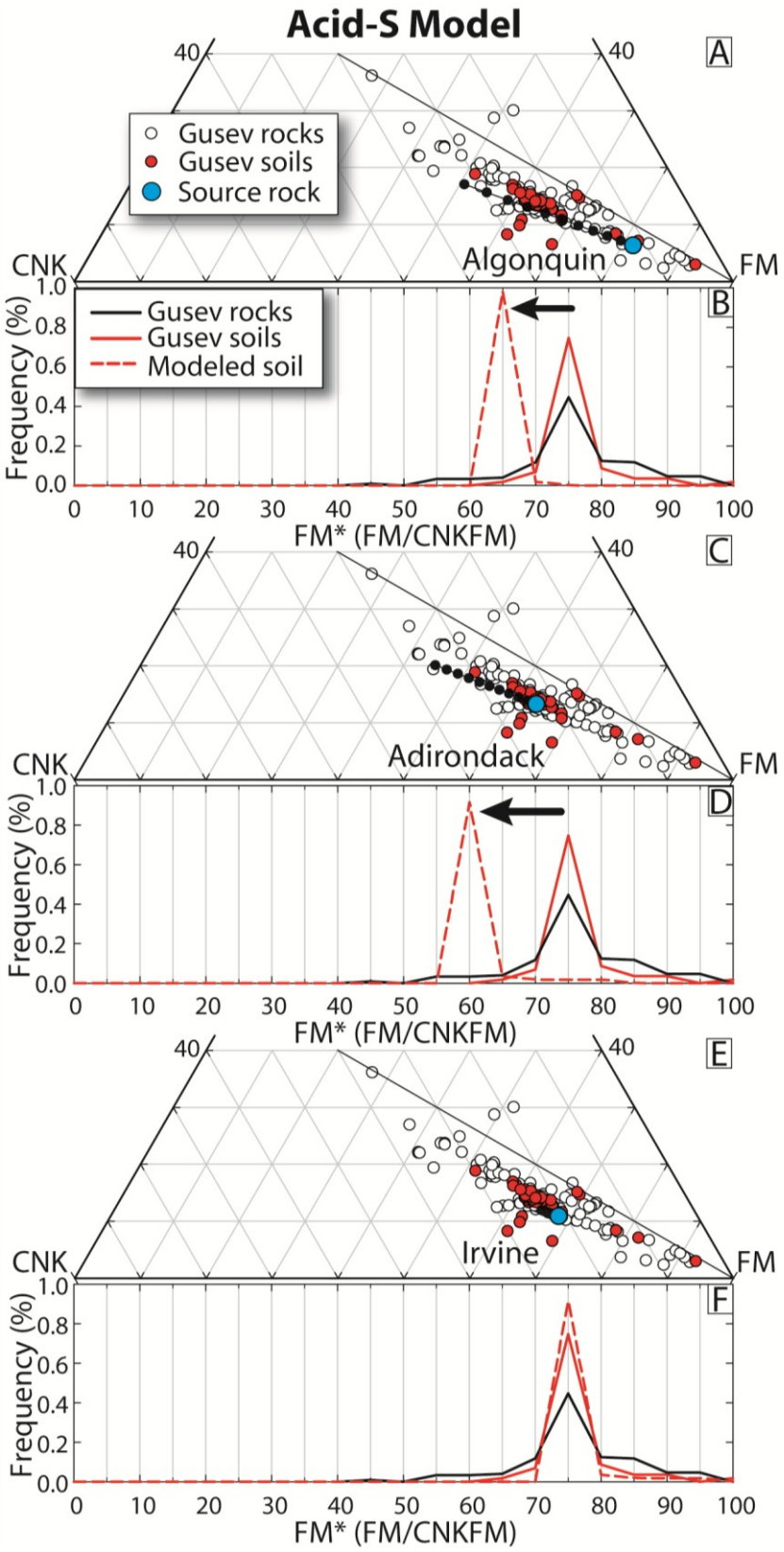
Acid-S Model
A
40
40
Gusev rocks
Gusev soils
Source rock
CNK
FM
Algonquin
B
Frequency (%)
1.0
0.8
0.6
0.4
0.2
0.0
Gusev rocks
Gusev soils
Modeled soil
0
10
20
30
40
50
60
70
80
90
100
FM* (FM/CNKFM)
C
Adirondack
D
E
Irvine
F

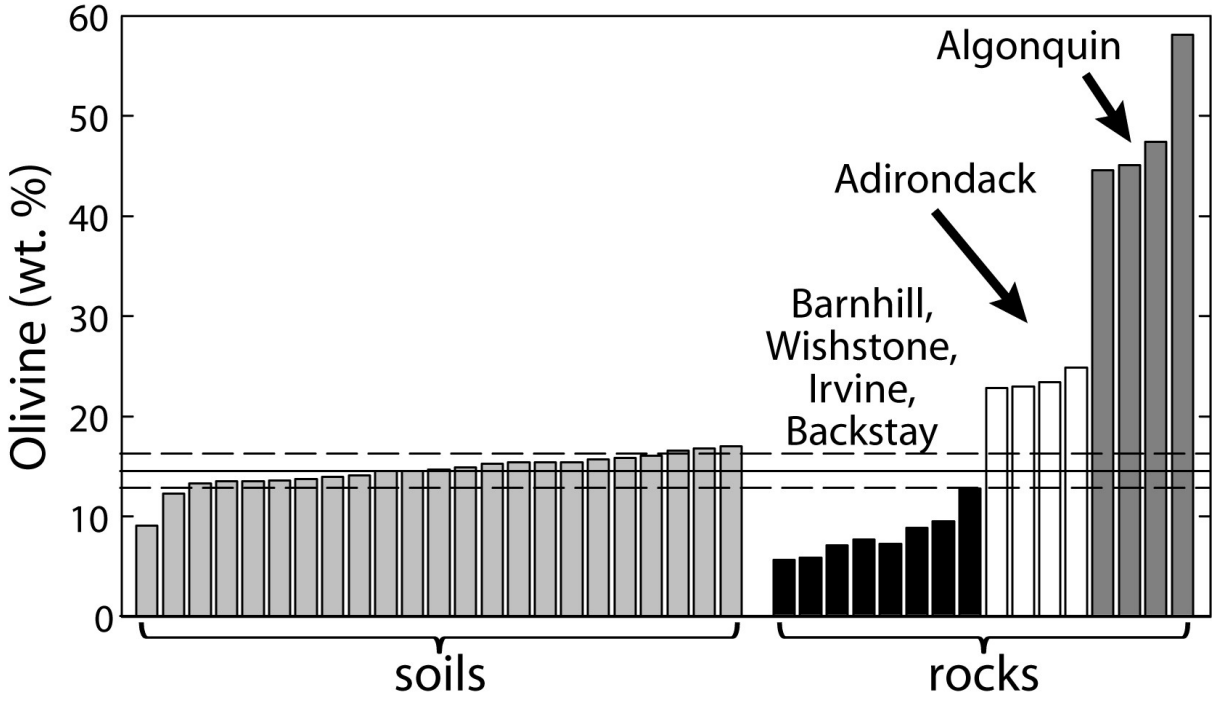

Figure 3.10. If soils require significant composition weathering from olivine loss, then they cannot be derived from many rocks in Gusev Crater. Soils are homogeneous in olivine (14 wt. %), and cannot be derived from Barnhill, Wishstone, Irvine, and Backstay classes that are depleted in olivine relative to soils. An Adirondack source would require a reasonable loss in 9–12 wt. % loss in olivine.

5 wt. % clays, soils in Gusev Crater are compositionally similar to basaltic rocks and do not represent significant chemical weathering.

4.4. Effects of Physical Modification of Soils by Hydrodynamic Sorting

4.4.1. Potential Redistribution of FeO_T + MgO from Physical Sorting

The greatest variation in soil chemistry is subparallel to olivine-feldspar join, and is therefore the most complicated feature to evaluate. As determined above, chemical processes are not necessary to explain Mars soil compositions leading us to consider whether physical processes might be responsible. With the importance of aeolian reworking of surface sediments [McGlynn et al., 2011], hydrodynamic sorting [McLennan, 2000; McSween and Keil, 2000; McGlynn et al., 2008; Karunatillake et al., 2010] serves as a process capable of redistributing mineral concentrations, and thereby modifying soil compositions without chemical weathering of source rocks within Gusev Crater. Impact ejecta, fallback, and subsequent aeolian transport may be capable of sorting minerals and glass components with different grain sizes and densities into deposits with compositional differences to the original source. Density separation can occur from differences in settling velocities, grain entrainment thresholds, or grain transport velocities [e.g., Hughes et al., 2000], with the potential for significant compositional modification in soils on Mars.

The effects of sorting on soils compositions are evaluated with a simple two-component mixing model involving the Adirondack-class rock mean as a source end-member. Olivine removal is modeled from the Adirondack-class mean (Figure 3.11A, blue point) by unmixing with an Adirondack-mean end-member that contains no olivine (Figure 3.11A, arrow 1). With the

decrease in olivine, the resulting soil composition moves left from the Adirondack mean and away from the FM apex (Figure 3.11A) in the same manner as acid-S modeled in section 4.3. A similar trend would also result from a low-Ca pyroxene end-member. However, a greater proportion of olivine in coarse sediments compared to fine grains has also been identified from MiniTES spectra in Gusev Crater [Bandfield et al., 2011]. Acid-S has the possibility of driving soil compositions away from the Adirondack end-member, but cannot explain the process of concentrating the olivine necessary for soils enriched in FM-rich phases. Unlike acid-S weathering, physical processes can also concentrate different mineral proportions. The transport and concentration of olivine is modeled from the Adirondack-class mean (Figure 3.11A, blue point), and mixed with an olivine end-member. Olivine accumulation at 10% increments is represented by points that extend away from the Adirondack source toward the FM apex (Figure 3.11A, arrow 2). Impact and aeolian transport responsible for olivine mineral separation is modeled as a 40% loss in olivine in addition to a 10% accumulation in olivine from a potential Adirondack mean source rock. On the basis of modeled compositions from mixing models in Figure 3.11A, it is possible to attribute the observed pattern of soil compositions to moderate olivine mineral sorting.

4.4.2. Mixing of Secondary Minerals

In addition to physical sorting, about 5% of phyllosilicates may be present within Gusev soils (Table 3.1 and Figure 3.1). To model the possible addition of clays, Adirondack, Irvine, and

Figure 3.11. (A) Major compositional variations subparallel to the olivine-feldspar join in Gusev soils can be explained by the potential compositional range from hydrodynamic FeO_T + MgO redistribution modeled by the complete removal (arrow 1) olivine from an Adirondack source shown by small black lines emanating from each source rock. Accumulation of olivine (arrow 2) is modeled from an Adirondack source to an idealized olivine (Fo_{46}) end-member. (B) Minor variations in soil chemistry perpendicular to the olivine-feldspar join can be attributed to mixing of secondary mineral components. Chemical mixing models plotted at 20% increments (black points) between bedrock and nontronite (lines 1), a hypothetical mixing end-member, demonstrate the potential for up to 20% phyllosilicate component within soils, from Adirondack (Ad), Irvine (Ir), and Algonquin (Al) rocks. Variations in soil chemistry parallel to the A-CNK axis below the olivine-feldspar join demonstrate the potential for sulfate $(Mg,Ca)SO_4$ mixing (lines 2). (C) Sorting of crushed terrestrial basalt analogs from unaltered Cima and Kilauea whole rock samples (dark circles) demonstrates extensive compositional variations from physical sorting. Accumulation of olivine phenocrysts in Kilauea samples result in greater compositional variation than aphanitic Cima sediment.

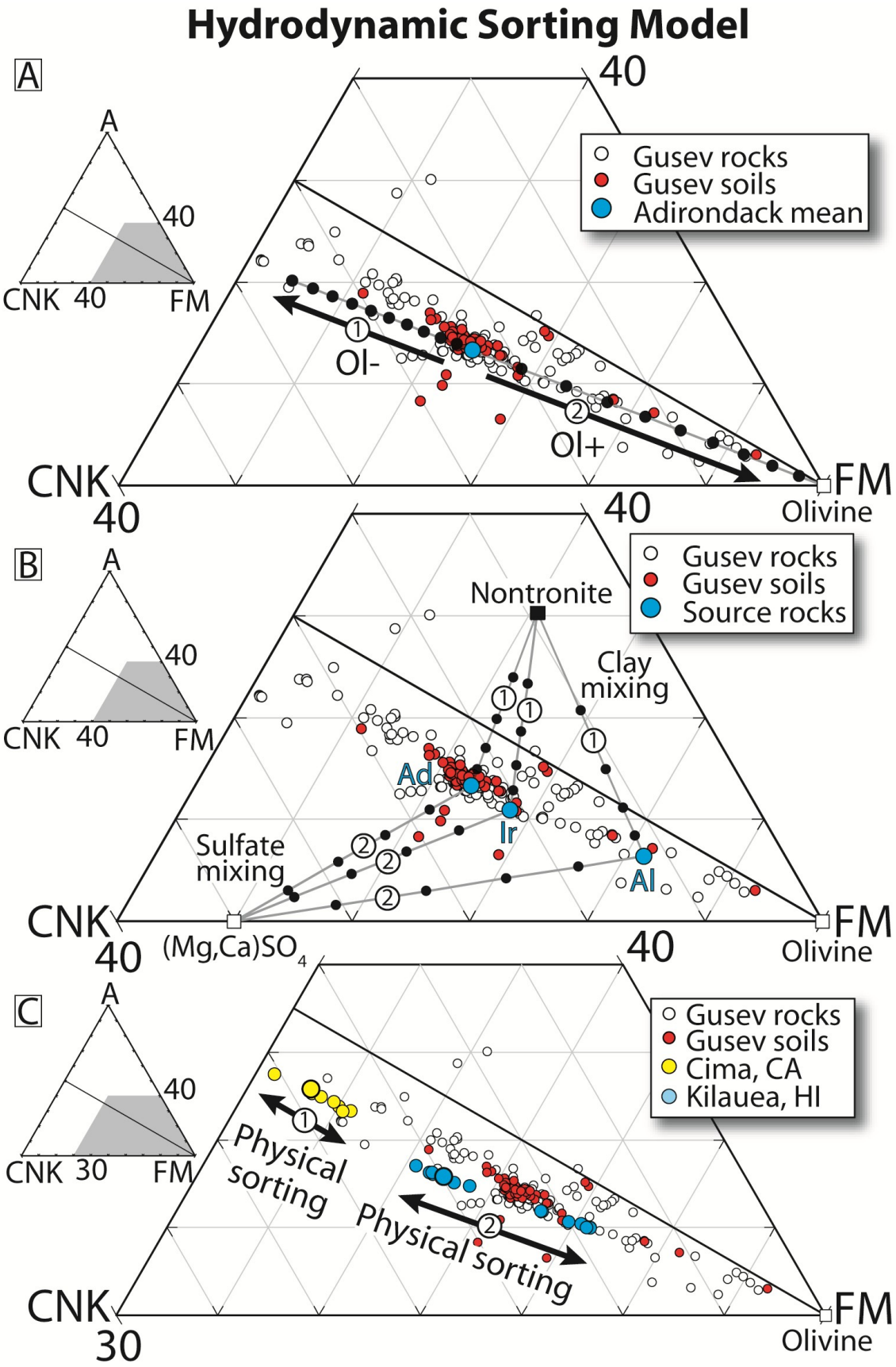
Hydrodynamic Sorting Model
A
A
40
CNK 40 FM
Gusev rocks
Gusev soils
Adirondack mean
Ol-
Ol+
CNK
40
40
FM
Olivine
B
A
40
CNK 40 FM
Gusev rocks
Gusev soils
Source rocks
Nontronite
Clay
mixing
Ad
Ir
Al
Sulfate
mixing
CNK
40
(Mg,Ca)SO4
40
FM
Olivine
C
A
40
CNK 30 FM
Gusev rocks
Gusev soils
Cima, CA
Kilauea, HI
Physical
sorting
Physical sorting
CNK
30
FM
Olivine

Algonquin bedrock end-members (Figure 3.11B, blue points) are mixed with nontronite end-member (Figure 3.11B, arrows 1, black dotted lines) in 20% increments. Up to 20% nontronite can be mixed with the source rocks and remain within the compositional field of soil samples (Figure 3.11B, red points). In this model, nontronite is selected as a possible clay mixture in order to assess the potential for clay mixing, but is not intended to identify nontronite as a known component within soils. Other clay minerals, such as montmorillonite, could also be present.

Soil compositions must also account for the addition of an idealized Mg- and Ca-rich sulfate (Figure 3.11B; 1:1 modal Mg/Ca ratio), which we estimate to represent about 10% of the soil (Figure 3.1). To test the potential significance of added sulfates, the same bedrock end-members were mixed with $(Mg,Ca)SO_4$ at 20% increments. Although only a small amount of sulfate addition is permitted from the selected bedrock end-members to produce typical soil compositions (Figure 3.11B), the likely soil source represents a composite of different basalt compositions with a mixture of older secondary components, including phyllosilicates [McSween et al., 2010]. Such a bulk source composition would lie closer to the olivine-feldspar join (Figure 3.7B, star) than do single bedrock values so that soil data most likely have compositions that do not perfectly overlap the composite provenance. Up to 20% sulfate can be mixed with many potential source rocks and remain within the compositional field of soil samples when derived from other possible bedrock end-members.

4.4.3. Sorting Analogs

Chemical mixing models are inherently idealized. Therefore two terrestrial analogs are used to demonstrate the potential for identifying compositional modification by physical sorting (chapter 4). The first sample is vesicular, aphanitic basalt from the Cima volcanic field in the Mojave Desert, CA. The basalt has a primary mineralogy of olivine, plagioclase, clinopyroxene, glass, and equant opaque minerals. A second sample from the Kilauea volcano in Hawaii is a vesicular, porphyritic hawaiite with a primary mineralogy of olivine, plagioclase, glass, and clinopyroxene phenocrysts, and a groundmass of olivine, clinopyroxene, and plagioclase. The aphanitic (<1 mm) Cima and porphyritic (1–10 mm) Kilauea samples were selected to evaluate how a range in igneous textures and different initial compositions can influence compositional modification from physical sorting.

To mimic physical processes of impact comminution and aeolian sorting on Mars, the two basalt samples were crushed, sieved into 0.5 ϕ fractions, and analyzed for major and trace element geochemistry (chapter 4). The range of compositions in crushed sediment samples is controlled by (1) the initial bulk rock mineral composition and (2) the igneous textures of the source rocks. Both of these parameters are represented by the diversity in composition and textures of the Cima and Kilauea rock samples. The A-CNK-FM composition of sieved sediment from both samples plot parallel and below the olivine-feldspar join (Figure 3.11C). A lower proportion of olivine in Cima samples is expressed as depletion in FM chemistry. Despite the low initial proportion of olivine in Cima sediment, olivine becomes concentrated relative to the bulk rock (Figure 3.11C, arrow 1) in medium (2.0 ϕ) to very fine sand (4.0 ϕ) as shown by the yellow

points moving away from the bulk rock (Figure 3.11C, enlarged yellow circle) toward the FM apex. The greatest concentration of olivine occurs at fine sand (3.0 ϕ) corresponding to the dominant crystal size of crushed olivine.

Crushed sediment from the Kilauea sample has a greater FM* compositional range (ΔFM* = 20.8) than Cima samples (ΔFM* = 9.6) as seen in arrow 2 (Figure 3.11C). Olivine phenocrysts in the Kilauea sample are concentrated from coarse (0.5 ϕ) to vey fine sand (4.0 ϕ) with the greatest enrichment from medium (2.0 ϕ) to fine sand (3.0 ϕ). With a higher initial proportion of olivine and the presence of olivine as phenocrysts, the behavior of compositional sorting is more pronounced. The concentration of olivine is represented by higher FeO_T + MgO and a trajectory diverging away from the source rock toward the FM apex, while the removal of olivine is represented by lower FeO_T + MgO concentrations with a trajectory away from the FM apex (Figure 3.11C, arrow 2). Olivine phenocrysts in the Kilauea basalt allow for a greater compositional range from olivine redistribution, and the concentration of olivine occurs at coarser grain sizes than observed aphanitic Cima sediments where olivine is not extensively concentrated in proportion to other major and secondary minerals. In both samples, mineral fractionation from physical sorting serves as a plausible explanation to account for compositional variations in Gusev soils without alteration by chemical weathering (chapter 5).

4.5. Compositional Modification of Sediments' Soil Textures

Compositional modification of Gusev soils by hydrodynamic sorting can be evaluated by comparing soil FM (modal FeO_T + MgO) compositions with the grain size of soils. There is a

progressive increase in FM from coarsest to finest sediments (Figure 3.12). Minor differences among compositions of dust, fine to medium sand, and medium to coarse sand are present. The highest FeO_T + MgO concentrations occur in bright dust, which are surfaces with < 100 μm grains that are too small to directly measure with the Microscopic Imager (MI). Dark soils which contain fine to medium sand are also enriched in FM (Figure 3.12). In contrast, bed form armor soils, which contain medium to coarse sand, are depleted in FM and in olivine (Figures 3.3A and 3.3B), relative to other soils. The FM enrichments in fine sand and dust samples may represent the concentration of olivine in finer sediments in a manner similar to the accumulation of olivine observed in the Cima and Kilauea terrestrial analogs. The ability of olivine to concentrate in finer grains may imply the crystal size of olivine is small, although olivine megacrysts have been reported in some abraded Gusev rock MI imagery [McSween et al., 2008]. Trajectories of modeled olivine loss (Figure 3.11B, arrow 2) and mixing (Figure 3.11B, arrow 3) are distinct from soil observations (Figure 3.12), and are not exclusively controlled by olivine redistribution. Instead other FeO- and MgO-bearing minerals including pyroxene and FeO_x are also concentrated.

Soil compositions plot parallel and below the olivine-feldspar join, and appear to be in part controlled by the effects of transport, abrasion, and sorting, without significant chemical alteration by acid-S. Minor variations in FeO_T + MgO primarily reflects the separation of fine

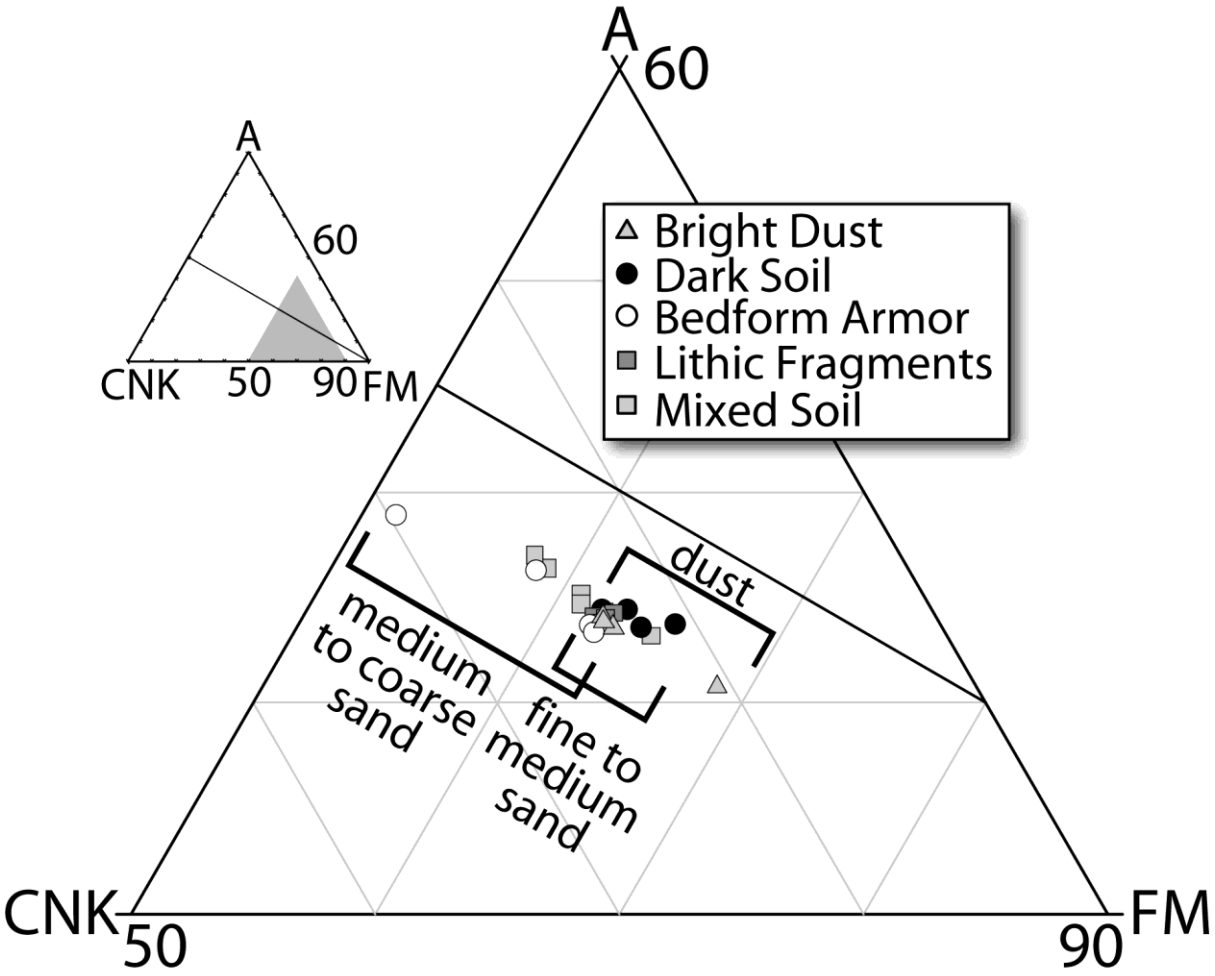

Figure 3.12. Minor hydrodynamic sorting of grain size control on FeO_T + MgO compositions. FM is concentrated in fine sand and dust (dark soil, bright dust) and depleted in coarse sand (bed form armor). The trajectory of soil compositions is not straight toward an olivine end-member indicating that compositional variations are not exclusively controlled by olivine redistribution, and include other FM-rich minerals.

sands in dark soils possibly capable of saltation, from creep transported coarse sands in ripples that are probably inactive at present. The concentration of olivine, as a result of hydrodynamic sorting, would require (1) the availability of individual minerals to be isolated, such as from the density separation of olivine, and (2) a transport mechanism to separate and concentrate the proportion of individual minerals, such as bolide impacts or aeolian sorting. Both of these conditions appear feasible on the surface of Mars. Although it is not clear how active transport is on the current surface [Jerolmack et al., 2006; Sullivan et al., 2008] sand mobility from active dunes has been reported [Chojnacki et al., 2011], and sorting by physical transport must have been relevant in the past. With the conditions for hydrodynamic sorting in place, soils in Gusev Crater can therefore represent impact comminuted sediment with minor, but detectable compositional modification by subsequent transport.

4.6. Soil Formation

Detailed textural analysis of soils imaged at Gusev Crater [McGlynn et al., 2011] indicates that the upper layer of soil on the surface of Mars originates from comminuted impact material that has been mixed with volcaniclastic deposits and possible alteration components, and transported by surfaces processes. Compositional results demonstrate that most soils are poorly weathered based on the presence of olivine from individual soil MB spectra and from the absence of FM* depletion of soil APXS chemistry relative to most rocks. Instead, soil compositions appear to be modified by surface processes as demonstrated by the compositional sorting of sediments (Figure 3.11), consistent with earlier findings [McGlynn et al., 2011]. Such results enhance the textural model with the addition of compositional results that support soils generated, and largely

modified, by physical processes, and do not require (but does not exclude) chemical alteration by acidic weathering.

5. Conclusions

The results in this study demonstrate that chemical weathering of basalts on Mars is limited, but the addition of secondary and alteration phases is permissible. Several important implications for modeling chemical weathering of basaltic material on Mars are summarized as follows:

1. Soils in Gusev Crater and Meridiani Planum have a basaltic parent and a composition including primary igneous minerals as well as secondary alteration minerals. Primary minerals, the abundance of which is estimated from the integration of Mossbauer (MB), MiniTES and APXS spectra, include in decreasing abundance plagioclase, pyroxene, olivine, apatite, magnetite, and chromite. Secondary (alteration) components include sulfates, amorphous silica, phyllosilicates, nanophase oxides, chlorides, and hematite. The abundances of Fe-bearing minerals are detected from MB spectra. Amorphous silica and phyllosilicate quantities are estimated from limited MiniTES deconvolution, where both are assumed to be present in all soils. All other minerals estimates derive from normative calculations of APXS chemistry.

2. Minor chemical variations for most soil compositions are perpendicular to the olivine-feldspar join. Soils are chemically similar to local bedrocks in Gusev Crater and Meridiani, not having Al_2O_3 concentrations above parent levels that would be expected from the presence of substantial phyllosilicate accumulation. The presence of abundant olivine (11 and 13 wt. % mean for Gusev

Crater and Meridiani, respectively) in all the studied soils also indicates only limited chemical weathering by hydrolysis, despite the occurrence or mixing of a small amount of phyllosilicate minerals (~5 wt. %) that may be present. The addition of sulfate (<20% mixing) to soils is possible when mixed from potential source rocks and remain within the compositional field of soil samples.

3. The major chemical variation for most soil compositions is subparallel to the olivine-feldspar join. Olivine dissolution by acid-S weathering was modeled by incrementally removing FeO_T + MgO (as a proxy for olivine) from Algonquin, Adirondack, and Irvine rock classes that were selected to represent the range of initial olivine available for weathering. Dissolution from an Algonquin class source requires 32 to 47 wt. % olivine reduction to match most soils, which is unlikely due to the absence of additional weathering products. Weathering modeled from an Adirondack type source rock requires the loss of 10 to 13 wt. % of the original olivine proportion, but would exceed the FeO_T + MgO compositions of most soils. Irvine class rocks have smaller initial olivine concentrations than are found in soils, and cannot be reasonable source rocks. Additionally, both Adirondack and Irvine class rocks cannot be modeled to produce many soils with high FeO_T + MgO compositions, even without any reduction in olivine.

4. Physical comminution by bolide impacts and the effects of abrasion, transport, and sorting contribute to the redistribution of FeO_T + MgO-bearing (mafic) minerals without chemical weathering. The accumulation and removal of FeO_T + MgO (olivine proxy) modeled from a possible Adirondack class rock can match soils with low FeO_T + MgO concentrations by the removal of olivine and can also match soils with high FeO_T + MgO concentrations from the

accumulation of olivine. On the basis of modeled compositions from mixing models it is reasonable to attribute the observed pattern of soil compositions to moderate sorting of FeO_T + MgO-bearing minerals. A grain-size relationship is observed with soil FeO_T + MgO concentrations, where finer-grained soils (dust and fine sand) are enriched in FeO_T + MgO relative to coarser-grained soils (coarse sand), indicating compositional fractionation in soils at Gusev Crater. The physical sorting of soils in Gusev Crater does not necessitate chemical weathering, and is a likely mechanism of soil modification throughout the surface of Mars.

5. Soils are mixtures of comminuted basalts with older, altered components of phyllosilicates and sulfate, are not significantly altered by chemical weathering after formation. Source rock compositions and hydrodynamic sorting of FeO_T + MgO minerals are the dominant control of soil chemistry. When combined with compositional sorting associated with olivine loss, limited weathering, and the physical concentration of olivine, creates a geochemical field in A-CNK-FM space that contains all of the soil data. This observation is consistent with the importance of the co-occurrence of physical sorting and chemical weathering processes in the formation of Mars soils.

6. Acknowledgments

This work was partly supported by a NASA Mars Exploration Rovers grant through Cornell subcontract 39361–6446 to H.Y.M. The authors are grateful to the MER Athena Science Team. We thank Wayne Nesbitt for helpful discussions. We also thank two anonymous reviewers who gave helpful and constructive advice to improve the quality of this manuscript.

References

Amundson, R., et al. (2008), On the in situ aqueous alteration of soils on Mars, *Geochim. Cosmochim. Acta, 72*, 3845–3864, doi:10.1016/j.gca.2008.04.038.

Anand, M., et al. (2008), Mineralogy and geochemistry of shregottite RBT 04262, *Lunar Planet. Sci., XXXIX*, Abstract 2173.

Bandfield, J. L., Glotch, T. D., and Christensen, P. R. (2003), Spectroscopic identification of carbonate minerals in the Martian dust, *Science, 301*, 1084–1087, doi:10.1126/science.1088054.

Bandfield, J. L., Rogers, A. D., and Edwards, C. S. (2011), The role of aqueous alteration in the formation of Martian soils, *Icarus, 211*, 157–171, doi:10.1016/j.icarus.2010.08.028.

Barlow, N. G. (2010), What we know about Mars from its impact craters, *Geol. Soc. Am. Bull., 57*, 1338–1345, doi:10.1016/j.pss.2009.06.006.

Barrat, J. A., et al. (2001), Bulk chemistry of Saharan shergottite Dar al Gani 476, *Meteorit. Planet. Sci., 36*, 23–29, doi:10.1111/j.1945-5100.2001.tb01807.x.

Barrat, J. A., et al. (2002), Petrology and chemistry of the picritic shergottite North West Africa 1068 (NWA 1068), *Geochim. Cosmochim. Acta, 66*, 3505–3518, doi:10.1016/S0016-7037(02)00934-1.

Beck, P., et al. (2006), Petrography and geochemistry of the chassignite Northwest Africa 2737(NWA 2737), *Geochim. Cosmochim. Acta, 70*, 2127–2139, doi:10.1016/j.gca.2006.01.016.

Bell, J. F., III, et al. (2000), Mineralogic and compositional properties of Martian soil and dust: Results from Mars Pathfinder, *J. Geophys. Res., 105*(E1), 1721–1755, doi:10.1029/1999JE001060.

Bertelsen, P., et al. (2004), Magnetic properties experiments on the Mars exploration Rover Spirit at Gusev Crater, *Science, 305*, 827–829, doi:10.1126/science.1100112.

Bibring, J.-P., et al. (2006), Global mineralogical and aqueous mars history derived from OMEGA/Mars express data, *Science, 312*, 400–404, doi:10.1126/science.1122659.

Bishop, J. L., et al. (2008), Phyllosilicate diversity and past aqueous activity revealed at Mawrth Vallis, Mars, *Science, 321*, 830–833, doi:10.1126/science.1159699.

Burr, D. M. (2010), Palaeoflood-generating mechanisms on Earth, Mars, and Titan, *Global Planet. Change, 70*, 5–13, doi:10.1016/j.gloplacha.2009.11.003.

Carr, M. H., and J. W. Head (2010), Geologic history of Mars, *Earth Planet. Sci. Lett., 294*, 185–203, doi:10.1016/j.epsl.2009.06.042.

Chojnacki, M., et al. (2011), Orbital observations of contemporary dune activity in Endeavor Crater, Meridiani Planum, Mars, *J. Geophys. Res., 116*, E00F19, doi:10.1029/2010JE003675.

Christensen, P. R., et al. (2003), Miniature thermal emission spectrometer for the Mars Exploration Rover, *J. Geophys. Res., 108*(E12), 8064, doi:10.1029/2003JE002117.

Christensen, P. R., et al. (2004), Mineralogy at Meridiani Planum from the Mini-TES experiment on the Opportunity Rover, *Science, 306*, 1733–1739, doi:10.1126/science.1104909.

Clark, B. C., et al. (2007), Evidence for montmorillonite or its compositional equivalent in Columbia Hills, Mars, *J. Geophys. Res., 112*, E06S01, doi:10.1029/2006JE002756.

Day, J. M. D., et al. (2006), Petrology and chemistry of MIL 03346 and its significance in understanding the petrogenesis of nakhlites on Mars, *Meteorit. Planet. Sci., 41*, 581–606, doi:10.1111/j.1945-5100.2006.tb00484.x.

Dreibus, G., et al. (2002), Chemistry and petrology of the most feldspathic shergottite: Dhofar 378, Meteorit. *Planet. Sci., 37*, A43.

Drube, L., et al. (2010), Magnetic and optical properties of airborne dust and settling rates of dust at the Phoenix landing site, *J. Geophys. Res., 115*, E00E23, doi:10.1029/2009JE003419.

Ehlmann, B. L., et al. (2009), Identification of hydrated silicate minerals on Mars using MRO-CRISM: Geologic context near Nili Fossae and implications for aqueous alteration, *J. Geophys. Res., 114*, E00D08, doi:10.1029/2009JE003339.

Elwood Madden, M. E., R. J. Bodnar, and J. D. Rimstidt (2004), Jarosite as an indicator of water-limited chemical weathering on Mars, *Nature, 431*, 821–823, doi:10.1038/nature02971.

Fedo, C. M., H. W. Nesbitt, and G. M. Young (1995), Unraveling the effects of potassium metasomatism in sedimentary rocks and paleosols, with implications for paleoweathering conditions and provenance, *Geology, 23*, 921–924, doi:10.1130/0091-7613(1995)023<0921:UTEOPM>2.3.CO;2.

Folk, R. L. (1981), *Petrology of Sedimentary Rocks*, Hemphill, Austin, Tex.

Gellert, R., et al. (2006), Alpha Particle X-ray Spectrometer (APXS): Results from Gusev Crater and calibration report, *J. Geophys. Res., 111*, E02S05, doi:10.1029/2005JE002555.

Gillet, P., et al. (2005), Petrology, geochemistry, and cosmic-ray exposure age of Iherzolitic shergottite Northwest Africa 1950, *Meteorit. Planet. Sci., 40*, 1175–1184, doi:10.1111/j.1945-5100.2005.tb00182.x.

Greeley, R., et al. (2004), Wind-related processes detected by the Spirit rover at Gusev Crater, Mars, *Science, 305*, 810–813, doi:10.1126/science.1100108.

Greeley, R., et al. (2006), Gusev Crater: Wind-related features and processes observed by the Mars Exploration Rover Spirit, *J. Geophys. Res., 111*, E02S09, doi:10.1029/2005JE002491.

Greeley, R., et al. (2008), Columbia Hills, Mars: Aeolian features seen from the ground and orbit, *J. Geophys. Res., 113*, E06S06, doi:10.1029/2007JE002971.

Hamilton, V. E., H. Y. McSween Jr., and B. Hapke (2005), Mineralogy of Martian atmospheric dust inferred from thermal infrared spectra of aerosols, *J. Geophys. Res., 110*, E12006, doi:10.1029/2005JE002501.

Hausrath, E. M., et al. (2008), Basalt weathering rates on Earth and the duration of liquid water on the plains of Gusev Crater, Mars, *Geology, 36*, 67–70, doi:10.1130/G24238A.1.

Herkenhoff, K. E., et al. (2003), Athena Microscopic Imager investigation, *J. Geophys. Res., 108*(E12), 8065, doi:10.1029/2003JE002076.

Hughes, M. G., J. B. Keene, and R. G. Joseph (2000), Hydraulic sorting of heavy-mineral grains by swash on a medium-sand beach, *J. Sediment. Res., 70*, 994–1004, doi:10.1306/112599700994.

Hurowitz, J. A., and S. M. McLennan (2007), A ~3.5 Ga record of water-limited, acidic weathering conditions on Mars, *Earth Planet. Sci. Lett., 260*, 432–443, doi:10.1016/j.epsl.2007.05.043.

Ikeda, Y., et al. (2006), Petrology of a new basaltic shergottite: Dhofar 378, *Antarct. Meteorite Res., 19*, 20–44.

Irvine, T. N., and W. R. A. Baragar (1971), A guide to the chemical classification of the common volcanic rocks, *Can. J. Earth Sci., 8*, 523–548, doi:10.1139/e71-055.

Jambon, A., et al. (2002), The basaltic shergottite Northwest Africa 856: Petrology and chemistry, *Meteorit. Planet. Sci., 37*, 1147–1164, doi:10.1111/j.1945-5100.2002.tb00885.x.

Jerolmack, D. J., et al. (2006), Spatial grain size sorting in eolian ripples and estimation of wind conditions on planetary surfaces: Application to Meridiani Planum, Mars, *J. Geophys. Res., 111*, E12S02, doi:10.1029/2005JE002544.

Karunatillake, S., McLennan, S., and Herkenhoff, K. (2010), Regional and grain size influence on the geochemistry of soil at Gusev Crater, Mars, *J. Geophys. Res., 115*, E00F04, doi:10.1029/2010JE003637.

King, P. L., and McLennan, S. M. (2010), Sulfur on Mars, *Elements, 6*, 107–112, doi:10.2113/gselements.6.2.107.

Klingelhöfer, M., et al. (2003), Athena MIMOS II Mossbauer spectrometer investigation, *J. Geophys. Res., 108*(E12), 8067, doi:10.1029/2003JE002138.

Klingelhöfer, M., et al. (2004), Jarosite and hematite at Meridiani Planum from Opportunity's Mossbauer spectrometer, *Science, 306*, 1740–1745, doi:10.1126/science.1104653.

Knauth, L. P., Burt, D. M., and Wohletz, K. H. (2005), Impact origin of sediments at the opportunity landing site on Mars, *Nature, 438*, 1123–1128, doi:10.1038/nature04383.

Kuno, H. (1968), *Differentiation of basalt magmas, in Basalts: The Poldervaart Treatise on Rocks of Basaltic Composition*, vol. 2, edited by H. H. Hess and A. Poldervaart, pp. 623–688, Intersci. Publ., New York.

Lin, Y., et al. (2008), Bulk chemical composition of lherzolitic shergottite Grove Mountains 99027-Constraints on the mantle of Mars, *Meteorit. Planet. Sci., 43*, 1179–1187, doi:10.1111/j.1945-5100.2008.tb01121.x.

Lodders, K. (1998), A survey of shergottite, nakhlite and chassigny meteorites whole-rock compositions, *Meteorit. Planet. Sci., 33*, A183–A190, doi:10.1111/j.1945-5100.1998.tb01331.x.

Madsen, M. B., et al. (2009), Overview of the magnetic properties experiments on the Mars Exploration Rovers, *J. Geophys. Res., 114*, E06S90, doi:10.1029/2008JE003098.

McGlynn, I. O., McSween, H. Y., and Fedo, C. M. (2008), Textural and chemical evidence of hydrodynamic sorting in sediments in Gusev Crater, *Lunar Planet. Sci., XXXIX*, Abstract 1332.

McGlynn, I. O., Fedo, C. M. and McSween, H. Y. (2011), Origin of basaltic soils at Gusev Crater, Mars, by aeolian modification of impact-generated sediment, *J. Geophys. Res., 116*, E00F22, doi:10.1029/2010JE003712.

McKeown, N. K., et al. (2009), Characterization of phyllosilicates observed in the central Mawrth Vallis region, Mars, their potential formational processes, and implications for past climate, *J. Geophys. Res., 114*, E00D10, doi:10.1029/2008JE003301.

McLennan, S. (2000), Chemical composition of Martian soil and rocks: Complex mixing and sedimentary transport, *Geophys. Res. Lett., 27*(9), 1335–1338, doi:10.1029/1999GL008432.

McLennan, S. M., et al. (2005), Provenance and diagenesis of the evaporite-bearing Burns Formation, Meridiani Planum, Mars, Earth Planet. Sci. Lett., 240, 95–121, doi:10.1016/j.epsl.2005.09.041.

McSween, H. Y., and Keil, K. (2000), Mixing relationships in the Martian regolith and the composition of globally homogeneous dust, *Geochim. Cosmochim. Acta, 64*, 2155–2166, doi:10.1016/S0016-7037(99)00401-9.

McSween, H. Y., et al. (2006), Alkaline volcanic rocks from the Columbia Hills, Gusev Crater, Mars, *J. Geophys. Res., 111*, E09S91, doi:10.1029/2006JE002698.

McSween, H. Y., et al. (2008), Mineralogy of volcanic rocks in Gusev Crater, Mars: Reconciling Mössbauer, Alpha Particle X-Ray Spectrometer, and Miniature Thermal Emission Spectrometer spectra, *J. Geophys. Res., 113*, E06S04, doi:10.1029/2007JE002970.

McSween, H. Y., G. J. Taylor, and M. B. Wyatt (2009), Elemental composition of the Martian crust, *Science, 324*, 736–739, doi:10.1126/science.1165871.

McSween, H. Y., I. O. McGlynn, and A. D. Rogers (2010), Determining the modal mineralogy of Martian soils, *J. Geophys. Res., 115*, E00F12, doi:10.1029/2010JE003582.

Ming, D. W., et al. (2008), Geochemical properties of rocks and soils in Gusev Crater, Mars: Results of the Alpha Particle X-Ray Spectrometer from Cumberland Ridge to Home Plate, *J. Geophys. Res., 113*, E12S39, doi:10.1029/2008JE003195.

Morris, R. V., et al. (2006a), Mössbauer mineralogy of rock, soil, and dust at Gusev Crater, Mars: Spirit's journey through weakly altered olivine basalt on the plains and pervasively altered basalt in the Columbia Hills, *J. Geophys. Res., 111*, E02S13, doi:10.1029/2005JE002584.

Morris, R. V., et al. (2006b), Mössbauer mineralogy of rock, soil, and dust at Meridiani Planum, Mars: Opportunity's journey across sulfate-rich outcrop, basaltic sand and dust, and hematite lag deposits, *J. Geophys. Res., 111*, E12S15, doi:10.1029/2006JE002791.

Morris, R. V., et al. (2008), Iron mineralogy and aqueous alteration from Husband Hill through Home Plate at Gusev Crater, Mars: Results from the Mössbauer instrument on the Spirit Mars Exploration Rover, *J. Geophys. Res., 113*, E12S42, doi:10.1029/2008JE003201.

Nesbitt, H. W., and G. Markovics (1997), Weathering of granodioritic crust, long-term storage of elements in weathering profiles, and petrogenesis of siliciclastic sediments, *Geochim. Cosmochim. Acta, 61*, 1653–1670, doi:10.1016/S0016-7037(97)00031-8.

Nesbitt, H. W., and R. E. Wilson (1992), Recent chemical weathering of basalts, *Am. J. Sci., 292*, 740–777, doi:10.2475/ajs.292.10.740.

Nesbitt, H. W., and G. M. Young (1989), Formation and diagenesis of weathering profiles, *J. Geol., 97*, 129–147, doi:10.1086/629290.

Nesbitt, H. W., and G. M. Young (1996), Petrogenesis of sediments in the absence of chemical weathering: Effects of abrasion and sorting on bulk composition and mineralogy, *Sedimentology, 43*, 341–358, doi:10.1046/j.1365-3091.1996.d01-12.x.

Nesbitt, H. W., et al. (1996), Effects of chemical weathering and sorting on the petrogenesis of siliciclastic sediments, with implications for provenance studies, *J. Geol., 140*, 525–542.

Parteli, E. J. R., et al. (2009), Sand transport on Mars, *Comput. Phys. Commun., 180*, 609–611, doi:10.1016/j.cpc.2008.12.024.

Rieder, R., et al. (2003), The new Athena alpha particle X-ray spectrometer for the Mars Exploration Rovers, *J. Geophys. Res., 108*(E12), 8066, doi:10.1029/2003JE002150.

Rieder, R., et al. (2004), Chemistry of rocks and soils at Meridiani Planum from the alpha particle X-ray spectrometer, *Science, 306*, 1746–1749, doi:10.1126/science.1104358.

Rogers, A. D., and O. Aharonson (2008), Mineralogical composition of sands in Meridiani Planum determined from MER data and comparison to orbital measurements, *J. Geophys. Res., 113,* E06S14, doi:10.1029/2007JE002995.

Rubin, A. E., et al. (2000), Los Angeles: The most differentiated basaltic Martian meteorite, *Geology, 28*, 1011–1014, doi:10.1130/0091-7613(2000)28<1011:LATMDB>2.0.CO;2.

Sarbadhikari, A. B., et al. (2009), Petrogenesis of olivine-phyric shergottite Larkman Nunatak 06319: Implications for enriched components in Martian basalts, *Geochim. Cosmochim. Acta, 73*, 2190–2214, doi:10.1016/j.gca.2009.01.012.

Schmidt, M. E., et al. (2008), Hydrothermal origin of halogens at Home Plate, Gusev Crater, *J. Geophys. Res., 113*, E06S12, doi:10.1029/2007JE003027.

Shirai, N., and Ebihara,, M. (2004), Chemical characteristics of a Martian meteorite, Yamato 980459, *Antarct. Meteorite Res., 17*, 55–67.

Squyres, S. W., and Kasting, J. F. (1994), Early Mars: How warm and how wet? *Science, 265*, 744–749, doi:10.1126/science.265.5173.744.

Squyres, S. W., et al. (2008), Detection of silica-rich deposits on Mars, *Science, 320*, 1063–1067, doi:10.1126/science.1155429.

Sullivan, R., et al. (2005), Aeolian processes at the Mars Exploration Rover Meridiani Planum landing site, *Nature, 436*, 58–61, doi:10.1038/nature03641.

Sullivan, R., et al. (2008), Wind-driven particle mobility on mars: Insights from Mars Exploration Rover observations at “El Dorado” and surroundings at Gusev Crater, *J. Geophys. Res., 113,* E06S07, doi:10.1029/2008JE003101.

Tomasko, M. G., et al. (1999), Properties of dust in the Martian atmosphere from the imager on Mars Pathfinder, *J. Geophys. Res., 104*(E4), 8987–9007, doi:10.1029/1998JE900016.

Tosca, N. J., et al. (2004), Acid-sulfate weathering of synthetic Martian basalt: The acid fog model revisited, *J. Geophys. Res., 109*, E05003, doi:10.1029/2003JE002218.

Tosca, N. J., et al. (2008), Fe oxidation processes at Meridiani Planum and implications for secondary Fe mineralogy on Mars, *J. Geophys. Res*., 113, E05005, doi:10.1029/2007JE003019.

Treiman, A. H., and Irving, A. J. (2008), Petrology of Martian meteorite Northwest Africa 998, *Meteorit. Planet. Sci., 43*, 829–854, doi:10.1111/j.1945-5100.2008.tb01085.x.

Yen, A. S., et al. (2005), An integrated view of the chemistry and mineralogy of Martian soils, *Nature, 436*, 49–54, doi:10.1038/nature03637.

Yen, A. S., et al. (2006), Nickel on Mars: Constraints on meteoritic material at the surface, *J. Geophys. Res., 111*, E12S11, doi:10.1029/2006JE002797.

Yen, A. S., et al. (2008), Hydrothermal processes at Gusev Crater: An evaluation of Paso Robles class soils, *J. Geophys. Res., 113*, E06S10, doi:10.1029/2007JE002978.

Young, G. M., and Nesbitt, H. W. (1998), Processes controlling the distribution of Ti and Al in weathering profiles, siliciclastic sediments and sedimentary rocks, *J. Sediment. Res., 68*, 448–455.

Appendix

Table 3.A-1. MODEL 1 Mineralogy estimates for Gusev Crater and Meridiani Planum soils.

Sol	Name	Ol	fo	Px	en	Plg	an	Mt	Cr	Ap	npOx	Hm	Ilm	(Mg,Ca) SO_4	(Na,K)Cl	Silica	Clays	TA
Gusev Crater Soil																		
A014	Gusev_Soil	14.5	48	20.9	50	36.0	42	1.3	0.5	2.2	4.9	0.4	0.0	6.6	0.8	8	4	25
A043	Track	15.7	48	19.8	50	38.1	41	1.7	0.6	2.0	3.3	1.2	0.0	5.0	0.6	8	4	22
A047	Grandeflats																	
A049	Road Cut_Floor3_																	
A050	Road Cut_WallMIonl	15.3	38	18.8	40	36.2	37	2.3	0.5	2.0	4.8	0.9	0.0	6.3	0.7	8	4	25
A071	Gobi1_soil	16.5	46	22.4	48	34.4	47	2.1	0.7	1.7	3.3	0.2	0.0	6.1	0.7	8	4	22
A074A	BearPaw	15.9	46	21.9	48	36.0	45	1.8	0.6	1.8	3.2	0.2	0.0	5.7	0.8	8	4	22
A105	Bitterrootflats_flats1																	
A113	Bighole_Mayfly_surface	16.7	47	23.2	49	33.1	52	2.9	0.7	0.4	3.0	0.7	0.0	6.6	0.8	8	4	23
A114	Bighole_RS2	14.6	57	16.5	59	37.0	37	4.9	0.5	2.0	5.2	0.0	0.0	6.7	0.7	8	4	25
A122	Owens_soil_Track	16.9	47	17.3	49	37.7	37	2.4	0.6	2.2	3.7	0.0	0.0	6.4	0.8	8	4	23
A140	Boroughs_Mills_bottom																	
A141	Boroughs_Hellskitchen_side	13.2	54	19.1	56	40.0	39	2.2	0.5	2.3	4.3	0.4	0.0	5.4	0.6	8	4	23
A158	Shredded_dark4_soil																	
A167	Goldfinger_Jaws_soil																	
A259	Disturbance_soil	13.4	48	21.2	50	42.4	38	1.1	0.5	1.8	2.8	0.2	0.0	4.1	0.5	8	4	20
A280	Coffee_disturbed_soil	15.3	52	19.8	54	39.2	33	2.0	0.4	2.0	3.1	0.4	0.0	5.3	0.6	8	4	21
A342	Penny_dist_soil	13.7	50	18.7	53	39.0	36	1.6	0.5	2.2	4.6	0.4	0.0	6.6	0.8	8	4	24
A457	Crumble	12.2	51	20.9	53	37.8	36	2.5	0.5	2.5	3.8	0.4	0.0	6.5	0.9	8	4	24
A477	Bell	14.4	49	19.8	52	41.3	33	1.6	0.5	2.1	2.6	0.3	0.0	4.8	0.6	8	4	20
A502	Pequod_Doubloon_TG	15.6	50	16.5	52	43.4	38	1.5	0.3	3.4	2.2	0.5	0.0	4.0	0.6	8	4	19
A587	Whymper	14.8	49	19.7	51	40.3	39	1.4	0.5	2.0	3.4	0.6	0.0	4.8	0.6	8	4	21
A607	LandsEnd																	
A611	HangTwo																	
A709	ElDorado_Scuff_Shadow	9.0	55	20.4	57	43.5	36	1.5	0.4	2.7	3.8	0.5	0.3	5.3	0.6	8	4	22
A814	Mawson																	
A823	Progress	14.0	52	25.6	55	39.6	39	1.8	0.5	1.9	1.1	0.0	0.0	3.1	0.4	8	4	17
A831	Progress 1 brushed	15.2	49	20.5	51	39.2	38	1.4	0.5	2.1	2.7	1.3	0.0	4.5	0.6	8	4	21
A847	Progress 2 brushed	13.9	49	20.4	51	38.1	41	1.5	0.5	2.4	4.4	0.6	0.0	5.5	0.6	8	4	23
A1013	Berkner Island 1	15.3	47	18.6	50	38.2	42	1.5	0.5	2.4	4.1	0.8	0.0	5.8	0.7	8	4	23
A1017	Bear_Island	13.5	50	19.8	52	40.5	34	1.2	0.5	2.2	3.6	0.7	0.0	5.4	0.6	8	4	22
A1246	Eastern Valley Eileen Dean_Eileen Dean 2																	

Table 3.A-1. (continued)

Sol	Name	Ol	fo	Px	en	Plg	an	Mt	Cr	Ap	npOx	Hm	Ilm	$(Mg,Ca)SO_4$	(Na,K)Cl	Silica	Clays	TA
Meridiani Planum Soil																		
B011	Tarmac	16.8	39	23.7	41	30.3	57	1.6	0.7	2.0	3.4	0.9	0.0	5.0	0.6	10	5	25
B023	Hematite_Slope_Hema2	14.5	42	22.3	45	29.3	48	1.7	0.5	2.0	3.5	5.7	0.0	4.8	0.7	10	5	30
B025	Trench_floor																	
B026	Trench_sidewall	14.2	42	23.2	45	30.3	53	1.3	0.7	1.8	5.4	1.7	0.0	5.7	0.6	10	5	28
B060	MontBlanc_LeHauches																	
B080	JackRussel_SoilBesi																	
B090	Scuff_Nougat	12.6	51	21.4	54	32.6	45	1.6	0.7	2.1	5.0	2.5	0.0	5.8	0.6	10	5	29
B091	Fred_Ripple_soil																	
B100	Leahs_Choice																	
B123	HillTop_Wilson	13.7	41	21.0	44	32.6	47	1.9	0.6	2.2	4.3	0.9	0.0	7.1	0.8	10	5	28
B166	Soil_Millstone_Dahlia	14.2	38	22.7	41	35.0	48	1.1	0.5	2.0	3.0	0.6	0.0	5.2	0.6	10	5	24
B237	Auk_RAT	14.1	39	22.6	41	36.2	49	1.3	0.4	2.0	2.9	0.2	0.0	4.6	0.6	10	5	23
B249	Rocknest_void_soil	15.3	39	23.2	42	33.5	46	1.6	0.7	2.1	2.8	0.6	0.0	4.6	0.6	10	5	24
B368	Left_of_peanut_TrenchFloor	13.3	37	22.8	39	31.8	46	1.8	0.7	2.1	4.6	0.9	0.0	6.6	0.5	10	5	28
B373	Scuff_Srcuffy	11.8	35	26.6	37	31.5	49	1.7	0.7	2.2	3.0	0.9	0.0	6.1	0.5	10	5	25
B420	RippleCrest_NoRooz																	
B420	RippleCrest_MayNoRooz																	
B443	Recovery_Cure																	
B507	Purgatory_Track2																	

Mineral abreviations are Ol, olivine; Px, pyroxene; Plg, plagioclase; Mt, magnetite; Cr, chromite; Ap, apatite; npOx, nanophase ferric oxide, Hm, hematite; and Ilm, ilmenite. Clays are modeled to represent a 1:1 ratio of montmorilonite and beidellite. TA (Total Alteration) is the sum of all alteration components (nanophase ferric oxides, hematite, sulfates, chlorides, silica, and clays).

Table 3.A-2. MODEL 2 Mineralogy estimates for Gusev Crater and Meridiani Planum soils.

Sol	Name	Ol	fo	Px	en	Plg	an	Mt	Cr	Ap	npOx	(Sh)	(Ak)	Hm	Ilm	Silica	Clays	TA
Gusev Crater Soil																		
A014	Gusev_Soil	10.3	53	30.7	56	39.5	35	0.9	0.5	2.2	3.7	2.5	1.2	0.3	0.0	8	4	16
A043	Track	12.3	52	29.9	54	38.1	38	1.3	0.6	2.0	2.8	1.9	0.9	0.9	0.0	8	4	16
A047	Grandeflats	14.2	43	33.8	46	29.7	40	2.0	0.5	2.1	4.9	3.3	1.6	0.8	0.0	8	4	18
A049	Road Cut_Floor3_	12.1	51	30.8	53	38.4	40	1.5	0.7	1.7	2.7	1.8	0.9	0.1	0.0	8	4	15
A050	Road Cut_WallMIonl	11.6	50	32.4	53	37.5	39	1.2	0.6	1.9	2.6	1.7	0.9	0.1	0.0	8	4	15
A071	Gobi1_soil	9.9	57	32.1	60	37.3	33	1.0	0.5	2.3	4.5	3.0	1.5	0.3	0.0	8	4	17
A074A	BearPaw	12.4	52	33.8	54	35.8	44	2.0	0.7	0.4	2.4	1.6	0.8	0.5	0.0	8	4	15
A105	Bitterrootflats_flats1	11.7	62	27.1	64	38.9	31	3.5	0.5	2.0	4.3	2.9	1.4	0.0	0.0	8	4	16
A113	Bighole_Mayfly_surface	13.9	52	29.4	54	36.7	33	1.8	0.6	2.3	3.3	2.2	1.1	0.0	0.0	8	4	15
A114	Bighole_RS2	11.4	66	28.6	68	37.8	35	1.2	0.6	2.1	6.1	4.1	2.0	0.1	0.0	8	4	18
A122	Owens_soil_Track	9.8	58	29.0	61	41.3	35	1.5	0.5	2.4	3.4	2.3	1.1	0.2	0.0	8	4	16
A140	Boroughs_Mills_bottom	11.8	60	36.6	62	30.0	42	1.3	0.6	1.9	5.3	3.6	1.8	0.3	0.0	8	4	18
A141	Boroughs_Hellskitchen_side	12.4	68	41.2	70	23.9	43	1.4	0.7	2.2	6.0	4.0	2.0	0.1	0.0	8	4	18
A158	Shredded_dark4_soil	11.2	51	32.1	54	38.6	40	0.9	0.5	1.9	2.6	1.7	0.9	0.1	0.0	8	4	15
A167	Goldfinger_Jaws_soil	13.7	55	33.9	58	33.0	35	1.6	0.4	2.0	3.1	2.0	1.0	0.3	0.0	8	4	15
A259	Disturbance_soil	10.9	56	31.0	58	38.0	33	1.2	0.5	2.3	3.9	2.6	1.3	0.3	0.0	8	4	16
A280	Coffee_disturbed_soil	10.2	56	35.9	58	33.2	35	1.9	0.5	2.6	3.4	2.3	1.1	0.3	0.0	8	4	16
A342	Penny_dist_soil	14.3	53	33.2	55	33.3	38	1.5	0.5	2.1	2.8	1.9	0.9	0.3	0.0	8	4	15
A457	Crumble	12.8	53	27.8	55	40.0	40	1.1	0.4	3.4	2.0	1.4	0.7	0.4	0.0	8	4	14
A477	Bell	11.4	53	29.6	55	40.1	36	1.0	0.5	2.1	2.9	1.9	1.0	0.4	0.0	8	4	15
A502	Pequod_Doubloon_TG	11.8	69	17.9	71	44.3	47	0.8	0.3	5.5	3.6	2.4	1.2	1.6	2.1	8	4	17
A587	Whymper	9.2	67	30.8	69	38.9	30	1.0	0.4	2.4	4.7	3.2	1.6	0.5	0.0	8	4	17
A607	LandsEnd	6.7	59	31.9	62	41.7	35	1.0	0.4	2.8	3.0	2.0	1.0	0.3	0.2	8	4	15
A611	HangTwo	2.9	74	25.2	76	51.1	33	0.5	0.2	5.3	2.2	1.5	0.7	0.5	0.0	8	4	15
A709	ElDorado_Scuff_Shadow	16.6	54	32.9	56	32.6	46	2.0	0.5	2.0	1.5	1.0	0.5	0.0	0.0	8	4	13
A814	Mawson	12.5	52	31.5	54	36.7	38	1.1	0.6	2.2	2.4	1.6	0.8	1.0	0.0	8	4	15
A823	Progress	9.8	53	29.0	56	41.5	35	1.0	0.5	2.4	3.4	2.2	1.1	0.4	0.0	8	4	16
A831	Progress 1 brushed	11.3	52	27.1	55	41.7	35	1.0	0.5	2.5	3.3	2.2	1.1	0.5	0.0	8	4	16
A847	Progress 2 brushed	11.5	54	32.6	57	36.3	35	0.9	0.5	2.3	3.3	2.2	1.1	0.6	0.0	8	4	16
A1013	Berkner Island 1	12.8	76	43.4	78	24.9	35	0.0	0.8	2.8	1.6	1.0	0.5	1.7	0.0	8	4	15
A1017	Bear_Island	11.6	55	34.8	57	34.7	38	1.2	0.5	2.2	2.7	1.8	0.9	0.4	0.0	8	4	15
A1246	Eastern Valley Eileen Dean_Eileen Dean 2	16.2	79	29.8	80	25.7	33	9.3	0.8	1.7	2.9	1.9	1.0	1.0	0.7	8	4	16

Table 3.A-2. (continued)

Sol	Name	Ol	fo	Px	en	Plg	an	Mt	Cr	Ap	npOx	(Sh)	(Ak)	Hm	Ilm	Silica	Clays	TA
Meridiani Planum Soil																		
B011	Tarmac	12.3	43	32.2	45	33.4	49	1.1	0.7	2.1	2.8	1.8	0.9	0.6	0.0	10	5	18
B023	Hematite_Slope_Hema2	11.8	47	34.4	49	27.4	47	1.3	0.5	2.0	3.2	2.1	1.1	4.4	0.0	10	5	23
B025	Trench_floor	9.1	65	29.1	67	35.0	44	0.9	0.6	2.0	7.3	4.9	2.4	0.9	0.0	10	5	23
B026	Trench_sidewall	11.1	48	31.2	50	33.4	46	0.9	0.7	1.9	4.6	3.1	1.5	1.2	0.0	10	5	21
B060	MontBlanc_LeHauches	9.6	56	29.6	59	36.1	40	0.8	0.5	2.4	5.2	3.5	1.7	0.7	0.0	10	5	21
B080	JackRussel_SoilBesi	9.8	80	36.1	81	28.5	33	0.0	0.5	1.9	1.3	0.9	0.4	6.9	0.0	10	5	23
B090	Scuff_Nougat	9.2	57	31.2	59	35.0	39	1.1	0.7	2.2	3.9	2.6	1.3	1.7	0.0	10	5	21
B091	Fred_Ripple_soil	9.7	88	37.9	89	29.1	30	0.6	0.4	2.1	0.9	0.6	0.3	4.2	0.0	10	5	20
B100	Leahs_Choice	9.2	78	35.8	79	28.5	31	0.7	0.4	2.1	2.1	1.4	0.7	6.2	0.0	10	5	23
B123	HillTop_Wilson	11.0	48	33.8	50	31.7	43	1.4	0.6	2.2	3.7	2.4	1.2	0.6	0.0	10	5	19
B166	Soil_Millstone_Dahlia	11.2	43	32.7	45	34.7	45	0.8	0.5	2.0	2.6	1.7	0.9	0.5	0.0	10	5	18
B237	Auk_RAT	10.3	43	30.1	46	38.6	43	0.9	0.4	2.1	2.4	1.6	0.8	0.1	0.0	10	5	18
B249	Rocknest_void_soil	13.3	43	34.0	46	30.4	47	1.3	0.7	2.1	2.7	1.8	0.9	0.5	0.0	10	5	18
B368	Left_of_peanut_TrenchFloor	10.7	43	35.3	46	30.1	46	1.3	0.7	2.1	4.0	2.7	1.3	0.7	0.0	10	5	20
B373	Scuff_Srcuffy	8.8	41	37.9	43	31.0	47	1.2	0.7	2.2	2.5	1.6	0.8	0.6	0.0	10	5	18
B420	RippleCrest_NoRooz	12.0	85	32.4	86	30.3	34	0.0	0.4	2.2	1.5	1.0	0.5	6.1	0.0	10	5	23
B420	RippleCrest_MayNoRooz	11.4	88	34.6	89	30.4	32	0.0	0.4	2.1	1.2	0.8	0.4	4.9	0.0	10	5	21
B443	Recovery_Cure	11.8	77	30.3	79	30.0	36	0.5	0.5	2.1	2.1	1.4	0.7	7.7	0.0	10	5	25
B507	Purgatory_Track2	9.4	62	29.3	64	34.2	39	0.9	0.6	2.4	5.8	3.9	1.9	2.4	0.0	10	5	23

Mineral abreviations are Ol, olivine; Px, pyroxene; Plg, plagioclase; Mt, magnetite; Cr, chromite; Ap, apatite; npOx, nanophase ferric oxide (modelled as a 2:1 ratio of Sh, schwertmannite and Ak, akaganeite), Hm, hematite; and Ilm, ilmenite. Clays are modeled to represent a 1:1 ratio of montmorilonite and beidellite. TA (Total Alteration) is the sum of all alteration components (nanophase ferric oxides, hematite, sulfates, chlorides, silica, and clays).

Chapter 4

Grain size and hydrodynamic sorting controls on synthetic basaltic sediments: Implications for interpreting martian soils

A version of this chapter to be submitted to Earth and Planetary Science Letters

Abstract

Impact shattering of bedrock, wind-driven transport, and sorting have been identified as the primary processes modifying the size, shape, and roundness of basalt-derived sediment "soils" at the Spirit rover landing site in Gusev Crater, Mars. Here we experimentally explore how hydrodynamic sorting can cause significant compositional modification. Two basalt samples, chosen to provide a range of source rock compositions and igneous textures, were crushed and sieved. We quantify the variations sediment mineral proportions as a function of grain size, as well as the accompanying changes in major- and trace-element geochemistry that result from sieving. Redistribution of phenocrysts imposes the primary compositional control on basalt-derived sediments, although minor mineral fractionations affect trace-element concentrations. Major- and trace-element compositions diverge from expected source rock values. Olivine accumulation is paired with MgO, Fe_2O_3(T), Ni, and Co, and Al_2O_3 depletion. Trace-elements are strongly controlled by accessory minerals. The observed chemical changes in physically sorted sediments in our experiments mimic those measured in Martian soils and previously attributed to chemical weathering. Aeolian transport models demonstrate that sorting of mineral components of basalts under Martian conditions is likely. Given the potential for sorting by winds on Mars we argue that sorting must be considered, in addition to source rock and chemical weathering, when interpreting the geochemistry of Mars sediments.

1. Introduction

Interpretations of sediment compositions on Mars commonly focus on the abundance of olivine to identify local source rocks [Mangold et al., 2007; Stockstill-Cahill et al., 2009] or as an indication of the extent of chemical weathering of basalt [*e.g.,* Koeppen and Hamilton, 2008]. However, low *chemical index of alteration* [CIA; Nesbitt and Young, 1982] values for sediment at the Mars Pathfinder [McSween and Keil, 2000] and Mars Exploration Rovers [MER; Hurowitz and McLennan, 2007] landing sites indicate limited hydrolysis and clay production from phases such as plagioclase and volcanic glass. Clay and sulfate minerals present at the MER landing sites of Gusev Crater and Meridiani Planum most likely represent physical admixtures of material [McSween et al., 2010; McGlynn et al., 2012] that formed during earlier, perhaps wetter, sedimentary cycles.

Several factors control how sediments acquire their compositions from bedrock sources. Based on the removal of labile cations during hydrolysis, chemical weathering largely controls the composition of weathered terrestrial basalt [Nesbitt and Wilson, 1992] and synthetic basalt analogs [Tosca et al., 2004]. However, changes in sediment mineral composition, indicating olivine abundance, may also reflect initial variability in source rocks, and hydrodynamic sorting can impose compositional changes in active terrestrial transport environments [Nesbitt et al., 1996; Fralick, 2003] including basalt-derived sediment [Mangold et al., 2011]. *Hydrodynamic sorting*, or the separation of minerals by transport [*e.g.* Rieu et al., 2007], will be referred to as *sorting* throughout the paper. Sorted sedimentary particles occur on the martian surface in the form of dunes [Greeley et al., 2008], including presently active dunes [Bridges et al., 2012], in

small dunes or complex ripples [Greeley et al., 20006a], and in ripples [Sullivan et al., 2005, 2008]. Therefore compositional changes derived from purely physical processes must be considered when interpreting the sedimentary petrology [*e.g.* Mangold et al., 2011; McGlynn et al., 2012].

Continued lack of evidence for abundant chemical weathering coupled with a growing interest in the important, even dominant, role for physical processes in the formation of sediment on the Martian landscape [*e.g.*, Knauth, 2005; Grotzinger et al., 2011; McGlynn et al., 2011, 2012] leads us to consider how we might address the extent to which it shaped sediment mineralogy and geochemistry. This paper uses experiments to explore whether compositional variations occur from the range of sieved grain-size populations from two texturally and compositionally different crushed basaltic bedrock analogs. The grain-size frequency distribution of impact-generated sediments on a planetary surface [King, 1977] should resemble the distribution of sediment generated in crushing experiments [Kittleman, 1964]. This experimental approach is not intended to simulate sorting of impact-generated sediment, but instead provides a demonstration of concept for compositional controls resulting from the redistribution of mineral grains. Further, using relevant rocks and minerals with a range of densities, we model initial threshold velocity (u_{*t}) and grain-size relationships in order to demonstrate that, even in the complete absence of hydrolysis, significant chemical changes in sediment may result from the redistribution of mineral species by sorting. The experiment and modeling investigate the extent to which physical fractionations in artificially crushed and sieved sediments mimic impact shattering of bedrock followed by aeolian transport of sediment on Mars and account for its

surface composition, a combined set of processes that have strongly shaped the martian surface [McGlynn et al., 2011; 2012].

2. Importance of Sorting on Sediment Compositions

When physical processes outpace chemical processes, transport effects, principally through sorting, are capable of modifying the composition of terrestrial sediments to varying degrees. Physical breakdown of bedrock alone is insufficient to impose compositional changes on the resultant sediments [Kuenen, 1964], which indicates that additional processes leading to mineral segregation must be operative. In such conditions, elemental fractionation can be significant. Sorting effects have been described in sediment generated from glacial abrasion in the Guys Bight Basin of Baffin Island, in Arctic Canada [Nesbitt and Young, 1996], where there is a general absence of chemical weathering due to low temperatures and short transport distances. Glacially comminuted sediment, derived from feldspar-quartz-biotite gneiss, underwent sorting during fluvial transport from glaciers to the ocean. The resulting sediment compositions exhibited concentration of quartz and feldspars in coarse sands, and a relative increase in abundance of biotite, garnet, and hornblende in fine sands and muds, although in this case, chemical weathering of feldspars was present but minimal. Considerable variation in bulk sediment TiO_2 concentrations was identified, with the abrasion and separation of biotite concentrated in finer-grained samples [Young and Nesbitt, 1998].

Size separations of lunar mare [Taylor et al., 2001] and highlands [Taylor et al., 2010] samples have produced considerable variations in soil mineralogy and chemistry relative to bulk chemistry. Decreasing grain size produces an increase in plagioclase abundance and with concomitant increase in CaO and Al_2O_3, and decreases in pyroxene and olivine reflected in lower FeO and MgO. Additionally, nanophase iron concentrates in agglutinate glass in < 10 μm fractions [Taylor et al., 2010]. Agglutinates have not been observed in martian soil, although clay- and silt-sized grains cannot be examined in MER soils due to the MI resolution. However, a similar approach is relevant for the characterization of soils on Mars. Given the potential for aeolian transport effects on Mars, considerable compositional changes from the mineral separation of soils is expected.

In addition to sorting of primary minerals, accessory mineral sorting has also been investigated. Case studies from Fralick [2003] documented geochemical differences from heavy mineral separation controlled by grain size, shape, specific gravity, and flow conditions in Matinenda Formation placer deposits, where smaller dense grains resist erosion compared to light mineral grains. Preferential segregation of accessory minerals was reported with increasing distance from the sedimentary source.

Aeolian transported, minimally altered volcanic sand from the Eldborgir shield volcano, Iceland, provides a basaltic comparison for mineral segregation [Baratoux et al., 2011]. The prevailing wind direction concentrated sand enriched in Mg and Ni from an increased proportion of olivine grains relative to the source rocks, but the sand is depleted in Ba, Ce, Dy, Er, Eu, Hf, La, Nb, Nd,

Pr, Sr, Sm, Zn, and Zr [Mangold et al., 2011]. Results are complicated by potential mixing from multiple sources.

Controlled mineral separation experiments are needed to reduce the variability inherent in such investigations. Prior attempts to identify the effects of sorting on Mars have focused on chemically immobile elements that will maintain invariant ratios during rock mass change caused by either addition or depletion of mobile elements. Ratios of Fe:Ti in Viking, Pathfinder [McSween and Kiel, 2000; McLennan, 2000], and MER [McGlynn et al., 2008] sediment results indicated the possibility of aeolian-driven mineral fractionation, where separation of dense accessory phases, including ilmenite, titanomagnetite, magnetite, and chromite from less dense phases might be expected in mafic sediments. The compositions of sediments in Gusev Crater are, in part, controlled by mixing materials from multiple bedrock sources and by the selective sorting of dense ferromagnesian minerals (olivine or pyroxene) from basaltic lithic fragments [McGlynn et al., 2012]. As bolide impacts and aeolian sandblasting comminute basaltic bedrock, individual minerals, especially those occurring as phenocrysts, can be isolated from the source rock. Sorting then has the potential to selectively winnow or concentrate minerals, and thereby modify sediment compositions.

3. Physical Weathering and Dynamic Sediment Transport on Mars

Sediment transport must occur to drive sorting. The surface of Mars is an aeolian-dominated landscape, with aeolian features including ripples and dunes observed at the MER landing sites [Greeley et al., 2004; Sullivan et al., 2005, 2008] and elsewhere [*e.g.,* Cutts and Smith, 1973;

Bridges et al., 2007; Balme et al., 2008; Zimbelman, 2010]. Ventifacts were described at the Mars Pathfinder site [Greeley et al., 1999]. Despite the presence of aeolian landscapes, direct observations of wind-blown transport are limited. Entrainment and movement of silt-sized grains (<100 μm) were observed at the Pathfinder [Smith and Lemmon, 1999] and Phoenix [Ellehoj et al., 2010] landing sites, and cameras on the Spirit rover in Gusev Crater captured images of dust devil tracks [Greeley et al., 2004] and active dust devils [Greeley et al., 2006a, b, 2010]. While dust is easily entrained and suspended on a local and global scale on Mars, the magnitude and frequency of aeolian processes capable of transporting sand-sized sediment is not well constrained.

The lack of observed sediment mobility during the extended Viking and MER missions [Greeley et al., 2004], and modeling of sediment entrainment using the low atmospheric pressure conditions [Greeley et al., 1993] suggested that the transport of sand-sized sediment may be a rare event. However, the El Dorado ripple field in Gusev Crater demonstrates that aeolian transport was once active [Sullivan et al., 2008], and models predict that when saltation of sand-sized sediment is initiated, transport may be easily sustained [Kok, 2010]. Recent observations of active sand dunes [Silvesto et al., 2010; Hansen et al., 2011; Chojnacki et al., 2011] dispersed globally [Bridges et al., 2012] demonstrate that the movement of sand occurs, offering a viable mechanism for sediment sorting and mineral fractionation on Mars.

4. Rationale and Design for Experiments

4.1. Basaltic Bedrock

Global surface compositions analyzed by the Mars Odyssey Gamma Ray Spectrometer [Taylor et al., 2006] point to a basaltic composition for the crust of Mars [McSween et al., 2009]. Rocks examined by the Spirit rover at the Gusev Crater landing site consist olivine-rich basalts and related trachybasalts and tephrites [McSween et al., 2004, 2006a, b, 2008], and martian (SNC) meteorites are basalts and related ultramafic rocks [McSween et al., 2003]. Most sediment "soils" in Gusev Crater and Meridiani Planum analyzed by the MER Alpha Particle X-ray Spectrometer (APXS) have chemical compositions [McSween et al., 2010; McGlynn et al. 2012] indicating basalt-derived sources. In this light, we have selected two basalts with varying textures and compositions, one from the Cima volcanic field, Mojave Desert, CA and the other from Kilauea, HI to conduct this study. Details of each are described in section 5.

4.2. Physical Comminution and Sieving

Bedrock pulverized by impacts on the surface of a planet [King, 1977] produces sediment with a Rosin grain-size distribution similar to what is generated from comminution experiments [Kittleman, 1964]. In this study, two basalt samples were broken into cobble-sized clasts with a rock press, and then pulverized using a WD Chipmunk Crusher. Sediments generated from each basalt sample were sieved into 14 grain-size fractions using conventional dry sieving procedure [*e.g.* Friedman and Johnson, 1982; Lewis, 1984; McManus, 1988] with a Tyler Ro-Tap RX-29 for 30 minutes at 0.5 ϕ fractions from -2.0 to 4.0 ϕ (4 to 1/16 mm; 4,000 to 62 μm). Sediments retained at -2.0 ϕ were manually sieved into -2.0, -2.5, and -3.0 ϕ fractions. Constrains in the

crushing procedure limits the production of boulder- and cobble-sized grains expected from impacts, resulting in coarse-skewed sediment. Additionally, once the particle size significantly exceeds the grain size of phenocrysts in the protolith, then the composition of sediment cannot change relative to the source.

Material retained at each successive sieve was recorded, and mass loss from sieving was < 0.5% for each sample (Table 4.A-1; all tables in Appendix). Resultant grain-size fractions compare to those observed in images taken by the MER Microscopic Imager (MI), with examples provided in McGlynn et al. [2011]. Sediments finer than 4.0 ϕ lie outside MI resolution and were not further subdivided, even though that fraction is not likely to be homogeneous as seen in lunar soils [Taylor et al., 2001, 2010].

4.3. Petrographic and Geochemical Analysis

The modal mineralogies of Cima and Kilauea bedrock and sieved sediment samples were determined using the Gazzi-Dickinson point counting method [Dickinson, 1970; Ingersoll et al., 1984] on conventional 30 μm thin sections. Point counts of bedrock samples had 1000 points. Sediment samples were characterized by point counting with 500 counts and grains were classified into: (1) lithic fragments, (2) olivine, (3), plagioclase, (4), pyroxenes, (5) oxides, and (6) glass. Mineral compositions were determined using a Cameca SX-100 electron microprobe. Bedrock and synthetic sediment populations were powdered with a SPEX 8515 shatterbox using a ceramic dish and puck, then commercially analyzed by Inductively Coupled Plasma Spectrometry for major-, trace-, and rare earth element (REE) concentration by ACTLABS (4Lithoresearch package).

5. Basalt Source Rocks

5.1. Cima Trachybasalt

5.1.1. Mineralogy and Petrology

The first examined bedrock sample is a nearly aphyric trachybasalt (hawaiite), from the Cima volcanic field [Wells et al., 1985; Farmer et al., 1995], Mojave Desert, CA (Figure 4.1A-C). It contains rare phenocrysts of plagioclase, and microphenocrysts of olivine, plagioclase, and clinopyroxene (Figure 4.1B, C) set in a groundmass of olivine, clinopyroxene, plagioclase, and equant opaque minerals of chromite (Figure 4.1C). Plagioclase phenocrysts show a zonation from andesine (An_{40}) in the core to and labradorite (An_{60}) in the rim. Magnetite inclusions are common within pyroxene microphenocrysts. Olivine microphenocrysts are zoned with Mg-rich cores (Fo_{75} to Fo_{85}) and a gradual increase in iron content towards the grain rims (Fo_{68} to Fo_{73}). Pyroxene microphenocrysts are composed of augite (Wo_{45}, En_{43}) with minor increase in Ca-enrichment in the rims (Wo_{48}, En_{48}). Matrix minerals are distinct from the phenocryst/microphenocryst compositions, and composed of plagioclase (labradorite An_{54} to An_{62}), olivine (Fo_{65} to Fo_{74}), pyroxene (Wo_{45}, En_{36} to Wo_{49}, En_{40}), and oxides. Modal mineralogy is estimated as 35 % plagioclase, 34 % pyroxene, 16 % oxides, and 15 % olivine (Table 4.A-1).

5.1.2. Geochemistry

Geochemical results for Cima bedrock (Tables 4.A-2 to 4.A-4) provide a basis from which to compare deviations in sediment compositions. Cima trachybasalt contains high alkali

Figure 4.1. Images, photomicrographs, and backscatter electron (BSE) images of rocks used to generate sediments. (A) Aphyric to sparsely phyric Cima trachybasalt. (B) Vesicles and phenocrysts of plagioclase (pl), pyroxene (px), and olivine (ol) are visible in plain light photomicrograph. (C) BSE image of sparsely plagioclase-pyroxene phyric trachybasalt, with olivine-pyroxene-plagioclase matrix. (D) Vesicles and olivine phenocrysts in Kilauea basalt. (E) Photomicrograph of abundant olivine phenocrysts and vesicles in plain light. (F) BSE image of Kilauea basalt with olivine phenocrysts and plagioclase-pyroxene matrix.

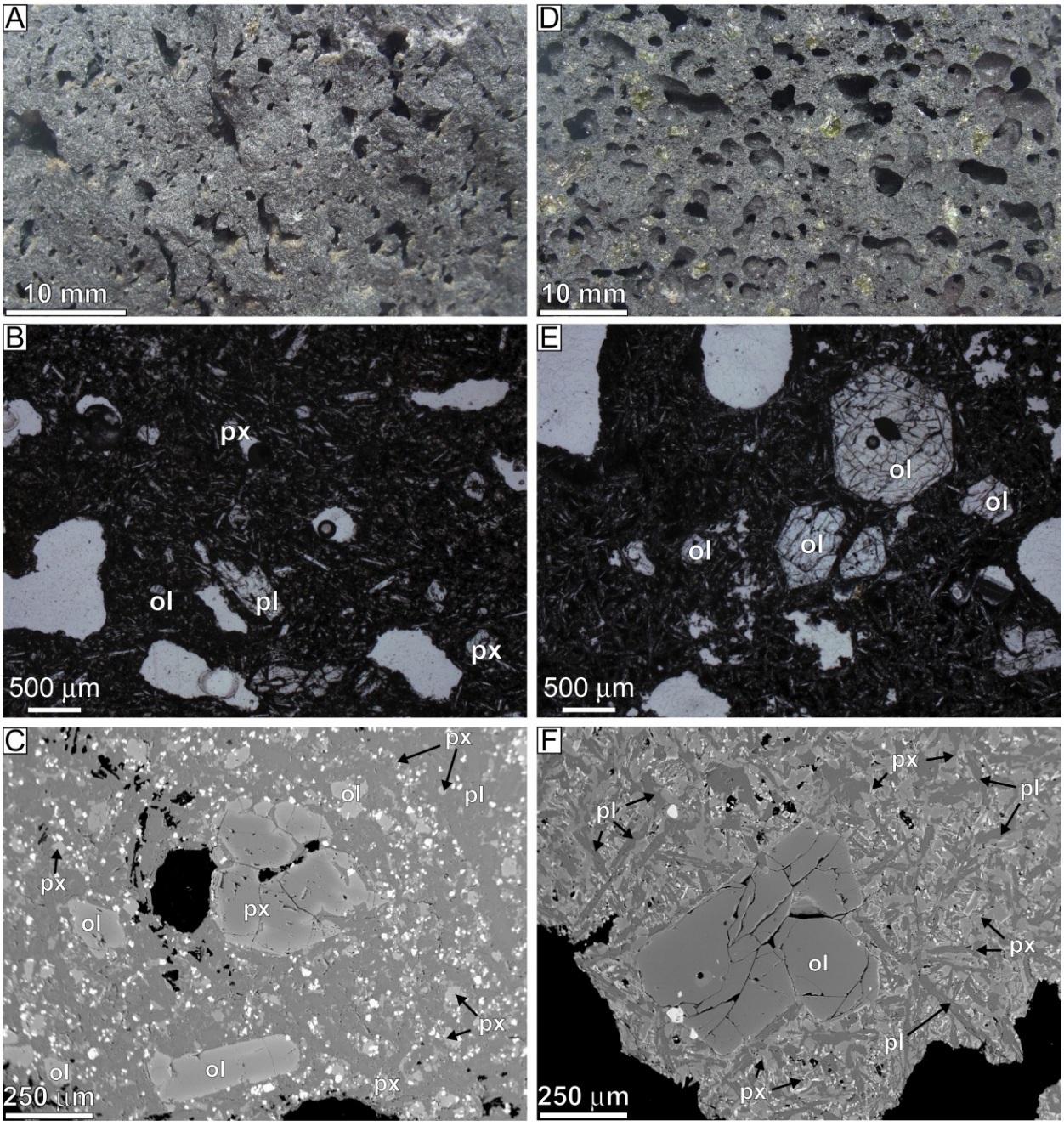
A
10 mm
D
10 mm
B
px
ol
pl
px
500 µm
E
ol
ol
ol
ol
500 µm
C
px
ol
pl
px
ol
px
px
ol
ol
px
250 µm
F
px
pl
pl
px
ol
pl
px
250 µm

components (Na_2O+K_2O) and contains moderate TiO_2 from secondary minerals (Figure 4.2A). Plagioclase controls Al_2O_3, Na_2O, and K_2O concentrations, whereas pyroxene and olivine control the concentrations of Fe_2O_3(T) and MgO. Silica abundance is comparable to rocks and soils on Mars [McSween et al., 2009]. Trace-element abundances (Figure 4.2B) are normalized to chondrite [McDonough and Sun, 1995] as a reference. Bedrock rare earth element (REE) results are light-REE enriched and show no Eu anomaly (Figure 4.2C), which are consistent with other findings in Cima [Farmer et al., 1995].

5.2. Kilauea Basalt

5.2.1. Mineralogy and Petrology

The second studied bedrock is a highly porphyritic vesicular basalt from Kilauea volcano, HI [*e.g.* Garcia et al., 2003], with abundant euhedral olivine phenocrysts and a groundmass of olivine, clinopyroxene, plagioclase, and equant opaque minerals (Figure 4.1D-F). Olivine phenocrysts and microphenocrysts are magnesium-rich (Fo_{84} to Fo_{87}) and are slightly zoned with minor iron enrichment in the rims (Fo_{80} to Fo_{84}). Equant chromite inclusions are common in olivine phenocrysts [Garcia et al., 2003]. Olivine grains make up the majority of phenocrysts present in the Kilauea bedrock (Figure 4.1E,F), and therefore have the highest potential for being physically isolated as individual mineral grains in processed sediment. Microprobe analysis of matrix olivine (Fo_{80} to Fo_{84}) shows similar compositions as the olivine phenocrysts. Pyroxene in the matrix ranges from diopside to augite (Wo_{31}, En_{31} to Wo_{43}, En_{54}), and plagioclase in the matrix (An_{56} to An_{68}) is composed of labradorite. A small amount of ilmenite, magnetite, chromite, and glass is also present. Modal mineralogy is estimated as 35 % plagioclase, 36 % pyroxene, 25 % oxides, and 10 % olivine (Table 4.A-1).

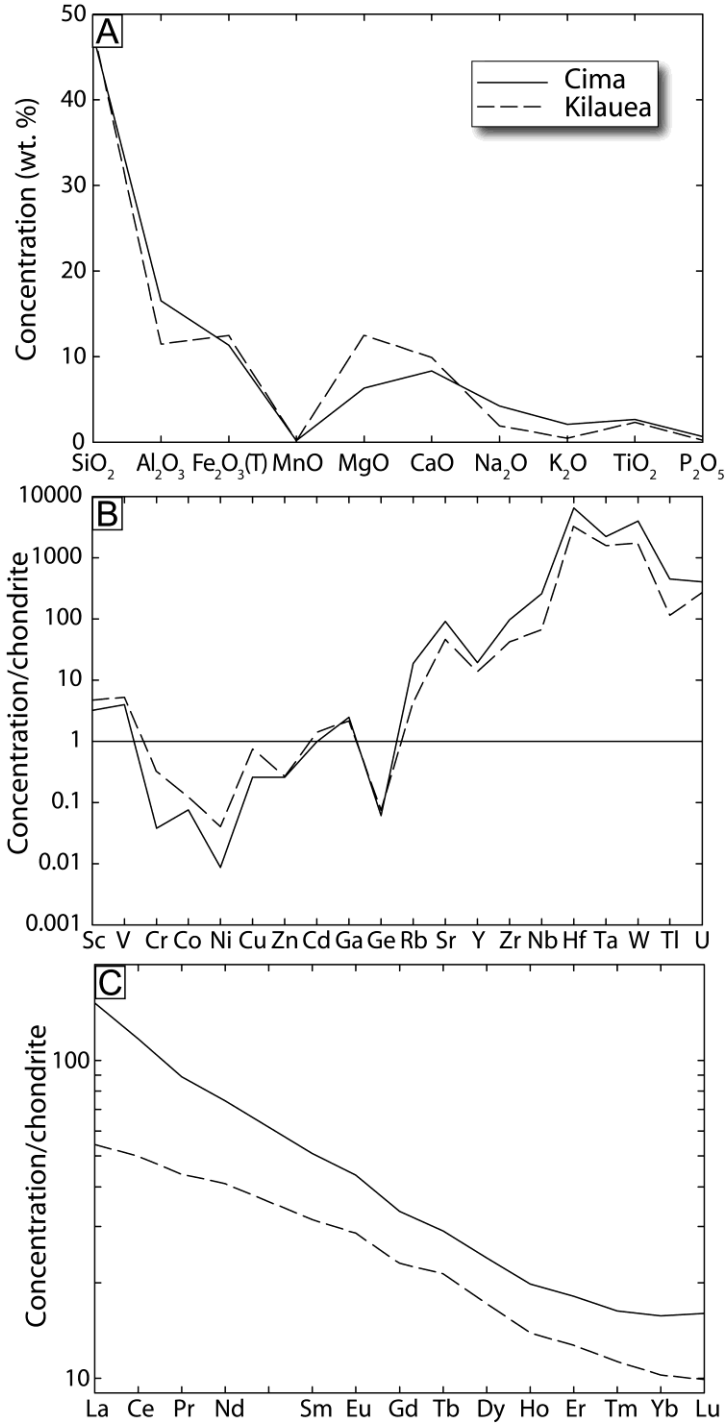

Figure 4.2. Chemistry results for Cima and Kilauea source rocks. (A) Major-element oxide (Table 4.A-2) concentrations. (B) CI chondrite [McDonough and Sun, 1995] normalized bulk-rock abundances of trace-elements (Table A.3). (C) CI chondrite normalized rare-earth-element (Table 4.A-4) patterns.

5.2.2. Geochemistry

Major-element-oxide results (Figure 4.2A) and trace-elements results (Figure 4.2B) for the pristine Kilauea basalt show a broadly similar composition to Cima basalt. Higher MgO concentrations result from pyroxene and olivine. Kilauea basalt contains low alkali components (Na_2O+K_2O) and is TiO_2 rich from secondary minerals, although high-TiO_2 glass is also present in some Kilauea basalts [Anderson and Wright, 1972]. Silica abundance is comparable to rocks and soils on Mars [McSween et al., 2009]. Trace-element abundances (Figure 4.2B) normalized to chondrite [McDonough and Sun, 1995] are presented as a reference. Bedrock REE results are consistent with a range of values reported from Kilauea studies [Pietruszka and Garcia, 1999; Garcia et al., 2000, 2003; Norman et al., 2005]. Kilauea is depleted in all REEs when compared to Cima (Figure 4.2C). No Eu anomaly is present.

6. Synthetic Sediment Sieving and Compositional Analysis

6.1. Cima

6.1.1. Textures

Incident light images with a perspective comparable to the Mars Science Laboratory (MSL) Mars Hand Lens Imager [MAHLI; Edgett et al., 2009] of loose sediment subdivided into different grain-size groups (Figures. 4.3, 4.4) show a mixture of rock fragments and isolated mineral grains. The grain-size distribution for Cima-derived pulverized and sieved sediment is positively skewed, with most sediment generated as fine pebbles to very coarse sand (-2.0 to 0.0 ϕ; Figure 4.3C; Table 4.A-5), with decreasing frequency from coarse to very fine sand (0.5 to 4.0 ϕ). The increased proportion of > 4.0 ϕ (< 62.5 μm) sediment represents the aggregation of silt

and clay sized grains which have not been subsequently sieved into finer fractions. Sediment coarser than very coarse sand (-2.0 ϕ) was not produced due to the nature of the experimental crushing process. Coarse-skewed distribution of the sediment is shown with the cumulative frequency distribution curve (black curve, Figure 4.3C), where 67 % of the sediment frequency is fine pebbles to very coarse sand (-2.0 to 0.0 ϕ).

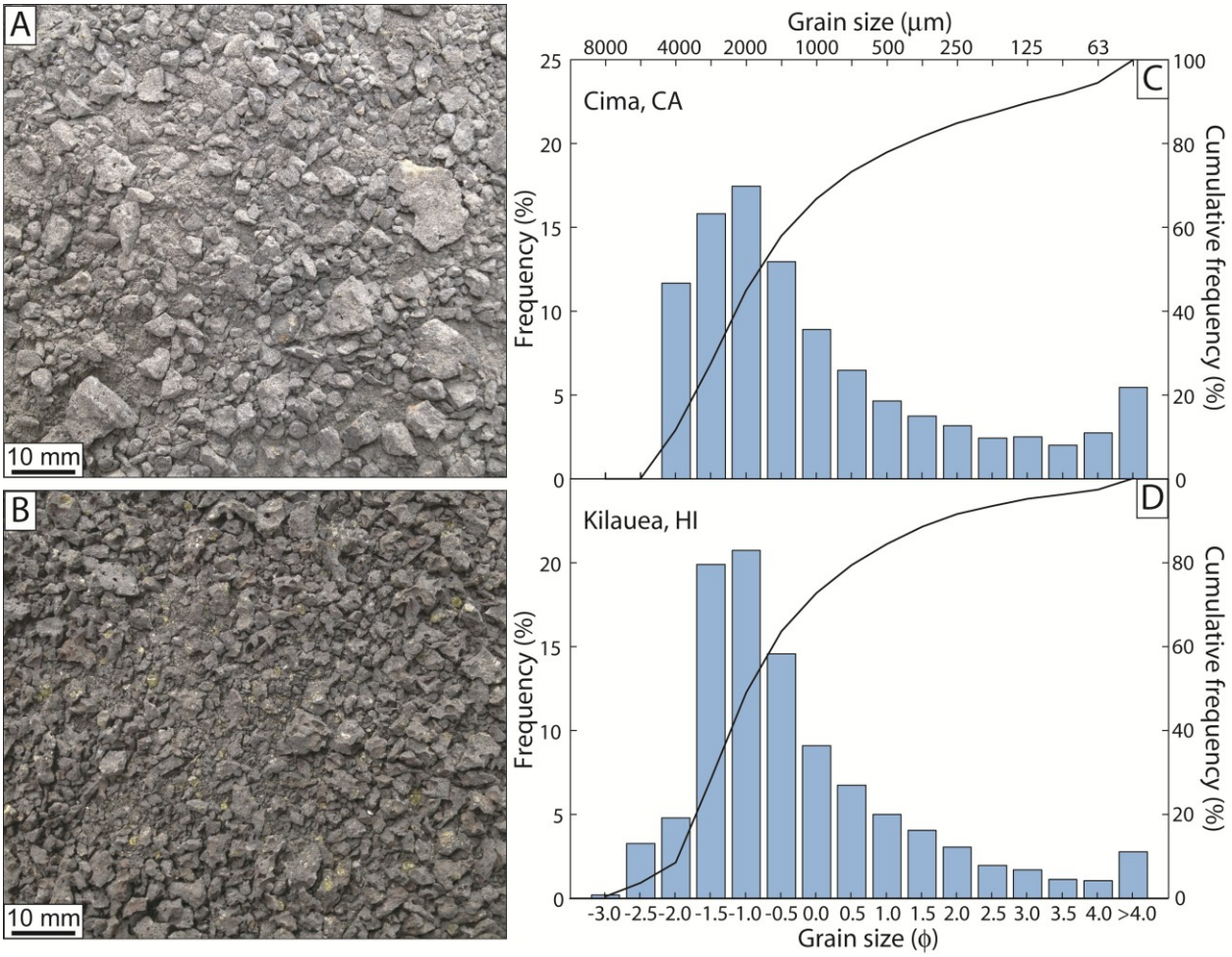

Figure 4.3. (A) Sediment generated from experimentally pulverized Cima source rock. (B) Sediment generated from Kilauea source rock. (C) Grain-size distribution histogram (Table 4.A-5) and cumulative frequency curve for Cima sediment, sieved at 0.5 ϕ fractions from -3.0 to 4.0 ϕ and including >4 ϕ pan for silt- and clay-sized particles. (D) Grain-size distribution histogram (Table 4.A-5) and cumulative frequency curve for sieved Kilauea sediment.

6.1.2. Mineralogy

The abundance of isolated minerals separated from the bedrock at each sieve size is controlled by the igneous texture of the original Cima basalt. Images of very coarse sand (0 ϕ), medium sand (2 ϕ), and very fine sand (4 ϕ) represent a comparative breakdown of plagioclase, pyroxene, and olivine grains from Cima basalt rock fragments (Figure 4.4A-C, Figure 4.A-1 in Appendix). At coarse grain sizes (-1 to 0 ϕ), sediments are entirely composed of basalt rock fragments (Figure 4.5A). Olivine and plagioclase grains are initially separated from the rock fragments at very low amounts (1 to 3 %) in coarse to medium sand (1 to 2 ϕ; Figure 4.5A). The proportion of liberated minerals increases significantly from fine to very fine sand (3 to 4 ϕ; Figure 4.5A). Individual grains of all major components including olivine, plagioclase, pyroxene, and oxides are present in very fine sand (4 ϕ). The greatest proportion of liberated minerals (44 %) is collected in the sieve pan (> 4 ϕ; Figure 4.5A), an aggregation of silt and clay sediment, reflecting the sparsely phyric texture of Cima basalt.

6.1.3. Major-Element Geochemistry

The geochemistry of samples (Figures. 4.6, 4.7; Tables 4.A-2 to 4.A-4) is used to ascertain the degree of compositional variation that results from the sieving of comminuted sediment into grain-size fractions relative to the original protolith. Plots of source-rock normalized major element results for crushed and sieved sediments are presented in Figure 4.6 (Table 4.A-2). Cima sediment samples are compositionally similar to the original basalt source rock for most oxides (Figure 4.6A). The greatest difference in major-element variation (enrichment and depletion from source rock) is for MgO (varies by 40 %), and minor variations are present for

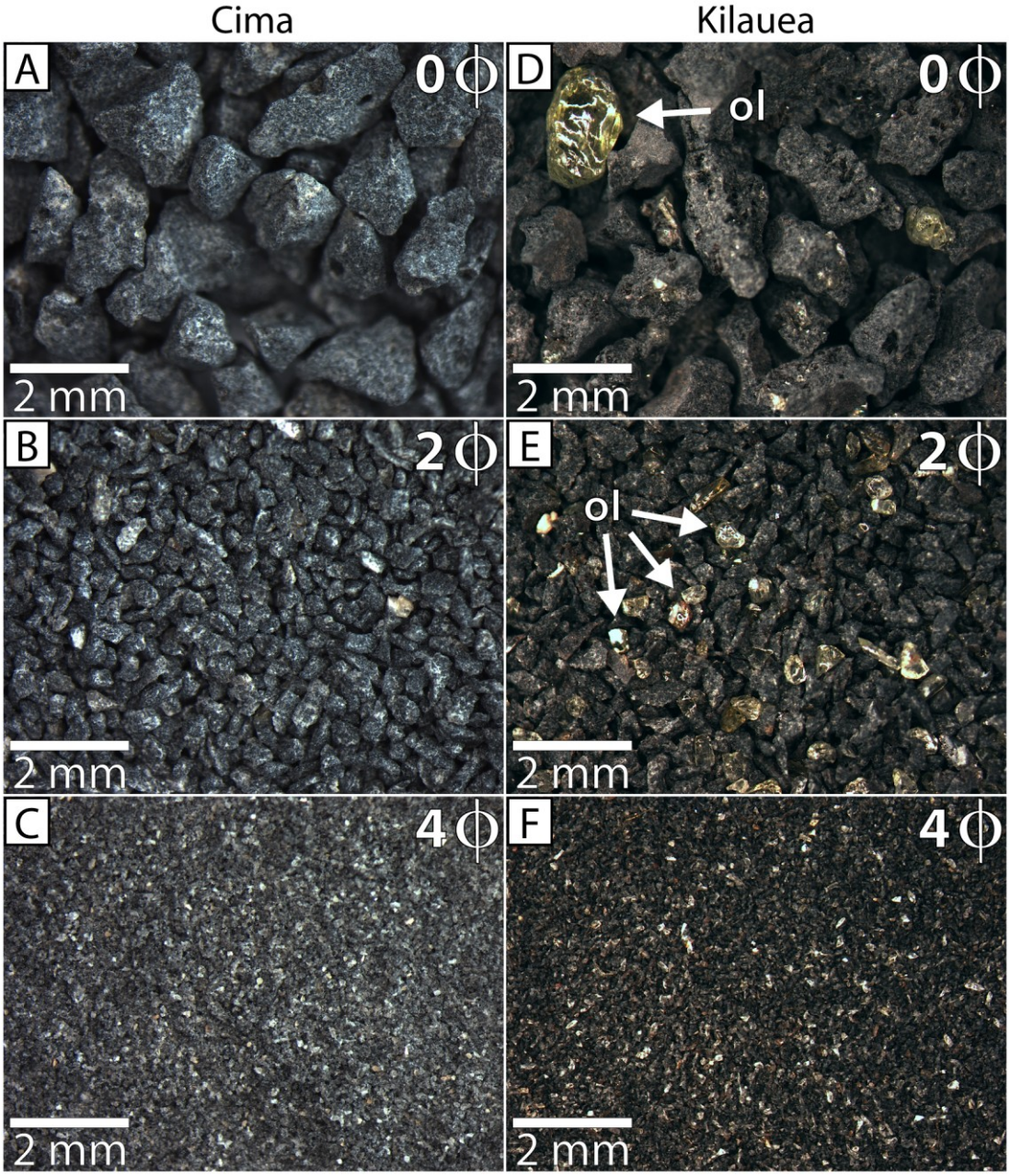

Figure 4.4. Incident-light images of comminuted and sieved sediments. (A) Rock fragments of Cima in very coarse sand. (B) Cima rock fragments in medium sand. (C) Accumulated pyroxene and olivine grains in very fine sand. (D) Kilauea very coarse sand with a small number of isolated olivine grains. (E) Greatest olivine accumulation in Kilauea medium sand. (F) Kilauea very fine sand with a reduced proportion of olivine. Mineral abbreviations in Figure 4.1, mineral proportions are depicted in Figure 4.5.

Fe_2O_3(T) (17 %), MnO (14 %), K_2O (12 %), and Al_2O_3 (12 %). Changes in sediment compositions are clearly controlled by the separation of pyroxene and olivine microphenocrysts, accounting for the variability in MgO and Fe_2O_3(T). Finer-grained samples (2.5 to 4.0 ϕ) show an accumulation in MgO, Fe_2O_3(T), and MnO (Figure 4.6A), corresponding to the concentration of pyroxene and olivine grains (Figure 4.5A). Only the clay and silt sized sample (> 4.0 ϕ) indicates a loss of MgO relative to the protolith, where pyroxene and olivine have been removed.

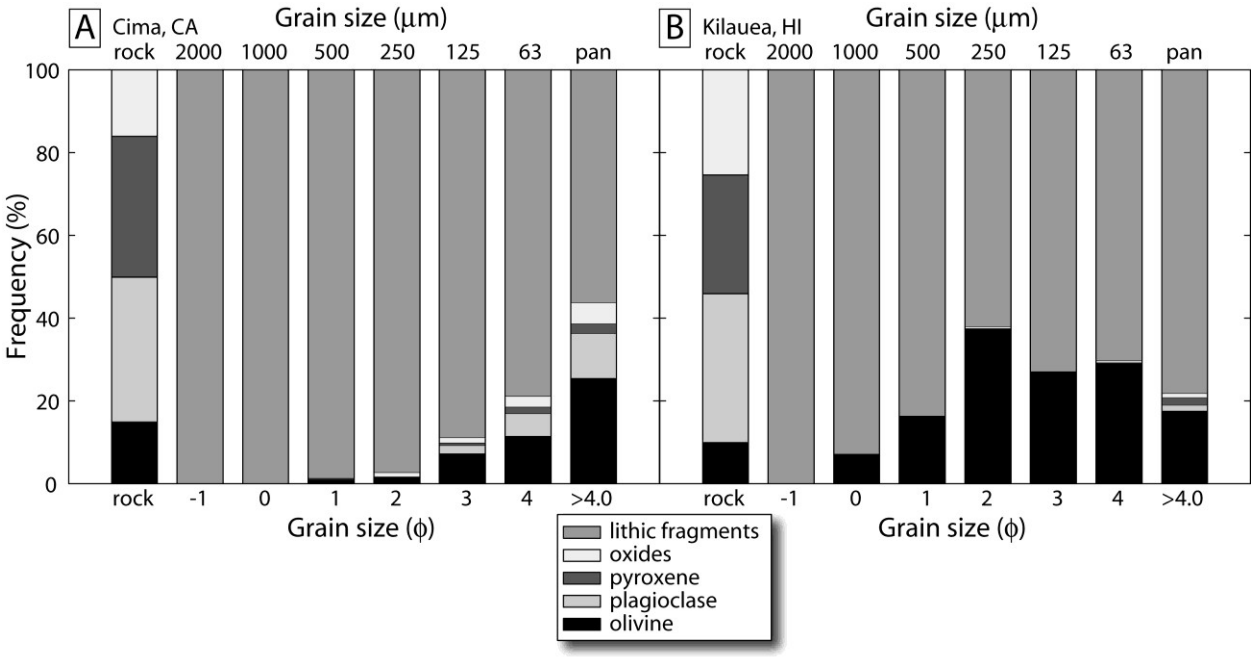

Figure 4.5. Modal compositions of rocks and sediments (Table 4.A-1). (A) Sediments derived from Cima basalt are largely composed of lithic fragments. Separation of isolated mineral grains occurs primarily in 3 to >4 ϕ (fine sand to silt) sieve fractions, although small amounts of olivine are present starting at 1.0 ϕ. The greatest abundance of olivine (26 %), plagioclase (11 %), and pyroxene (2 %) grains is in the >4 ϕ pan sample. **(**B) In contrast, olivine is isolated in Kilauea-derived sediments in 0 ϕ to >4 ϕ (very coarse to very fine sand) samples, with the greatest concentration at 2 ϕ (medium sand), due to the high abundance of olivine phenocrysts in Kilauea basalt.

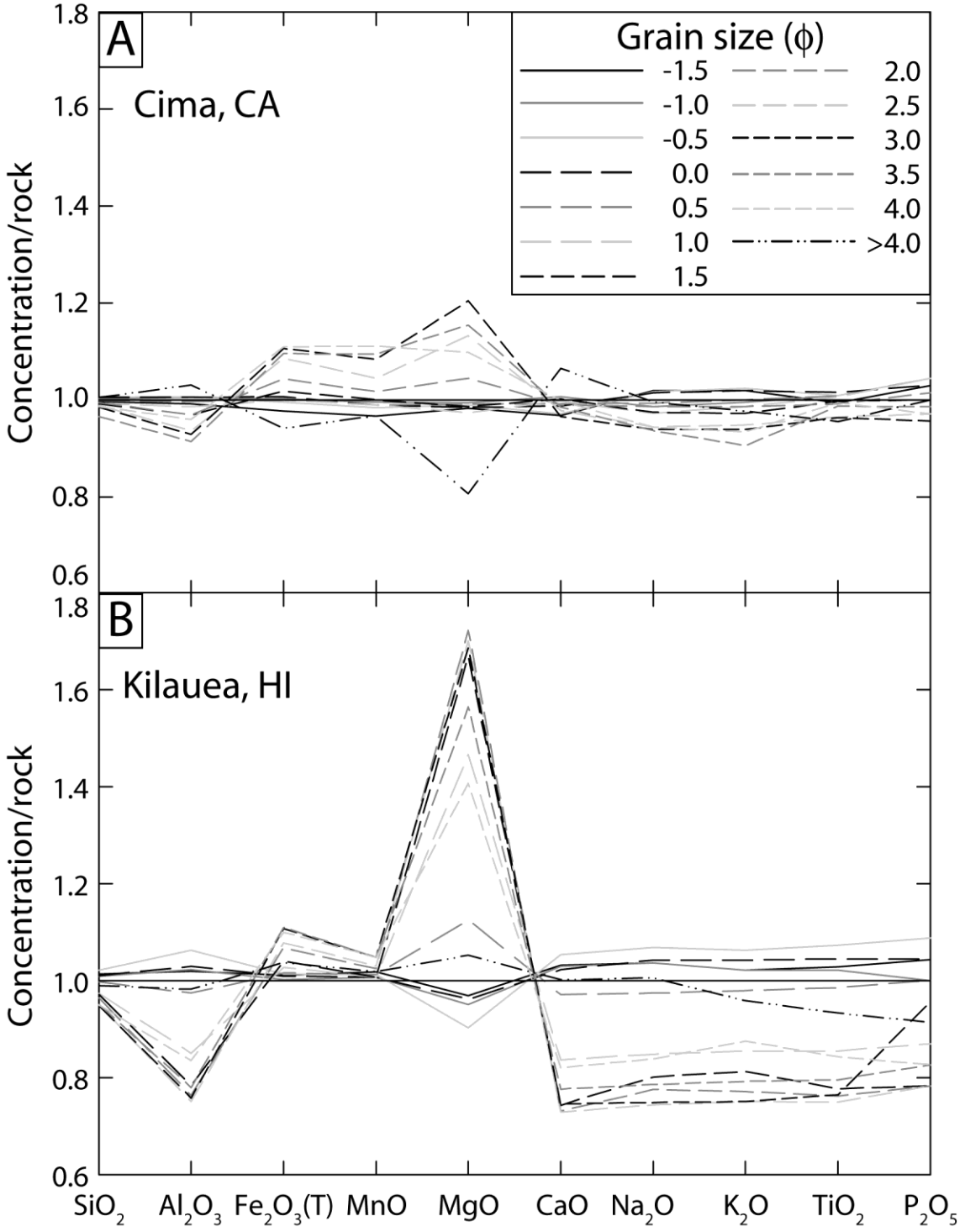

Figure 4.6. Source rock-normalized major element chemistry for sediment analogs. (A) Cima sediments are similar to the rock composition, except for a noticeable variation in MgO. (B) Kilauea sediments show greater compositional variations, especially in MgO, corresponding to olivine redistribution. Fine-grained sediment samples for both Cima and Kilauea display greater compositional variability than coarse-grained sediments.

6.1.4. Trace-Element and REE Geochemistry

Results of rock-normalized trace-element analyses are plotted in Figure 4.7. A clear separation between fine sediment (medium to very fine sand; 2.0 to 4.0 ϕ) and coarse sediment is observed (fine pebbles to medium sand; -1.5 to 1.5 ϕ) with the enrichment in V, Cr, Co, and Ni in fines. Enrichment of trace elements (Ni, Cr, Co) in olivine is expected from crystal field theory for octahedral co-ordination [Burns, 1970], and agrees with the accumulation of olivine in fine sediment, although minor Cr enrichment (20 %) is primarily attributed to higher accumulation of chromite and can also be concentrated in cliopyroxene. Coarse sediment (-1.5 to 0.0 ϕ) resembles rock fragments in petrographic analysis (Figures. 4.1A-C, A.1) and in imagery (Figure 4.4A-C). No discernible variation in Rb or Sr exists between grain-size groups. Fractionation of REE (represented by La, Nd, Sm, Eu, Gd, Dy, Er, Yb; full results in Table 4.A-4) is not present (Figure 4.7A). A preferential breakdown of heavy mineral components is not present in light rare earth (LREE) to heavy rare earth (HREE; La_N/Yb_N = 0.98 to 1.04), LREE/LREE (La_N/Yb_N = 1.00 to1.05), or HREE/LREE (La_N/Yb_N = 0.99 to 1.08) rock normalized ratios.

6.2. Kilauea

6.2.1. Textures

Medium pebbles to silt and clay (-3.0 to > 4.0 ϕ; Figure 4.3D; Table 4.A-5) were produced from the Kilauea protolith (Figure 4.1D-F). The sediment distribution is coarse-skewed, with most sediment present as very fine pebbles to coarse sand (-2.0 to 0.5 ϕ). Sediment in the pan sieve suggests further sieving is needed to separate silt and clay sized grains for a complete distribution beyond > 4.0 ϕ (< 62.5 μm). Medium to fine pebbles (-3.0 to -2.5 ϕ) were manually

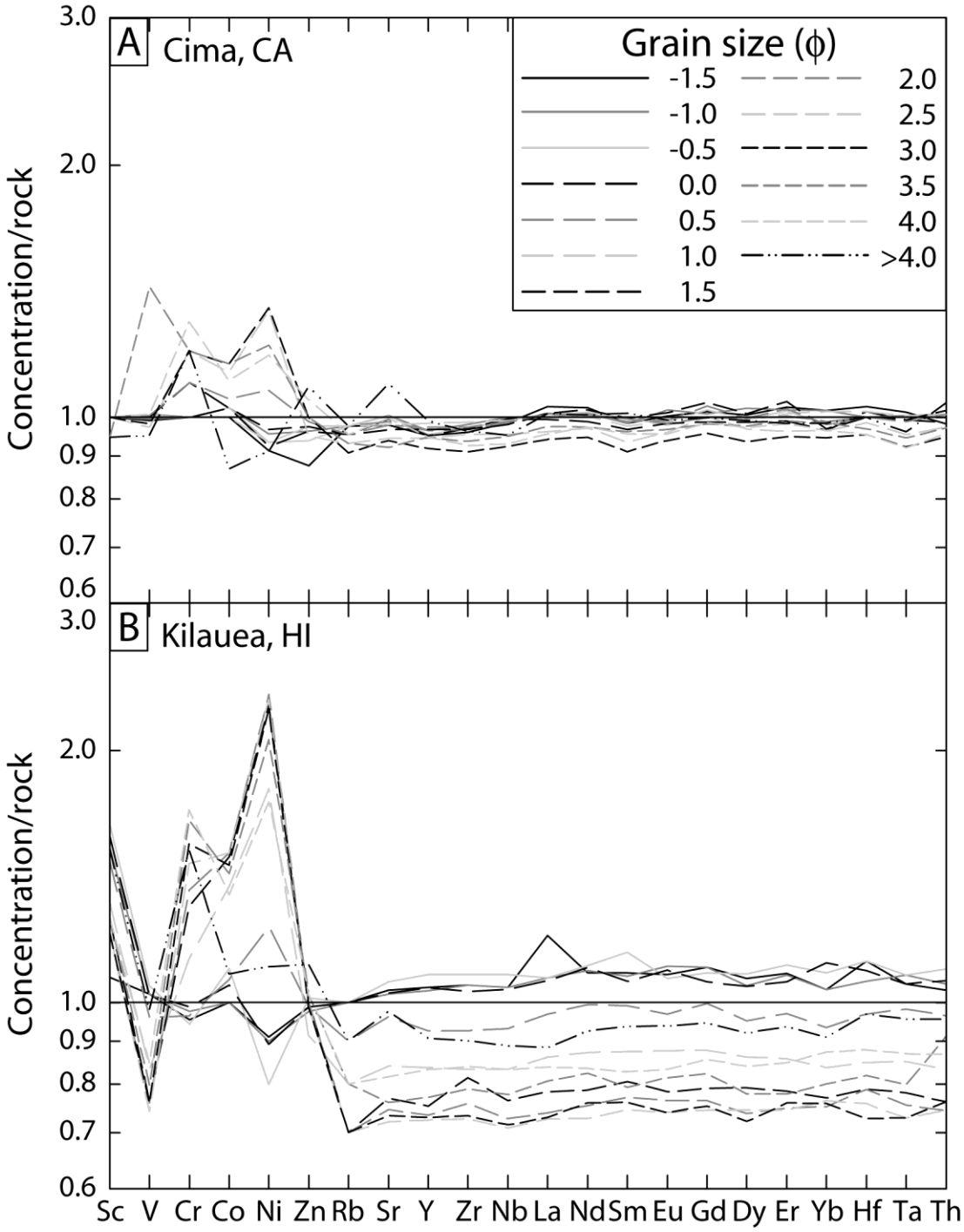

Figure 4.7. Bedrock-normalized transition and REE compositions for A) Cima and B) Kilauea sediment. Higher variations in sediment compositions are present for light transition elements for both data sets. REE depletion is consistent in fine-grained sediments.

sorted from the fine pebbles (-2.0 ϕ), but only account for a small number of grains (n = < 5). The cumulative distribution (Figure 4.3D, black curve) of Kilauea sediment is positively skewed, and 68 % of the sediment frequency is very fine pebbles to coarse sand (-2.0 to 0.5 ϕ).

6.2.2. Mineralogy

Olivine phenocrysts are the primary source for isolated mineral grains and are the primary mineral fractionated in sieved Kilauea sediment, as seen in sediment images (Figure 4.4D-F) and in the petrographic analyses (Figure A.l). Grains of olivine are first liberated in very coarse sand (0 ϕ; Figure 4.4D), with the proportion of separated grains increasing with decreasing grain size (Figure 4.5B). Images of medium sand (2 ϕ; Figure 4.4E) show the greatest accumulation (38 %) of olivine grains (Figs. 4.5B). This abundance mimics the abundance of medium sand-sized olivine phenocrysts in Kilauea basalt. A smaller proportion of olivine is visible in very fine sand (Figure 4.4F). Other components including plagioclase, pyroxene, and oxides are present only in silt and clay sediment (> 4 ϕ; Figure 4.5B), and only represent 4 % of the sediment distribution.

6.2.3. Major-Element Geochemistry

The most significant compositional variation between Kilauea source rock and sediment (Figure 4.6B) is for MgO (82 %), which increases to 170 % of source rock at 2.0 ϕ and decreases to 90 % of source rock at -0.5 ϕ. This reflects the concentration of MgO-rich olivine phenocrysts from 1.0 to 4.0 ϕ, and especially at 2.0 ϕ, and the relative immobility of Fe_2O_3(T) across all sieved sediment. Minor compositional variations are present for CaO (varies by 32 %), Na_2O (32 %), TiO_2 (32 %), K_2O (31 %), Al_2O_3 (31 %), and P_2O_5 (30 %). The proportion of plagioclase,

suggested by CaO and Na_2O values, increases in coarse sediment (-1.5 to 0.0 ϕ) and is depleted in finer-sized grains due to removal and concentration of olivine, respectively. A clear compositional trend in grain size is noticeable, with olivine (MgO) accumulation in (1.0 to 4.0 ϕ) matched by the depletion in Al_2O_3, CaO, Na_2O (32 %), K_2O, TiO_2, and P_2O_5, similar to trends observed in Kilauea lavas [Garcia et al., 1996]. The concentration of MnO is low (< 0.2 wt. %) with no variation between samples.

6.2.4. Trace Element and REE Geochemistry

Kilauea sediment samples (Figure 4.7B) have greater variations for most trace elements than Cima sediment. Ni has the greatest variation (153 %) among Kilauea samples. The enrichment of Cr, Co, and Ni (Figure 4.7B) in coarse to very fine sand (1.0 to 4.0 ϕ) matches the enrichment of MgO and Fe_2O_3(T) (and Al_2O_3 depletion) caused by olivine phenocrysts (Figure 4.5B), from crystal field theory for octahedral co-ordination [Burns, 1970], and demonstrates the overwhelming compositional control phenocrysts have in Kilauea sediment. Chromite (Cr-spinel) inclusions within olivine phenocrysts control Cr variability and explain Cr paring with these trace elements.

Results of Kilauea sediment REEs are retained with very little variability in rock-normalized ratios (La_N/Yb_N = 0.95 to 1.16; La_N/Yb_N = 0.93 to 1.11; La_N/Yb_N = 0.95 to 1.07). Concentrations of REEs (Figure 4.7B) cluster into three general groups based on grain-size. Coarse sediment samples (-1.5 to 0.0 ϕ, very fine pebbles to very coarse sand) are the most enriched across all REEs, and fine-grained sediments (1.5 to 3.5 ϕ; medium to very fine sand) are characterized by the greatest depletion in REEs. A third group (4.0 and >4.0 ϕ; very fine sand

and silt) is similar to the source rock or moderately depleted in REEs. A depletion in most lithophile trace (Rb, Sr, Y, Zr, Nb) and rare earth elements in fine-grained sediment (1.5 to 3.5 ϕ; medium to very fine sand) is consistent with the accumulation of olivine, and demonstrates that trace-element concentrations in Kiluaea sediment are largely controlled by the proportion of olivine.

6.3. Comparisons and Synthesis of Mineral Fractionation by Grain Size

Textural and compositional differences between the two selected source rocks provide a basis to compare the influence they have on resultant sediment grain-size distributions, mineral separation, and associated chemical changes. Although both sample sets were generated using the same mechanical processes of crushing and sieving, minor differences in the resulting grain-size distributions are present. Cima-derived sediment lacks grains at the -3.0 to -2.5 ϕ sieve fractions (Figure 4.3C) that are present in Kilauea-derived sediment (Figure 4.3D). In addition, a larger proportion of sediment was generated at -2.0 ϕ from the Cima protolith when compared to Kilauea derived sediment. This difference reflects the aphanitic nature of the Cima basalt relative to the phaneritic Kilauea basalt, and presents a characteristic that repeatedly imprints the results of this study. The grain sizes of generated sediment are comparable to observed range of cobbles through very fine sand from the MER MI [McGlynn et al., 2011].

The mineralogy and textures of Cima and Kilauea protoliths determine the mineralogy of liberated mineral grains, the total proportion of isolated mineral grains, and the grain size distributions of isolated individual mineral grains in sieved sediment (Figure 4.5). Liberated grains (Figs. 4.4, 4.5) of plagioclase, olivine, and pyroxene in Cima sediment and olivine grains

in Kilauea sediment simply reflect the mineralogy of the respective source rocks (Figs. 4.1, 4.5). Differences in the crystal-size distribution in aphanitic Cima and phaneritic Kilauea protoliths and the physical behavior of crushed minerals determine the grain-size distributions of isolated mineral grains in sediment. The breakdown of phenocrysts in Cima coarse sediment is rare due to the abundance of fine to very fine sand-sized phenocrysts in Cima basalt source rock. It is not until the breakup approaches silt-sized grains (> 4 ϕ) that isolated minerals in the matrix become more abundant (Figure 4.5A). Similarly, the distributions of liberated olivine in sand-sized Kilauea sediment samples (Figure 4.5B) resemble the initial grain-size distribution of olivine phenocrysts in the source rock.

Major-element-oxide abundances are controlled by the separation of phenocrysts and microphenocrysts from the source rock. A greater abundance of larger phenocrysts in the Kilauea basalt (Figure 4.1D-F) results in a more pronounced compositional difference for Kilauea sediment (Figure 4.6B) than for Cima sediment (Figure 6A). For most major elements, the compositional differences between source rock and sediment samples are in part controlled by grain size, reflecting the size differences of Cima microphenocrysts and Kilauea phenocrysts. Coarse sediment samples (< 2.0 ϕ Cima, < 0.5 Kilauea) exhibit minimal chemical variation, while fine-grained samples (> 2.0 ϕ Cima, > 0.5 Kilauea) have more pronounced variations in major chemistry relative to the respective source rock compositions. Al_2O_3 concentrations do not change appreciably for either Cima (4 % variation) and Kilauea sediment (7 % variation), and reflect the presence of plagioclase principally in the matrix. Previous approaches have used element ratios, including Fe:Ti [McSween and Keil, 2000; McLennan, 2000; McGlynn et al.,

2008] to explore compositional fractionation in sediment. In this assessment some fractionation in other elements is detected, based on phenocryst redistributions.

Trace-element analysis is beyond the capabilities of the Alpha Particle X-ray Spectrometers on MER [Rieder et al., 2003, 2004; Gellert et al., 2004, 2006] and MSL rovers. However, trace-element patterns in this study characterize important changes in primary minerals and oxides, which are relevant for studies in terrestrial provenance analysis and provide a framework for interpreting future data from Mars landers and sample return missions.

Differences in trace-element concentrations between Cima and Kilauea sediment sets are in the degree of compositional variation, and in the grain sizes at which trace elements are mobilized. The greater initial proportion of phenocrysts in Kilauea basalt enables a greater proportion of material to be redistributed in sieved sediment, and controls the greater variation in trace elements in Kilauea sediment (Figure 4.7B) when compared to Cima sediment (Figure 4.7A). Both Cima and Kilauea sediment sets show grain-size control, with coarse sediment enriched in REEs relative to fine sediment. The redistribution of phenocrysts in Kilauea sediment results in REE depletions in medium to very fine sand (1.5 to 3.5 ϕ), while REE depletion in Cima sediment occurs at fine to very fine sand (2.5 to 4.0 ϕ) due to the smaller microphenocryst sizes in the source rock. The REE compositions in both sample sets appear to represent the proportion of matrix components, which resemble source rock compositions in silt (>4.0 ϕ).

7. Implications of Compositional Variations by Grain Size

7.1. Interpreting the mineralogy of Mars "soil" sediment

Plotting major-element oxides of the analog source rock and derived sediment samples (Figure 4.8) in a total alkali-silica diagram (TAS) provides a way to compare the compositional variations from sieving to the compositions of Mars basaltic rock and "soil" sediment, using geochemical data collected from the Spirit rover Alpha Particle X-Ray Spectrometer (APXS) in Gusev Crater [*e.g.*, McSween et al., 2006a, b]. TAS diagrams are commonly used to classify igneous rocks on Mars, and also as a medium to explore relationships between rock mineralogy and soil sediment compositions [McSween et al., 2009], and possible weathering pathways [McSween, 2010]. Cima trachybasalt (black triangle, Figure 4.8) and Kilauea basalt (black circle, Figure 4.8) represent high- and low-alkali compositions, bracketing the compositions of most Gusev rocks (black squares, Figure 4.8) and soils (open squares, Figure 4.8). The ranges and trajectories of Cima sediments (shaded triangles, Figure 4.8) and Kilauea sediments (shaded circles, Figure 4.8) are indicated by two-headed arrows.

Analog synthetic sediment compositions show similar patterns to the trajectory and range of sediment in Gusev Crater (open squares, Figure 4.8). The concentrations of Na_2O+K_2O increase with SiO_2 in Cima, Kilauea, and Gusev sediments. The compositional range for Cima sediment is more constrained, but Kilauea sediment compositions generally match the compositional range and trajectory for Gusev sediment.

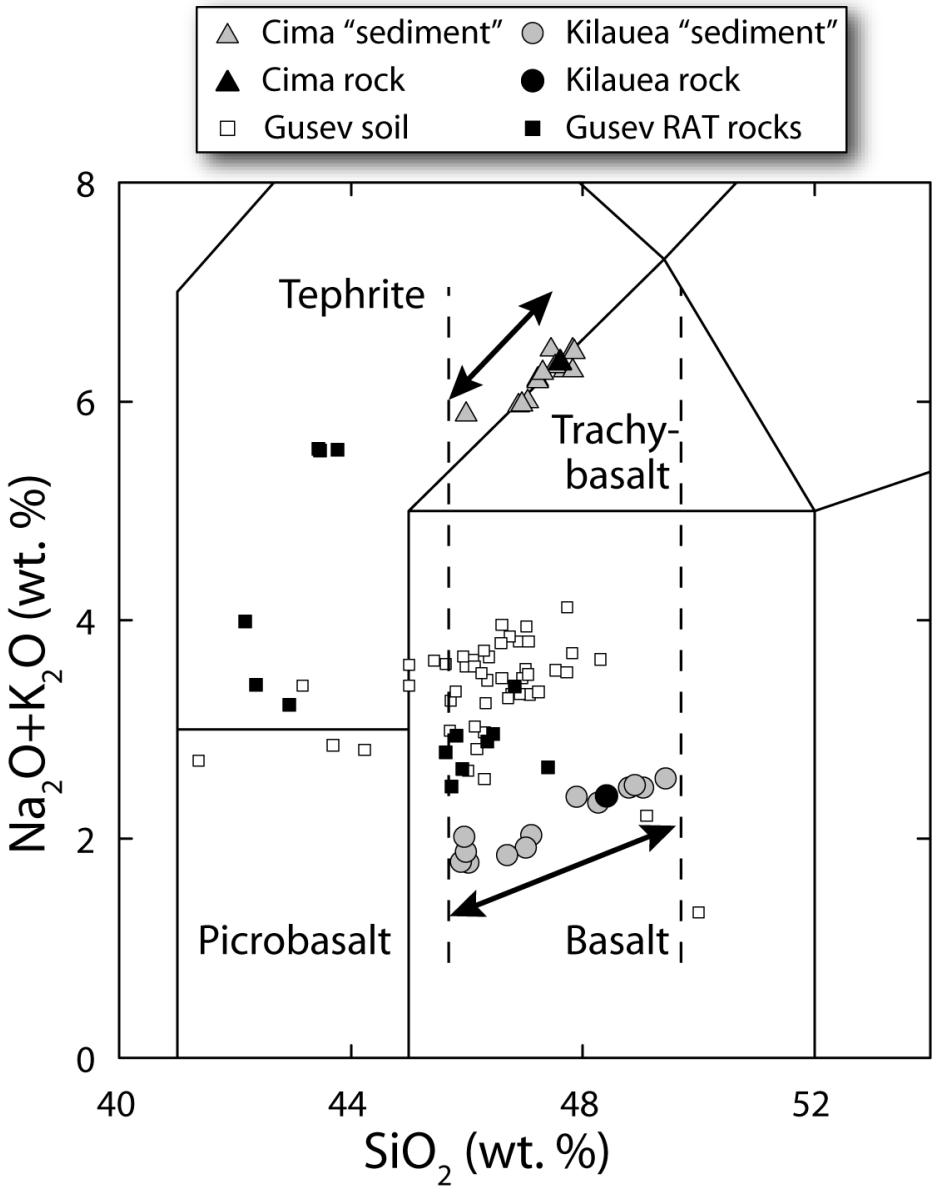

Figure 4.8. Total alkalis (Na_2O+K_2O) vs. SiO_2 classification diagram for volcanic rocks. Sediments generated from crushed and sieved Cima and Kilauea rocks display ranges in SiO_2 abundance caused by physical mineral sorting that is comparable to variations in soil chemistry in Gusev Crater. The similar spreads (dashed lines) and trajectories (arrows) for both sediment collections demonstrate hydrodynamic-driven compositional changes. The compositions of most Gusev soils can be generated by physical sorting from local source rocks and do not require chemical alteration. Modified from McSween et al. (2009).

The extended range in Kilauea sediment compositions (dashed lines, Figure 4.8), compared to Cima sediment compositions, results from the significant redistribution of primary minerals, principally olivine (Figure 4.5B). This is not to imply that all sediments in Gusev Crater are derived from a single protolith, as in the Kilauea sediment, but to demonstrate that considerable compositional spread exists from the grain-size variation alone, even before the redistribution of mineral species by sorting [*e.g.*, McGlynn et al., 2012]. Gusev Crater sediments exhibit a greater variation in alkali compositions (Na_2O+K_2O) than those of either analog sediment group, which suggests that the compositional spread of Gusev soils reflects, in part, their derivation from multiple protoliths with varying alkali compositions. Interior compositions of rock samples, abraded by the Spirit rover Rock Abrasion Tool (RAT; black squares, Figure 4.8) are possible source rocks for locally generated sediment in Gusev Crater.

7.2. Compositional Trends in A-CNK-FM Space

Changes in sediment compositions arising from chemical weathering can be interpreted by plotting the molar proportions of A (Al_2O_3), CNK ($CaO^*+Na_2O+K_2O$), FM (FeO_T+MgO) in a ternary diagram [Nesbit and Young, 1989; Nesbitt and Wilson, 1992; Nesbitt et al., 1996]. Unaltered source rocks such as basalt would typically plot along the olivine-feldspar join, between the FM-apex and the feldspar end member. As the compositions of sediment derived from basalt source rocks change due to chemical weathering the position of soils in the A-CNK-FM diagram diverge away from the original basalt location. Chemically weathered sediment generally follows a characteristic three-step pathway [Nesbitt and Wilson, 1992]. Firstly, olivine dissolution from the reduction in FeO_T+MgO plots parallel to the olivine-feldspar join and away from the FM-apex. Secondly, the loss of feldspars is represented by the change in position away

from the CNK apex and a trajectory perpendicular to the olivine-feldspar join. Thirdly, with the accumulation of Al-bearing clays, soil compositions plot towards the A-apex.

Soils examined by the MER Spirit rover in Gusev Crater show limited compositional deviation from Gusev rocks in A-CNK-FM plots, which permits the presence of a small amount of sulfate minerals and clays [McGlynn et al., 2012]. In general, most Gusev sediments plot subparallel to the olivine-feldspar join, a trend that has been interpreted as chemical weathering (mostly olivine dissolution) under acidic sulfur conditions [Hurowitz and McLennan, 2007]. However, olivine dissolution modeled from known rock samples in Gusev Crater cannot generate the composition of all Gusev soils, which implies a role for post-comminution mixing and compositional modification by sorting [McGlynn et al., 2012]. Without the presence of soils with compositions that plot perpendicular to the olivine-feldspar join and towards the A-apex, large quantities of clays are interpreted not to be present, and chemical weathering may be a less important process than sorting.

The compositional spread for analog sediments, as well as for sediments at Gusev Crater and Meridiani Planum, approximately parallels the olivine-feldspar join (Figure 4.9A). As shown with arrows, sieved sediment samples diverge in two directions away from their respective source rocks. Accumulations of olivine (ol+) in Kilauea sediments, and of olivine and pyroxene (ol+, px+) in Cima sediments, are shown by movement towards the FM apex. Conversely, the removal of FM-bearing minerals causes sediment to move away from the FM apex (ol-, px-). A greater range in FM chemistry (Figure 4.9A) for Kilauea sediment is attributed to the

Figure 4.9. (A) A-CNK-FM ternary plot for sieved Cima and Kilauea sediment away from source rocks, towards the FM-apex result from the accumulation of olivine (ol+) and pyroxene (px+), and away from the FM-apex result from the removal of olivine (ol-) and pyroxene (px-) relative to the source rocks. Compositional variations parallel to the olivine-feldspar join are represented by histograms (bin = 5) of FM* (McGlynn et al., 2012). Differences in phenocryst availability control the compositional spread of (B) Cima and (C) Kilauea sediment. Sieved Kilauea sediment matches a similar FM* spread for most Gusev and Meridiani soils demonstrating the importance of physically-induced compositional changes. Sorting of analog sediment allows for the complete separation of primary minerals olivine, pyroxene, and feldspar, to produce sediment compositions throughout the extent of the olivine-feldspar join. Cima and Kilauea sediment trends demonstrate that the compositions of Martian sediments do not require chemical alteration. Mineral abbreviations are olivine, ol; feldspasr, fs, pyroxene, px.

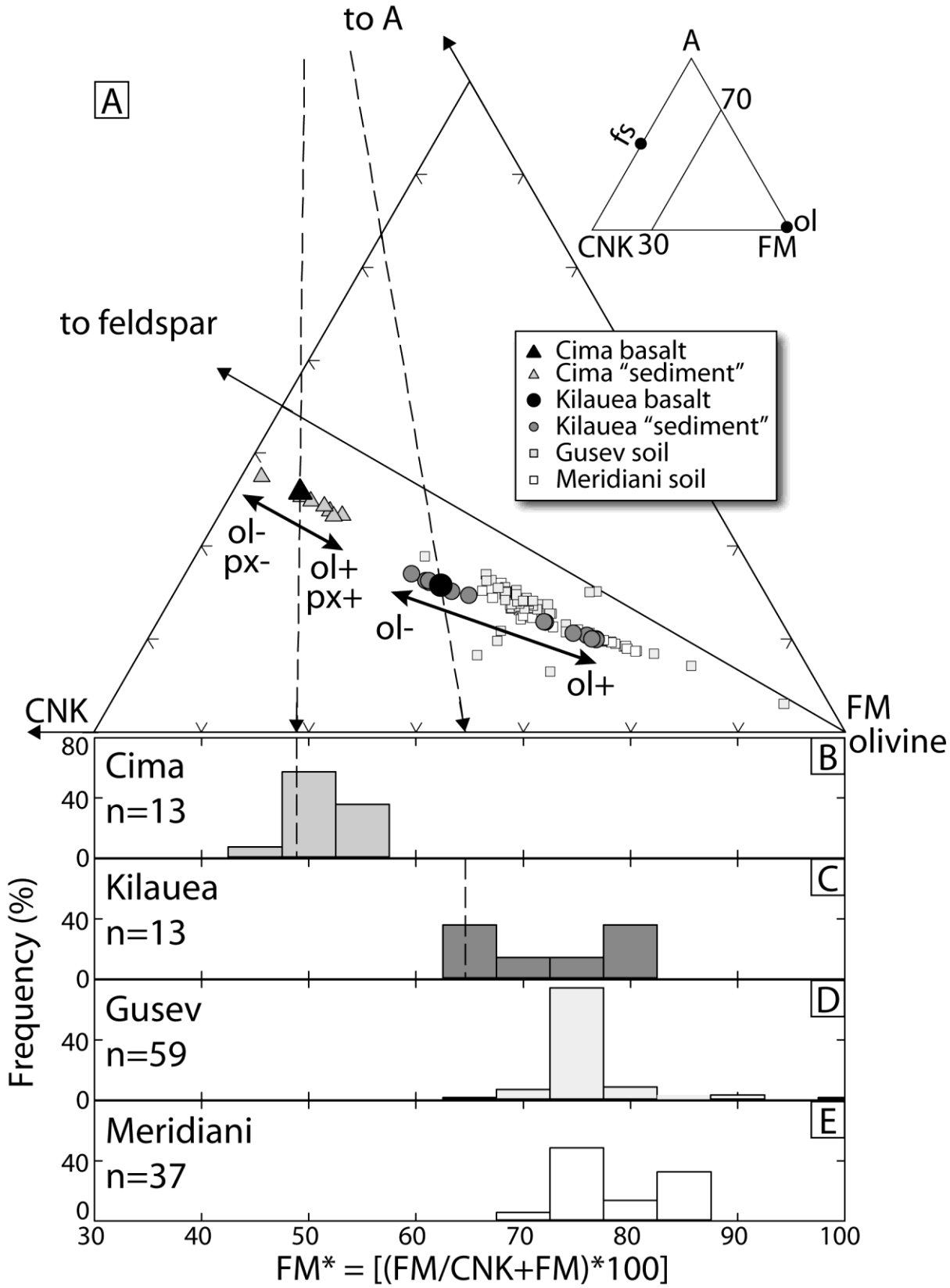
A
to A
to feldspar
CNK
FM
olivine
A
70
fs
ol
CNK
30
FM
Cima basalt
Cima "sediment"
Kilauea basalt
Kilauea "sediment"
Gusev soil
Meridiani soil
ol-
px-
ol+
px+
ol-
ol+
B
Cima
n=13
C
Kilauea
n=13
D
Gusev
n=59
E
Meridiani
n=37
Frequency (%)
0
40
80
30
40
50
60
70
80
90
100
FM* = [(FM/CNK+FM)*100]

redistribution of abundant olivine phenocrysts. Coarse sediment (0 ϕ, Figure 4.4D) resembles the composition of the protolith, while liberated olivine grains are concentrated at 2 ϕ (Figure 4.4E), and are also present at 4 ϕ (Figure 4.4F). Despite different initial basalt compositions (Figs. 4.2, 4.8), Cima sediments match the trajectory and Kilauea sediments have a similar range and trajectory to sediments in Gusev Crater and Meridiani Planum (Figure 4.9A). Such trends can be produced from the sieving of physically shattered basalt and do not require chemical weathering.

To compare variations in sediment compositions without the effects of Al_2O_3 variation, samples are calculated as the quantity FM* McGlynn et al. [2012], defined as molar ((FeO_T+MgO) / (CaO*+Na_2O+K_2O+ FeO_T+MgO)) * 100, which is the equivalent of projecting data onto the base of the A-CNK-FM plot. The FM* values for analog sediments (Cima and Kilauea) and MER (Gusev and Meridiani) soils are expressed as frequency histograms with a bin width of 5 FM* units (Figure 4.9B-E). Cima sediments have a narrow range of FM* values (Δ FM* = 10; Figure 4.9B). Abundant olivine phenocrysts in Kilauea basalt, concentrated in medium-to-fine sand and depleted in very coarse sand (Figure 4.6B), generate a more extensive range of FM* values (Δ FM* = 18; Figure 4.9C). Gaps in Cima and Kilauea sediment histograms result from the uneven separation of olivine and pyroxene minerals in soils plotting towards the FM apex (Figure 4.9A), where olivine and pyroxene proportions occur in finer ϕ fractions. Sediments in Gusev Crater (Δ FM* = 32; Figure 4.9D) and Meridiani Planum (Δ FM* = 14; Figure 4.9E) show extensive ranges in FM* values. However, the range in FM* chemistry for Kilauea sediment approximates the general range of most Gusev and Meridiani sediments. Analog Kilauea sediment, extending from rock, towards and away from the FM apex, shows a trajectory

that resembles Gusev Crater and Meridiani Planum soil (Figure 4.9A), from the accumulation and removal of olivine in the absence of chemical alteration. The major compositional spread for sediments at Gusev Crater and Meridiani Planum occurs parallel to the olivine-feldspar join (Figure 4.9A), caused by a combination of sediment mixing from different protoliths, sorting of FM-bearing minerals, sulfate mixing, and minor chemical alteration by acid-sulfate or phyllosilicate additions [McGlynn et al., 2012], in a trend similar to sieved analog sediments. The data only represents sieved grain-size populations, not actual sorting, which could complexly mix the different populations or isolate and separate constituent mineral components, generating an even larger divergence in sediment compositions. The role of sorting is considered critical, and is discussed below.

8. Sorting Effects

8.1. Threshold Friction Velocity (u_{*t}) Modeling

As evident from analog sediment mineralogy (Figure 4.5) and corresponding geochemistry (Figs. 4.6, 4.7), sieving of synthetic sediments has the capacity to produce significant mineral redistribution, and lays the foundation to postulate the effects of sorting. Here we apply aeolian transport models to better explore the how sorting may impose considerable compositional changes on martian sediment. Density sorting of sediment on the surface of Mars is explored using threshold friction velocity (u_{*t}), which represents the minimum friction velocity required to initiate movement of soil particles. Wind erosion is initiated when fraction velocity (u_*) is greater than the threshold friction velocity (u_{*t}). This parameter also represents the strength of forces among soil particles and function of sediment textures, soil moisture, surface cover,

subsurface crust, and other roughness elements [*e.g.* McKenna Neuman, 2003; McGlynn et al., 2005; Okin et al., 2009; Lancaster et al., 2010] to resist wind erosion. Empirical solutions, building upon Bagnold [1941] and Owen [1964], have been used to determine the threshold friction velocities for particles under different conditions [Greeley and Iversen, 1985; Raupach et al. 1993; Ravi et al., 2004] including wind tunnel experiments approximating atmospheric conditions on Mars [Iversen and White, 1982]. Based on those results, threshold friction velocity is expressed by Shao and Lu [2000] as:

$$u_{*t} = \sqrt{A_N \left(\sigma_p g d + \frac{\gamma}{\rho d}\right)} \quad (1)$$

where A_N is an empirical constant for interparticle cohesion, $\sigma_p = \rho_p / \rho$ is the particle to air density ratio, g is gravitational acceleration, d is particle diameter, and γ is an electrostatic force constant. Recommended values from Shao and Lu [2000] are used for interparticle cohesion A_N = 0.0123 and electrostatic force γ = 3 x 10^{-4} kg s^{-2}. Planetary conditions for Mars include gravity, g = 3.69 m s^{-2} and atmospheric density, ρ = 1.54 x 10^{-2} kg m^{-3} at 6.1 mb and 209 K [Bridges et al., 2010]. In Figure 10, particle sizes, *d,* are modeled from 10 to 2000 μm (7 to -1.0 ϕ) shown as solid curves, and as dashed curves where projected to extended beyond 2000 μm (> 2 mm, < -1.0 ϕ), in order to recognize problems of aeolian transport of large grains. Differences in particle density are ineffective in influencing u_{*t} for silt- and clay-sized grains (> 4.0 ϕ) due to the overwhelming role of van der Waals and electrostatic forces in theoretical predictions [Shao and Lu, 2000]. Average densities for Cima (2835 kg m^{-3}) and Kilauea (2601 kg m^{-3}) bedrock were experimentally measured (Table 4.A-6) and the densities for common minerals in basalt, including fayalite, forsterite, and plagioclase were compiled from existing data [Table 4.A-6; Roberts et al., 1990].

Threshold friction velocity curves are plotted for the above materials in Figure 4.10A. The effect of particle density on u_{*t} is noticeable for sand- through cobble-sized grains, where Cima and Kilauea sediment have lower u_{*t} than denser olivine at the same grain size, holding all other variables constant (Table 4.A-7). Dividing olivine into the end member compositions fosterite and fayalite shows the range in density for olivine. At Fo_{50} Mars rocks [McSween et al., 2008] and soils [McSween et al., 2010; McGlynn et al., 2012] would plot between the fosterite and fayalite threshold velocity curves. Differences in density between constituent minerals in Kilauea and Cima rock-derived sediments enable the potential for sorting by the removal of plagioclase relative to olivine.

The concept of equivalence establishes the grain sizes of rocks and minerals with difference densities or sphericities that can travel together at a fixed energy level. In this exercise, we are focusing on the effects only due to density variation and not shapes in part because of the shape differences are small. To illustrate the grain-size range of phases in equivalence for the materials of interest, we arbitrarily selected a starting u_{*t} of 2 ms^{-1}, which would be an appropriate velocity for Mars [Sullivan et al., 2000] and which is shown by the horizontal dotted line in Figure 4.10A and 4.10B. At the intersection of u_{*t} = 2 ms^{-1} for each material a corresponding vertical dotted line corresponds to grain size. Using the assumed density for fayalite (Figure 4.10C), the maximum density material we modeled, initial movement would occur at a grain size of medium sand (2.1 ϕ; Figure 4.10B, arrow 1) and grains with the lowest density, Kilauea sediment, (Figure 4.10D, arrow 2) are entrained as coarse sand (1.1 ϕ; 453 μm; Figure 4.9B), a range of ~1ϕ. Holding grain size constant at 250 μm (2 ϕ; Figure 4.10B, gashed line) u_{*t} increases with

increased density of material, as shown by $\Delta u_{*t} = 0.35$ ms^{-1} for fayalite (Figure 4.10B, arrow A) and Kilauea basalt (Figure 4.10A, arrow B).

The equivalence of olivine and basalt grains transported at $u_{*t} = 2$ ms^{-1}, shows how dramatic the grain-size differences can be when density varies. Conversely, for sediment of a specific grain size, the model shows the range of u_{*t} values needed to initiate sediment movement for materials of different densities, and shows that mineral separation, and thus compositional change, can easily occur in surface sediment eroded from a single rock source. Interpreted compositional and grain-size differences between potentially olivine enriched very fine sand compared to fine sand in the Edgar target of El Dorado in Gusev Crater [Sullivan et al., 2008] provides a direct demonstration of olivine concentration in ripples by aeolian action.

Under idealized conditions, lag deposits would become passively enriched in denser minerals (*e.g.*, olivine) while transported sediment would be enriched in less denser minerals (*e.g.*, plagioclase). However, plagioclase-enriched dunes are permissible but not expected. After the removal of olivine phenocrysts the remaining vesicular basaltic rock fragments become less dense. Low-density vesicular rock fragments would then become susceptible for transport resulting in olivine depleted landforms. With observations of active basaltic sand dunes [Chojnacki et al., 2011; Bridges et al., 2012] and the rarity of observed sediment transport events, density-sorted basaltic rock fragments may serve as the primary sediment source responsible for aeolian transport. Additionally, to maintain a constant grain-size of particles with different densities in motion, the necessary u_{*t} must increase with increasing density.

Figure 4.10. (A) Expressions [Shao and Lu, 2000] for the prediction of threshold friction velocity for sediment at Mars atmospheric conditions (6.1 mb). Differences in density between constituent minerals in Kilauea and Cima rock-derived sediments enable sorting of components. Dotted horizontal line denotes hydrodynamic equivalence at $u_{*t} = 2$ ms^{-1} for sediment grains and minerals with different densities, and corresponding grain sizes. (B) At $u_{*t} = 2$ ms^{-1} the entrainment for medium sand (2 ϕ) olivine grains, modeled as fayalite ($\rho_p = 4390$ kg m^{-3}) shown by arrow 1 is equivalent to entrainment for (C) Kilauea basalt derived coarse sand sediment ($\rho_p = 2601$ kg m^{-3}) shown by arrow 2. Differences in u_{*t} show potential for olivine (fayalite, arrow A) accumulation separated from Mars sand (Kilauea basalt, arrow B). See Table 4.A-7 for parameters.

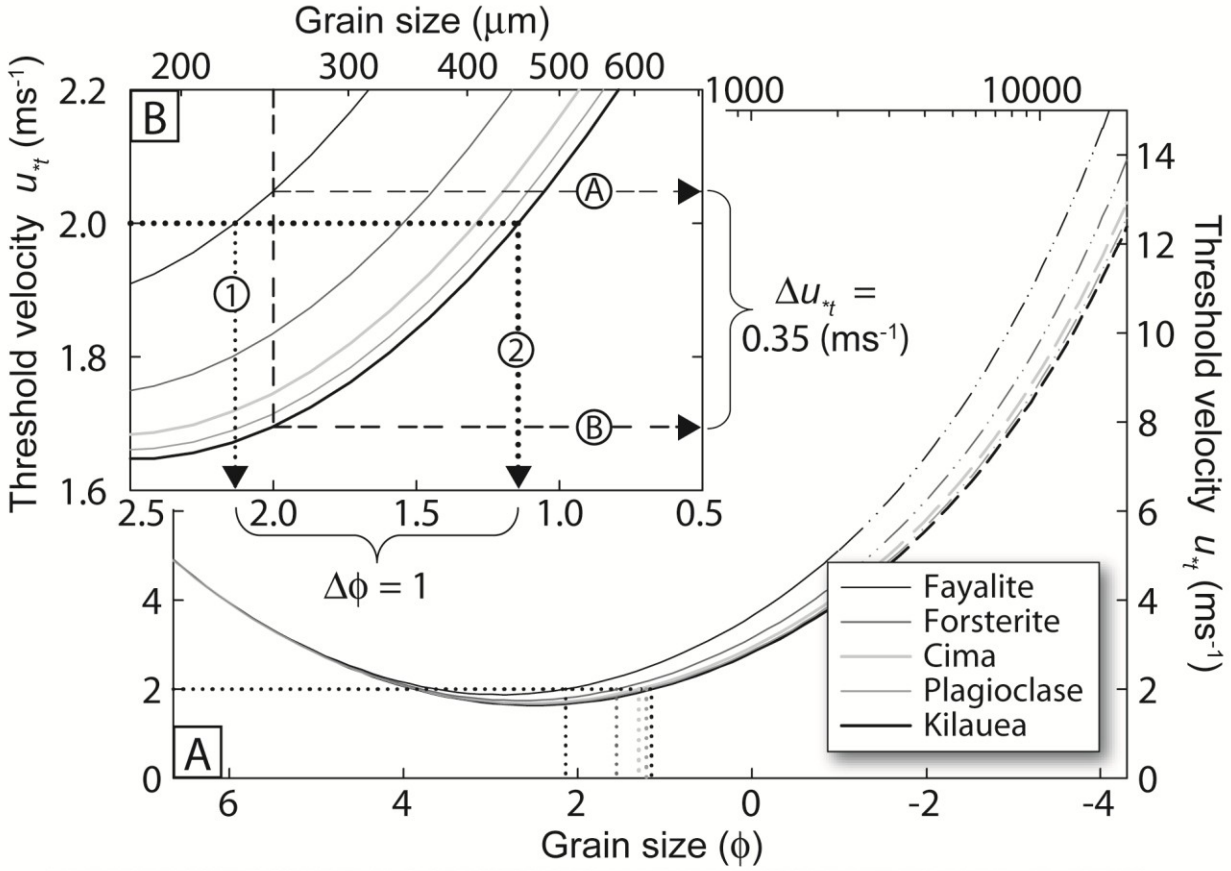
Grain size (μm)
200
300
400
500
600
1000
10000
Threshold velocity u_{*t} (ms^{-1})
2.2
2.0
1.8
1.6
B
A
1
2
Δu_{*t} = 0.35 (ms^{-1})
2.5
2.0
1.5
1.0
0.5
Δϕ = 1
14
12
10
8
6
4
2
0
Threshold velocity u_{*t} (ms^{-1})
Fayalite
Forsterite
Cima
Plagioclase
Kilauea
6
4
2
0
-2
-4
Grain size (ϕ)

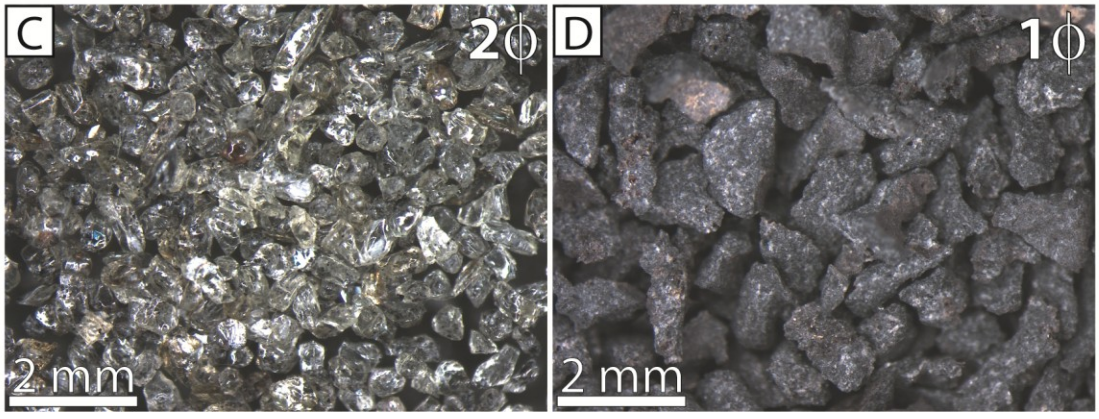
C
2ϕ
2 mm
D
1ϕ
2 mm

Models of threshold friction velocity [Shao and Lu, 2000] simplify particles as spherical objects. For non-spherical particles, the differences in shape (*i.e.,* compact, platy, bladed, and elongate) in addition to density, can affect the behavior of sediment transport, and are represented as aerodynamic diameter [Davies, 1979]. Here we simply the approach assuming spherical particles to allow direct comparison with prior experimental and theoretical studies [*e.g.,* Iversen and White, 1982; Shao and Lu, 2000; Bridges et al., 2010], but recognize the importance of aerodynamic differences of differently shaped particles in a natural setting.

8.2. Composition of Martian Sediments (Soils)

Chemistry results from sieved analog sediment provide a demonstration of concept for compositional variations generated from the redistribution of minerals, but do not show continued separation into mineral components as limited by the mechanics of the comminution and sieving experiment. Sediment exposed to sorting in a natural environment has the potential to generate a greater compositional range from the complete isolation and concentration of olivine, pyroxene, and feldspar end members are permissible. In such conditions, all combinations of compositions in A-CNK-FM plots parallel to the olivine-feldspar join are possible and are predicted. Soil sediment compositions on Mars are primarily controlled by variations in source rock and from sorting, as shown by the predominant compositional variation parallel to the olivine-feldspar join. Only deviations beyond physical sorting can be associated with other processes including chemical weathering. Due to the overwhelming similarities of soil compositions, the role of chemical weathering as the principal control of soils compositions is limited or, alternatively, isochemical weathering in a closed system occurs.

Given that aeolian transport is active on Mars, and combined with modeling the density separation of sediment components (Figure 4.10), the composition of sediments on Mars is therefore expected to have been modified. The degree of permissible sorting is clearly enhanced by diversity in source rock mineral densities, and in the abundance of phenocrysts in the source rock, as expected from terrestrial sorting studies [*e.g.* Nesbitt and Young, 1996; Young and Nesbitt, 1998]. Phenocrysts are present in some basaltic rocks at the MER landing site in Gusev Crater [McSween et al., 2006a] and in many Martian meteorites [McSween, 1985; Bridges and Warren, 2006]. The basaltic component in MER sediment compositions can be explained through mineral segregation by sorting and but do not specifically require significant chemical weathering and clay production. Soils also contain mixing of older chemically altered components [McSween et al., 2010; McGlynn et al., 2012]. Chemical weathering effects [*e.g.* Hurowitz and McLennan, 2007; Tosca et al., 2011] including clay production [*e.g.* Bishop et al., 2008] can only be considered beyond the scope of what physical processes are capable of generating.

9. Conclusions

Analog sediment from Cima and Kilauea mafic lavas were comminuted and sieved to generate sediment as a demonstration of concept compositional changes imposed by sieving. The resulting sediment compositions are controlled by the crystal-size distribution of the parent material, and the availability and redistribution of mineral species caused by sieving. Variations in sediment mineralogy derived from Kilauea basalt occurred from the concentration of olivine phenocrysts. Less significant partitioning of minerals occurred in sediment derived from the

aphanitic Cima basalt, which exhibited minor concentration of plagioclase, pyroxene, and olivine in fine sand. Major- and trace-element compositions diverge from expected source rock values. Olivine accumulation is paired with MgO, Fe_2O_3(T), Ni, and Co, and Al_2O_3 depletion. Trace elements are strongly controlled by accessory minerals. The effect of sieving on transition and REE chemistry is minor.

Cima trachybasalt and Kilauea basalt represent high- and low-alkali compositions, bracketing the composition of most rocks and soils in Gusev Crater, Mars. The ranges and trajectories of Cima and Kilauea analog sediments show similar patterns to Gusev sediments in a total alkalis versus silica diagram. Kilauea sediments also match the ranges and trajectories of Gusev and Meridiani sediments in A-CNK-FM plots. Such trends can be produced from the sorting of basaltic rock comminuted by impact or aeolian abrasion and do not require chemical weathering.

Aeolian transport modeling demonstrates the plausibility for density separation of minerals by selectively removing less-dense plagioclase and basalt clasts from denser grains of olivine, producing FeO_T+MgO-enriched lag deposits, consistent with soil observations in Gusev Crater. Results can also explain compositional variations in soils in Mars, including olivine rich sand dunes in Amazonis Planitia. This experimental approach demonstrates the capability of compositional modification of sediments by physical sorting, links igneous protolith textures with sediment compositions, and must be considered when interpreting the compositions and weathering pathways of sediments examined by the Mars rovers and landers.

10. Acknowledgments

We acknowledge discussions of aeolian transport with Devon Burr and assistance in electron microprobe analysis from Allan Patchen. This work was partly supported by a GSA Graduate Student Research Grant, a UT Development Award, and NASA Mars Exploration Rovers Cornell subcontract 39361-6446 to HYM.

References

Anderson, A. T., and Wright, T. L. (1972), Phenocrysts and glass inclusions and their bearing on oxidation and mixing of basaltic magmas, Kilauea Volcano, Hawaii, *Am. Mineral., 57*, 188-216.

Bagnold, R. A. (1941), *The Physics of Blown Sand and Desert Dunes*, 265 pp., Chapman and Hall, London.

Balme, M., Berman, D. C., Bourke, M. C., et al., (2008), Transverse Aeolian Ridges (TARs) on Mars, *Geomorphology. 101*, 703-720, doi:10.1016/j.geomorph.2008.03.011.

Baratoux, D., Mangold, N., Arnalds, O., et al. 2011. Origin of volcanic sands of Iceland, Earth Surf. Processes Landforms. doi:10.1002/esp.2201.

Batt, R.G. and Peabody, S.A. 1999. Threshold friction velocities for large pebble gravel beds. J. Geophys. Res. 104, 24273-24279, doi:10.1029/1999JD900484.

Bishop, J.L., Noe Doberea, E.Z., McKeown, N.K, et al. (2008), Phyllosilicate diversity and past aqueous activity revealed at Mawrth Vallis, *Mars. Science*. 321, 830-833, doi:10.1126/science.1159699.

Bridges, J. C. and Warren, P. H. (2006), The SNC meteorites: basaltic igneous processes on Mars. *J. Geol. Soc. London, 163*, 229-251, doi:10.1144/0016-764904-501.

Bridges, N. T., Geissler, P.E., McEwen, A. S., et al. (2007), Windy Mars: A dynamic planet as seen by the HiRISE camera. *Geophys. Res. Lett. 34*, L23205, doi:10.1029/2007GL031445.

Bridges, N. T., Banks, M. E., Beyer, R. A., et al. (2010), Aeolian bedforms, yardangs, and indurated surfaces in the Tharsis Montes as seen by the HiRISE Camera: Evidence for dust aggregates. *Icarus, 205*, 165-182, doi:10.1016/j.icarus.2009.05.017.

Bridges, N. T., Bourke, M. C., Geissler, P. E., et al. (2012), Planet-wide sand motion on Mars. *Geology, 40*, 31-34, doi:10.1130/G32373.1.

Burns, R. G. (1970), *Mineralogical applications of crystal field theory*. Cambridge University Press, Cambridge.

Chojnacki, M., Burr, D.M., Moersch, J.E., et al. (2011), Orbital observations of contemporary dune activity in Endeavor crater, Meridiani Planum, Mars. *J. Geophys. Res. 116*, E00F19, doi:10.1029/2010JE003675.

Cutts, J. A. and Smith, R. S. U. (1973), Eolian deposits and dunes on Mars. *J. Geophys. Res. 78*, 4139-4154, doi:10.1029/JB078i020p04139.

Davies, C. N. (1979), Particle-fluid interaction. *J. Aerosol. Sci., 10*, 477-513.

Dickinson, W. R. (1970), Interpreting detrital modes of greywacke and arkose. *J. Sed. Petrology, 40*, 695-707.

Ehlmann, B. L., Mustard, J. F., Murchie, S. L., et al. (2011), Identification of hydrated silicate minerals on Mars using MRO-CRISM: Geologic context near Nili Fossae and implications for aqueous alteration. *Nature, 479*, 53-60, doi:10.1029/2009je003339.

Ellehoj, M. D., Gunnlaugsson, H. P., Taylor, P. A., et al. (2010), Convective vortices and dust devils at the Phoenix Mars mission landing site. *J. Geophys. Res. 115*, E00E16, doi:10.1029/2009JE003413.

Farmer, G. L., Glazner, A. F., Wilshire, H. G., et al. (1995), Origin of late Cenozoic basalts at the Cima volcanic field, Mojave Desert, California, *J. Geophys. Res., 100*(B5), 8399–8415, doi:10.1029/95JB00070.

Fralick, P. W. (2003), Geochemistry of clastic sedimentary rocks: ratio techniques. In ed. D. Lentz, *Geochemistry of Sedimentary Rocks*. Geol. Assoc. Can.

Friedman, G. M. and Johnson, K. G. (1982), Exercises in Sedimentology. Wiley, New York.

Garcia, M. O., Rhodes, J. M., and Trusdell, F. A. (1996), Petrology of lavas from the Puu Oo eruption of Kilauea Volcano: III. The Kupaianaha episode (1986-1992). *Bull. Volcanol. 58*, 359-379.

Garcia, M. O., Pietruszka, A. J., Rhodes, J. M., et al. (2000), Magmatic processes during the prolonged Puu Oo eruption of Kilauea Volcano, Hawaii. *J. Petrol., 41*, 967-990.

Garcia, M. O., Pietruszka, A. J., Rhodes, J. M., et al. (2003), A petrologic perspective of Killauea Volcano's summit magma reservoir. *J. Petrol., 44*, 2313-2339.

Gellert, R., Rieder, R., Anderson, R. C., et al. (2004), Chemistry of rocks and soils in Gusev Crater from the Alpha Particle X-ray Spectrometer. *Science, 305*, 829-832, doi:10.1126/science.1099913.

Gellert, R., Rieder, R., Brückner, J., et al. (2006), Alpha Particle X-Ray Spectrometer (APXS): Results from Gusev crater and calibration report. *J. Geophys. Res, 111*, E02S05, doi:10.1029/2005JE002555.

Greeley, R. and Iversen J. D. (1985), *Wind as a geological process on Earth, Mars, Venus and Titan.* Cambridge University Press, Cambridge.

Greeley, R., Skypeck, A., and Pollack, J. B. (1993), Martian aeolian features and deposits - Comparisons with general circulation model results. *J. Geophys. Res, 98,* 3183-3196.

Greeley, R., Kraft, M., Sullivan, R., et al. (1999), Aeolian features and processes at the Mars Pathfinder landing site. *J. Geophys. Res. 104*, 8573-8584, doi:10.1029/98JE02553.

Greeley, R., Squyres, S.W., Arvidson, R.E., et al. (2004), Wind-related processes detected by the Spirit rover at Gusev Crater, Mars. *Science. 305*, 810-813, doi:10.1126/science.1100108.

Greeley, R., Arvidson, R.E., Barlett, P.W., et al. (2006a), Gusev crater: Wind-related features and processes observed by the Mars Exploration Rover Spirit. *J. Geophys. Res. 111*, E02S09, doi:10.1029/2005JE002491.

Greeley, R., Whelley, P. L., Arvidson, R. E., et al. (2006b), Active dust devils in Gusev crater, Mars: Observations from the Mars Exploration Rover Spirit. *J. Geophys. Res. 111*, E12S09, doi:10.1029/2006JE002743.

Greeley, R., Waller, D.A., Cabrol, N.A., et al. (2010), Gusev Crater, Mars: Observations of three dust devil seasons. *J. Geophys. Res. 115*, E00F02, doi:10.1029/ 2010JE003608.

Grotzinger, J.P., Beaty, D., Dromat, G. et al., (2011), The sedimentary record of Mars. *The Sed. Rec.*, *9*, 4-8, doi:10.2110/sedred.2011.2.

Hansen, C. J., Bourke, M., Bridges, N. T. et al. (2011), Seasonal erosion and restoration of Mars' northern polar dunes, Science, 331, 575-578, doi:10.1126/science.1197636.

Hurowitz, J. A. and McLennan, S. M. (2007), A ~3.5 Ga record of water-limited, acidic weathering conditions on Mars. *Earth Planet. Sc. Lett. 260*, 432-443, doi:10.1016/j.epsl.2007.05.043.

Ingersoll, R. V., Bullard, T. F., Ford, R. L., et al. (1984), The effect of grain size on detrital modes: A test of the Gazzi-Dickinson point-counting method. *J. Sed. Petrology, 54*, 103-116.

Iversen, J.D. and White, B.R. (1982), Saltation threshold on Earth, Mars and Venus. *Sedimentology, 29*, 111-119, doi: 10.1111/j.1365-3091.1982.tb01713.x.

King, E. A. (1977), The lunar regolith: Physical characteristics and dynamics. *Phil. Trans. R. Soc. Lond. A. 285*, 273-278, doi: 10.1098/rsta.1977.0065.

Kittleman, L. R. (1964), Application of Rosin's distribution in size-frequency analysis of clastic rocks. *J. Sed. Petrology, 34*, 483-502.

Koeppen, W.C. and Hamilton, V. E. (2008), Global distribution, composition, and abundance of olivine on the surface of Mars from thermal infrared data. *J. Geophys. Res. 113*, E05001, doi:10.1029/2007JE002984.

Kok, J. F. (2010), Difference in the wind speeds required for initiation versus continuation of sand transport on Mars: Implications for dunes and dust storms, *Phys. Rev. Lett. 104*, 074502, doi:10.1103/PhysRevLett.104.074502.

Kuenen, P.H. (1964), Experimental abrasion: 6 Surf action. *Sedimentology. 3*, 29-43, doi:10.1111/j.1365-3091.1964.tb00273.x.

Lancaster, N. Nickling, W. G., Gillies, J. A. (2010), Sand transport by wind on complex surfaces: Field studies in the McMurdo Dry Valleys, Antarctica. *J. Geophys. Res. 115*, F03027, doi:10.1029/2009JF001408.

Lewis, D. W. (1984), *Practical Sedimentology*. Hutchinson & Ross. Stroudsburg.

Mangold, N., Poulet, F., Mustard, J. F., et al. (2007), Mineralogy of the Nili Fossae region with OMEGA/Mars Express data: 2. aqueous alteration of the crust. *J. Geophys. Res. 112*, E08S04, doi:10.1029/2006JE002835.

Mangold, N., Baratoux, D., Arnalds, O., et al. (2011), Segregation of olivine grains in volcanic sands in Iceland and implications or Mars. *Earth Planet. Sc. Lett. 310*, 233-243, doi:10.1016/j.epsl.2011.07.025.

McDonough, W.F. and Sun, S., (1995), The composition of the Earth. *Chem. Geol. 120*, 223-254, doi:10.1016/0009-2541(94)00140-4.

McGlynn, I. O., Okin, G. S., Hartman, L. J., et al. (2005), The Importance of Spatial Connectivity in Wind Erosion. *American Geophysical Union Fall Meeting*, abstract #P13B-0156.

McGlynn, I. O., McSween, H. Y., and Fedo, C. M. (2008), Textural and chemical evidence of hydrodynamic sorting in sediments in Gusev crater, Houston, Texas, Lunar and Planetary Institute, *Lunar and Planetary Science Conference XXXIX*, abstract 1332.

McGlynn, I. O., Fedo, C. M. and, McSween, H. Y. (2011), Origin of basaltic soils at Gusev crater, Mars, by aeolian modification of impact-generated sediment. *J. Geophys. Res. 116*, E00F22, doi: 10.1029/2010JE003712.

McGlynn, I.O., Fedo, C.M. and, McSween, H.Y. (2012), Soil mineralogy at the Mars Exploration Rover landing sites: An assessment of the competing roles of physical sorting and chemical weathering. *J. Geophys. Res. 117*, E01006, doi:10.1029/ 2011JE003861.

McManus, J. (1988), Grain size determination and interpretation. In ed. M. Tucker, *Techniques in Sedimentology*, Blackwell Scientific Publications, Palo Alto.

Mckenna Neuman, C. (2003), Effects of temperature and humidity upon the entrainment of sedimentary particles by wind. *Bound.-Lay. Meteorol. 108*, 61-89, doi:10.1023/A:1023035201953.

McLennan, S. M. (1993), Weathering and global denudation. *J. Geol. 101*, 295-303.

McLennan, S. M. (2000), Chemical composition of Martian soil and rocks: Complex mixing and sedimentary transport, *Geophys. Res. Lett., 27*, 1335-1338.

McSween, H. Y. (2010), Martian rock and soil compositions from orbit and the ground: Why can't we all just get along?, Houston, Texas, Lunar and Planetary Institute, *Lunar and Planetary Science Conference XLI*, abstract 1105.

McSween H. Y. and Keil K. (2000), Mixing relationships in the Martian regolith and the composition of globally homogeneous dust. *Geochim. Cosmochim. Ac. 64*, 2155-2166, doi: 10.1016/S0016-7037(99)00401-9.

McSween, H. Y., Grove, T. L., Wyatt, M.B. (2003), Constraints on the composition and petrogenesis of the Martian crust. *J. Geophys. Res. 108*, 5135, doi:10.1029/2003JE002175.

McSween, H. Y., Arvidson, R.E., Bell, J.F., et al. (2004), Basaltic rocks analyzed by the Spirit rover in Gusev Crater. *Science. 305*, 842-845, doi:10.1126/science.3050842.

McSween, H. Y., Wyatt, M.B., Gellert. R., et al. (2006a), Characterization and petrologic interpretation of olivine-rich basalts at Gusev Crater, Mars. *J. Geophys. Res. 111*, E02S10, doi:10.1029/2005JE002477.

McSween H. Y., Ruff S.W., Morris R.V., et al. (2006b), Alkaline volcanic rocks from the Columbia Hills, Gusev Crater, Mars. *J. Geophys. Res. 111*, E09S91, doi:10.1029/2006JE002698.

McSween H. Y., Ruff, S.W., Morris, R.V., et al. (2008), Mineralogy of volcanic rocks in Gusev Crater, Mars: Reconciling Mossbauer, Alpha Particle X-ray Spectrometer, and Miniature Thermal Emission Spectrometer spectra. *J. Geophys. Res. 113*, E06S04, doi:10.1029/2007JE002970.

McSween, H. Y., Taylor, G. J., Wyatt, M. B. (2009), Elemental composition of the Martian crust. *Science. 324*, 736-739, doi:10.1126/science. 1165871.

McSween, H.Y., McGlynn, I. O., and Rogers, A. D., (2010), Determining the modal mineralogy of Martian soils. *J. Geophys. Res. 115*, E00F12, doi:10.1029/2010JE003582.

Nesbitt, H.W. and Wilson, R.E. (1992), Recent chemical weathering of basalts. *Am. J. Sci. 292*, 740-777.

Nesbitt, H.W. and Young, G.M. (1982), Early Proterozoic climates and plate motions inferred from major element chemistry of lutites. *Nature. 299*, 715 – 717, doi:10.1038/299715a0.

Nesbitt, H.W. and Young, G.M. (1989), Formation and Diagenesis of Weathering Profiles. *J. Geol. 97*, 129-147.

Nesbitt, H.W. and Young, G.M. (1996), Petrogenesis of sediments in the absence of chemical weathering: Effects of abrasion and sorting on bulk composition and mineralogy. *Sedimentology. 43*, 341-358, doi:10.1046/j.1365-3091.1996.d01-12.x.

Nesbitt, H.W., Young, G.M., McLennan, S.M., et al. (1996), Effects of chemical weathering and sorting on the petrogenesis of siliciclastic sediments, with implications for provenance studies. *J. Geol. 104*, 525-542.

Norman, M., Garcia, M. O., and Pietruszka, J. (2005), Trace-element distribution coeffi cients for pyroxenes, plagioclase, and olivine in evolved tholeiites from the 1955 eruption of Kilauea Volcano, Hawai'i, and petrogenesis of differentiated rift-zone lavas, *Am. Mineral., 90*, 888-899.

Okin, G. S., Parsons, A. J., Wainwright, J. et al., (2009), Do changes in connectivity explain desertification? *BioScience. 59*, 237-244.

Owen, P. R. (1964), Saltation of uniform grains in air, *J. Fluid Mech., 20*, 225-242, doi:10.1017/S0022112064001173.

Raupach, M. R., Gillette, D. A., Leys, J. F. (1993), The effect of roughness elements on wind erosion threshold. *J. Geophys. Res. 98*, 3023-3029, doi:10.1029/92JD01922.

Ravi, S., D'Odorico, P., Over, T. M., et al. (2004), On the effect of air humidity on soil susceptibility to wind erosion: The case of air-dry soils. *Geophys. Res. Lett. 31*, L09501, doi:10.1029/2004GL019485.

Roberts, W. L., Rapp, G. R., and Weber, J. (1993), *Encyclopedia of minerals*, Van Nostrand Reinhold Company, New York.

Rieder, R., Gellert, R., Brückner, J., et al. (2003), The new Athena alpha particle X-ray spectrometer for the Mars Exploration Rovers, *J. Geophys. Res., 108*(E12), 8066, doi:10.1029/2003JE002150.

Rieder, R., Gellert, R., Anderson, R.C., et al. (2004), Chemistry of Rocks and Soils at Meridiani Planum from the Alpha Particle X-ray Spectrometer. *Science, 306*, 1746-1749, doi:10.1126/science.1104358.

Rieu, R., Allen, P. A., Plotze, M., and Pettke, T. (2007), Compositional and mineralogical variations in a Neoproterozoic glacially influenced succession, Mirbat area, south Oman: Implications for paleoweathering conditions, Precambrian Res., 154, 248-265, doi:10.1016/j.precamres.2007.01.003.

Shao Y.P. and Lu, H. (2000), A simple expression for wind erosion threshold friction velocity. *J. Geophys. Res. 105*, 22437-22443, doi:10.1029/2000JD900304.

Silvestro, S., Fenton, L. K., Vaz, D.A., Bridges, N.T., and Ori, G.G. (2010), Ripple migration and dune activity on Mars: Evidence for dynamic processes, *Geophys. Res. Lett., 37*, L20203, doi:10.1029/2010GL044743.

Smith, P. H. and Lemmon, M. (1999). Opacity of the Martian atmosphere measured by the Imager for Mars Pathfinder. J. Geophys. Res. 104, 8975-8985, doi:10.1029/1998JE900017.

Stockstill-Cahill, K. R., Hamilton, W. E., and Anderson, F. S. (2009), A study of intracrater lowalbedo deposits within Amazonis Planitia craters: Evidence for locally-derived ultramafic to mafic materials, *J. Geophys. Res. 113*(E7), doi:10.1029/2007JE003036.

Sullivan, R., Greeley, R., Kraft, M., et al. (2000), Results of the Imager for Mars Pathfinder windsock experiment, *J. Geophys. Res., 105*(E10), 24,547–24,562, doi:10.1029/1999JE001234.

Sullivan, R., Banfield, D., Bell, J. F., et al. (2005), Aeolian processes at the Mars Exploration Rover Meridiani Planum landing site, *Nature, 436*, 58-61, doi: 10.1038/nature03641.

Sullivan, R., Arvidson, R. Bell, J. F., et al. (2008), Wind-driven particle mobility on mars: Insights from Mars Exploration Rover observations at "El Dorado" and surroundings at Gusev Crater. *J. Geophys. Res. 113*, E06S07, doi:10.1029/2008JE003101.

Taylor, G., Boynton, V., and Brueckner, J. (2006), Bulk composition and early differentiation of Mars. *J. Geophys. Res., 111*, E03S10, doi:10.1029/2005JE002645.

Taylor, L. A., Pieters, C. M., Keller, L. P., et al. (2001), Lunar Mare Soils: Space weathering and the major effects of surface-correlated nanophase Fe. *J. Geophys. Res. 106*, E11, 27,985-27,999.

Taylor, L. A., Pieters, C. M., Patchen, A., et al. (2010), Mineralogical and chemical characterization of lunar highland soils: Insights into the space weathering of soils on airless bodies. *J. Geophys. Res., 115*, E02002, doi:10.1029/2009JE003427.

Tosca, N.J., McLennan, S.M., Lindsley, D.H. et al. (2004), Acid-sulfate weathering of synthetic Martian basalt: The acid fog model revisited. *J. Geophys. Res. 109*, E05003, doi:10.1029/2003JE002218.

Tosca, N. J., McLennan, S. M. Lamb, M. P., and Grotzinger, J. P. (2011), Physicochemical properties of concentrated Martian surface waters, *J. Geophys. Res., 116*, E05004, doi:10.1029/2010JE003700.

Wells, S. G., Dohrenwend, J. C., McFadden, L. D. (1985), Late Cenozoic landscape evolution on lava flow surfaces of the Cima volcanic field, Mojave Desert, *California. Geol. Soc. Am. Bull. 96*, 1518-1529, doi:10.1130/0016-7606(1985)96<1518:LCLEOL>2.0.CO;2.

Young G. M. and Nesbitt, H. W. (1998), Processes controlling the distribution of Ti and Al in weathering profiles, siliciclastic sediments and sedimentary rocks. *J. Sediment. Res., 68*, 448–455.

Zimbelman, J. R. (2010), Transverse Aeolian Ridges on Mars: First results from HiRISE images. *Geomorphology. 121*, 22-29, doi:10.1016/j.geomorph.2009.05.012.

Appendix

Table 4.A-1. Modal mineralogy point-counting results for rock samples and for mineral and lithic fragment results for analog sediments.

	Grain size			Mineralogy (%)					
Sample	ϕ	μm	Counts	Olivine	Plagioclase	Pyroxene	Oxides	Lithic fragments	Interparticle void space (%)
Cima	rock		1000	15	35	34	16		
Cima	-1	2000	1069	0	0	0	0	100	46
Cima	0	1000	1000	0	0	0	0	100	46
Cima	1	500	1041	1	0	0	0	99	52
Cima	2	250	1000	2	0	0	1	97	41
Cima	3	125	1000	7	2	0	1	89	36
Cima	4	62.5	1000	12	6	2	3	79	40
Cima	>4	<62.5	1002	26	11	2	5	56	46
Kilauea	rock		1010	10	36	29	25		
Kilauea	-1	2000	1155	0	0	0	0	100	53
Kilauea	0	1000	1036	7	0	0	0	93	53
Kilauea	1	500	1046	16	0	0	0	84	50
Kilauea	2	250	1232	38	0	0	0	62	47
Kilauea	3	125	1203	27	0	0	0	73	39
Kilauea	4	62.5	1123	29	0	0	0	70	39
Kilauea	>4	<62.5	1010	18	1	2	1	78	42

Table 4.A-2. Major element oxides for Cima and Kilauea rocks and derived sediments.

Sample (ϕ)	SiO_2	Al_2O_3	Fe_2O_3(T)	MnO	MgO	CaO	Na_2O	K_2O	TiO_2	P_2O_5	LOI	Total
Cima												
rock	47.61	16.55	11.35	0.181	6.36	8.32	4.24	2.11	2.685	0.68	0.16	100.20
-1.5	47.45	16.42	11.08	0.175	6.25	8.05	4.32	2.15	2.668	0.70	0.05	99.31
-1.0	47.68	16.63	11.37	0.180	6.32	8.37	4.18	2.10	2.708	0.71	0.09	100.30
-0.5	47.83	16.65	11.30	0.178	6.29	8.08	4.31	2.16	2.710	0.71	0.22	100.40
0.0	47.85	16.64	11.42	0.179	6.26	8.21	4.30	2.15	2.725	0.70	0.18	100.60
0.5	47.52	16.48	11.38	0.179	6.30	8.25	4.21	2.11	2.704	0.71	0.18	100.00
1.0	47.22	16.31	11.34	0.179	6.19	8.30	4.12	2.08	2.700	0.71	0.2	99.34
1.5	47.22	16.03	11.55	0.181	6.27	8.33	4.13	2.05	2.678	0.68	0.29	99.40
2.0	47.31	16.03	11.83	0.184	6.64	8.23	4.18	2.08	2.661	0.69	0.19	100.00
2.5	47.05	15.48	12.32	0.189	7.20	8.13	4.00	2.00	2.590	0.66	0.18	99.80
3.0	46.89	15.36	12.55	0.196	7.66	8.03	3.98	1.98	2.586	0.65	0.12	100.00
3.5	45.98	15.12	12.43	0.198	7.34	8.19	3.97	1.91	2.649	0.67	0.25	98.69
4.0	46.94	15.88	12.59	0.201	6.98	8.30	4.00	1.97	2.668	0.66	0.44	100.60
>4.0	47.83	17.05	10.68	0.175	5.13	8.86	4.22	2.06	2.564	0.68	1.09	100.30
Kilauea												
rock	48.41	11.46	12.48	0.168	12.49	9.91	1.91	0.48	2.321	0.23	-0.69	99.17
-1.5	49.04	11.68	12.62	0.171	12.10	10.22	1.98	0.49	2.387	0.24	-0.68	100.20
-1.0	48.80	11.72	12.50	0.169	11.87	10.20	1.98	0.49	2.371	0.23	-0.64	99.70
-0.5	49.43	12.18	12.65	0.170	11.27	10.44	2.04	0.51	2.489	0.25	-0.63	100.80
0.0	48.90	11.79	12.59	0.169	12.01	10.13	1.99	0.50	2.424	0.24	-0.68	100.10
0.5	48.27	11.16	12.67	0.170	14.05	9.62	1.86	0.47	2.287	0.23	-0.66	100.10
1.0	47.11	9.74	12.82	0.169	18.31	8.29	1.62	0.41	1.984	0.20	-0.76	99.90
1.5	47.02	8.98	12.98	0.169	20.83	7.36	1.53	0.39	1.803	0.18	-0.73	100.50
2.0	46.69	8.75	13.32	0.172	21.51	7.24	1.48	0.37	1.768	0.18	-0.73	100.70
2.5	46.03	8.60	13.45	0.173	21.24	7.22	1.42	0.36	1.738	0.18	-0.77	99.64
3.0	45.89	8.68	13.81	0.176	21.05	7.39	1.43	0.36	1.774	0.22	-0.78	100.00
3.5	45.98	8.93	13.84	0.176	19.54	7.69	1.50	0.38	1.846	0.19	-0.66	99.42
4.0	45.95	9.56	13.72	0.176	17.57	8.13	1.60	0.42	1.955	0.19	-0.66	98.61
>4.0	47.89	11.25	12.94	0.171	13.14	9.92	1.92	0.46	2.165	0.21	-0.53	99.54
Detection Limit	0.01	0.01	0.01	0.001	0.01	0.01	0.01	0.01	0.001	0.01		

Concentrations in wt. %, detection by fusion inductively coupled plasma (FUS-ICP).

Table 4.A-3. Trace element analyses of Cima and Kilauea rocks and derived sediments.

				Cima (ϕ)												
	Method	Detection Limit	rock	-1.5	-1	-0.5	0	0.5	1	1.5	2	2.5	3	3.5	4	>4
Sc	1	1	19	19	19	19	19	19	19	19	19	19	19	18	19	18
Be	1	1	2	2	2	2	2	2	2	2	2	2	2	2	2	2
V	1	5	222	220	221	222	224	224	223	222	223	216	218	318	224	211
Cr	2	20	100	100	100	100	100	100	100	110	110	120	120	120	130	120
Co	2	1	38	38	39	39	39	38	38	39	40	43	44	44	42	33
Ni	3	1	91	83	87	85	84	85	85	88	98	122	123	111	108	83
Cu	3	1	31	21	27	26	30	30	28	29	42	36	36	39	50	81
Zn	3	1	80	70	77	75	77	78	78	78	79	76	80	80	84	87
Cd	3	0.5	0.7	0.5	0.7	0.6	0.7	0.6	0.6	0.5	0.6	0.6	0.7	0.6	0.8	1
S	3	0.001	0.018	0.011	0.013	0.013	0.017	0.014	0.014	0.014	0.017	0.013	0.014	0.016	0.022	0.042
Ga	2	1	23	23	23	23	23	23	23	23	23	23	22	23	23	24
Ge	2	0.5	1.9	1.9	1.9	1.9	1.9	1.9	2	2	2.1	2	1.9	2.2	2	1.9
As	2	5	< 5	< 5	< 5	< 5	< 5	< 5	< 5	< 5	< 5	< 5	< 5	< 5	< 5	6
Rb	2	1	43	42	42	42	41	42	42	41	41	40	39	40	41	42
Sr	1	2	667	653	670	669	664	659	654	645	653	630	626	614	665	732
Y	2	0.5	30.3	28.8	29.2	28.9	28.8	29.2	29.8	29.3	29.5	28.6	27.8	28.7	28.7	30
Zr	2	1	373	358	366	362	362	361	368	361	363	356	339	349	345	359
Nb	2	0.2	62.8	61.9	62.8	62.4	62.5	61.9	62.3	61.6	62.1	59.9	58	59.6	58.4	59.8
Mo	2	2	4	5	4	4	4	4	4	4	5	5	5	5	5	6
Ag	1	0.3	0.4	< 0.3	< 0.3	< 0.3	0.3	0.4	< 0.3	< 0.3	0.3	< 0.3	< 0.3	< 0.3	0.5	1.8
In	2	0.1	< 0.1	< 0.1	< 0.1	< 0.1	< 0.1	< 0.1	< 0.1	< 0.1	< 0.1	< 0.1	< 0.1	< 0.1	< 0.1	< 0.1
Sn	2	1	3	3	3	4	3	3	3	4	4	4	4	4	5	7
Sb	2	0.2	0.4	0.3	0.4	0.4	0.4	0.5	0.4	0.5	0.6	0.6	0.6	0.7	0.7	1.6
Cs	2	0.1	0.5	0.5	0.6	0.6	0.5	0.5	0.5	0.5	0.6	0.5	0.5	0.5	0.6	0.7
Ba	1	3	367	360	364	366	370	367	365	364	363	354	348	335	355	390
La_N/Yb_N				1.01	0.98	1.03	1.03	1.02	0.99	1.04	1.03	1	1	0.99	0.99	1.03
La_N/Sm_N				1.05	1.02	1.01	1.03	1.02	1.03	1.01	1.01	1.03	1.03	1.01	1	1
Gd_N/Yb_N				1	0.99	1.02	1.02	1.04	1.01	1.08	1.02	1.04	1.01	1	1.02	1.01

Table 4.A-3. (continued)

			Kilauea (ϕ)													
	Method	Detection Limit	rock	-1.5	-1	-0.5	0	0.5	1	1.5	2	2.5	3	3.5	4	>4
Sc	1	1	28	30	29	31	30	28	25	24	23	23	23	24	24	29
Be	1	1	< 1	< 1	< 1	< 1	< 1	< 1	< 1	< 1	< 1	< 1	< 1	< 1	< 1	< 1
V	1	5	295	302	302	309	301	283	246	225	224	219	224	235	250	289
Cr	2	20	860	820	840	810	850	830	970	1120	1170	1260	1330	1420	1460	1310
Co	2	1	61	61	61	67	64	65	84	91	92	92	89	87	82	66
Ni	3	1	423	385	380	338	377	521	761	956	986	973	946	871	734	467
Cu	3	1	90	88	97	123	74	67	69	81	83	87	98	111	121	137
Zn	3	1	82	81	80	83	81	81	75	82	82	81	81	84	84	91
Cd	3	0.5	1	0.6	0.6	0.7	0.5	0.5	< 0.5	1	0.6	0.6	1.1	< 0.5	< 0.5	0.9
S	3	0.001	0.002	0.003	0.003	0.005	0.002	0.001	< 0.001	0.001	0.002	0.003	0.002	0.003	0.003	0.004
Ga	2	1	20	21	21	21	21	19	17	16	15	15	15	16	17	19
Ge	2	0.5	2.3	2.3	2.3	2.3	2.4	2	2.1	2	2.1	2.1	2.1	2.3	2.2	2.3
As	2	5	< 5	< 5	< 5	< 5	< 5	< 5	< 5	< 5	< 5	< 5	< 5	< 5	< 5	< 5
Rb	2	1	10	10	10	10	10	9	8	7	7	7	7	8	8	9
Sr	1	2	337	349	345	357	346	324	283	259	251	243	247	256	275	329
Y	2	0.5	21.4	22.3	22.1	23.1	22.3	19.8	17.9	16.1	15.7	15.5	15.6	16.5	17.8	19.4
Zr	2	1	161	169	169	174	166	149	134	131	122	117	118	127	135	145
Nb	2	0.2	16.1	16.8	16.8	17.4	16.7	15	13.4	12.3	11.7	11.4	11.5	12.5	13.4	14.3
Mo	2	2	< 2	< 2	< 2	< 2	< 2	< 2	< 2	< 2	< 2	< 2	2	2	3	4
Ag	1	0.3	< 0.3	< 0.3	< 0.3	0.3	< 0.3	< 0.3	< 0.3	< 0.3	< 0.3	< 0.3	< 0.3	0.4	0.3	0.4
In	2	0.1	< 0.1	< 0.1	< 0.1	< 0.1	< 0.1	< 0.1	< 0.1	< 0.1	< 0.1	< 0.1	< 0.1	< 0.1	< 0.1	< 0.1
Sn	2	1	2	2	2	2	2	2	2	2	2	2	2	9	4	5
Sb	2	0.2	0.4	0.3	0.3	0.4	0.4	0.4	0.4	0.4	0.3	0.4	0.4	0.5	0.6	0.7
Cs	2	0.1	< 0.1	0.1	0.1	0.1	0.1	< 0.1	< 0.1	< 0.1	< 0.1	< 0.1	< 0.1	< 0.1	< 0.1	0.1
Ba	1	3	127	133	133	136	133	124	108	100	97	96	98	102	108	118
La_N/Yb_N				1.16	1.03	0.99	0.95	1.04	1.03	1.02	0.98	0.95	0.96	1.01	0.96	0.97
La_N/Sm_N				1.11	1	0.93	1	0.98	0.98	0.97	0.96	0.97	0.96	1.02	1.01	0.94
Gd_N/Yb_N				1.06	1.06	1	0.95	1.07	1.05	1.03	1.02	0.97	0.99	1.03	0.98	1.04

Concentrations in ppm, S in wt. %. Analytical methods are 1, fusion inductively coupled plasma (FUS-ICP); 2, fusion inductively coupled mass spectrometry; 3, total digestion inductively coupled plasma (TD-ICP).

Table 4.A-4. Rare earth element analyses of Cima and Kilauea rocks and derived sediments.

Sample (ϕ)	La	Ce	Pr	Nd	Sm	Eu	Gd	Tb	Dy	Ho	Er	Tm	Yb	Lu	Hf	Ta	W	Tl	Pb	Bi	Th	U
Method	2	2	2	2	2	2	2	2	2	2	2	2	2	2	2	2	2	2	3	2	2	2
Cima																						
rock	35.9	71.7	8.25	34.1	7.53	2.45	6.67	1.05	5.89	1.08	2.90	0.402	2.53	0.394	6.5	4.33	< 0.5	0.06	10	< 0.1	4.91	1.54
-1.5	37.0	74.3	8.51	35.0	7.41	2.46	6.78	1.11	5.93	1.10	2.98	0.409	2.58	0.413	6.7	4.39	< 0.5	< 0.05	< 3	< 0.1	4.82	1.51
-1.0	36.0	72.8	8.29	34.5	7.41	2.50	6.73	1.09	6.04	1.10	2.96	0.421	2.58	0.404	6.5	4.35	< 0.5	0.06	< 3	< 0.1	4.95	1.52
-0.5	36.2	72.3	8.23	34.6	7.51	2.40	6.67	1.09	5.87	1.07	2.95	0.413	2.48	0.402	6.5	4.33	< 0.5	0.06	< 3	< 0.1	4.95	1.53
0.0	35.7	70.7	8.07	33.7	7.28	2.41	6.58	1.05	5.81	1.09	2.87	0.411	2.44	0.399	6.6	4.30	< 0.5	< 0.05	< 3	< 0.1	4.84	1.51
0.5	36.3	72.3	8.30	34.3	7.44	2.43	6.88	1.09	5.87	1.09	2.91	0.414	2.50	0.403	6.5	4.35	< 0.5	< 0.05	< 3	< 0.1	4.93	1.52
1.0	36.0	72.1	8.25	34.2	7.35	2.42	6.81	1.10	5.85	1.08	2.93	0.407	2.57	0.394	6.6	4.35	< 0.5	0.06	5	< 0.1	4.93	1.49
1.5	36.3	72.9	8.40	34.8	7.51	2.48	6.95	1.11	5.95	1.09	3.03	0.413	2.45	0.407	6.5	4.30	< 0.5	0.05	4	< 0.1	5.00	1.56
2.0	36.2	72.3	8.37	34.3	7.50	2.41	6.67	1.08	5.87	1.10	2.97	0.413	2.48	0.400	6.5	4.28	< 0.5	0.05	5	< 0.1	4.95	1.51
2.5	34.5	69.4	8.04	33.1	7.03	2.35	6.68	1.03	5.70	1.04	2.79	0.390	2.44	0.387	6.4	4.13	< 0.5	0.06	8	< 0.1	4.78	1.51
3.0	33.8	68.5	7.84	32.3	6.85	2.30	6.38	1.01	5.51	1.01	2.75	0.399	2.39	0.380	6.2	3.99	< 0.5	0.06	13	0.1	4.65	1.43
3.5	35.0	70.4	8.04	33.2	7.24	2.37	6.55	1.06	5.75	1.06	2.87	0.399	2.49	0.399	6.3	4.09	< 0.5	0.08	18	0.1	4.77	1.50
4.0	34.3	70.3	7.99	33.2	7.19	2.34	6.57	1.04	5.72	1.04	2.85	0.389	2.44	0.397	6.2	3.98	< 0.5	0.08	35	0.2	4.70	1.46
>4.0	36.3	75.1	8.33	34.3	7.62	2.43	6.66	1.06	5.84	1.07	2.85	0.408	2.49	0.405	6.5	4.16	< 0.5	0.11	133	0.6	5.11	1.57

Table 4.A-4. (Continued).

Sample (ϕ)	La	Ce	Pr	Nd	Sm	Eu	Gd	Tb	Dy	Ho	Er	Tm	Yb	Lu	Hf	Ta	W	Tl	Pb	Bi	Th	U
Method	2	2	2	2	2	2	2	2	2	2	2	2	2	2	2	2	2	2	3	2	2	2
Kilauea																						
rock	12.9	30.6	4.07	18.7	4.67	1.61	4.57	0.77	4.23	0.76	2.03	0.279	1.65	0.244	3.3	1.14	< 0.5	< 0.05	< 3	< 0.1	1.13	0.40
-1.5	15.5	34.2	4.38	20.3	5.07	1.74	5.04	0.82	4.52	0.83	2.20	0.305	1.71	0.278	3.7	1.20	< 0.5	< 0.05	< 3	< 0.1	1.17	0.40
-1.0	13.8	32.7	4.48	20.4	5.02	1.78	5.04	0.84	4.43	0.83	2.19	0.305	1.71	0.267	3.5	1.23	< 0.5	< 0.05	< 3	< 0.1	1.19	0.43
-0.5	13.8	33.2	4.47	20.7	5.36	1.72	4.96	0.84	4.58	0.84	2.25	0.299	1.79	0.269	3.7	1.23	< 0.5	< 0.05	< 3	< 0.1	1.24	0.42
0.0	13.7	32.6	4.36	20.6	4.95	1.76	4.84	0.79	4.42	0.81	2.15	0.292	1.84	0.262	3.6	1.20	< 0.5	< 0.05	5	< 0.1	1.20	0.43
0.5	12.5	29.8	3.98	18.6	4.63	1.56	4.56	0.77	4.02	0.75	1.97	0.261	1.54	0.247	3.2	1.12	< 0.5	< 0.05	6	< 0.1	1.09	0.38
1.0	11.1	26.1	3.53	16.3	4.08	1.41	4.01	0.66	3.64	0.66	1.74	0.238	1.38	0.206	2.8	0.97	5.2	< 0.05	< 3	< 0.1	0.94	0.34
1.5	10.1	23.9	3.22	14.7	3.76	1.26	3.61	0.58	3.35	0.61	1.59	0.217	1.27	0.200	2.6	0.89	< 0.5	< 0.05	4	< 0.1	0.86	0.41
2.0	9.5	22.6	3.03	14.1	3.60	1.23	3.49	0.58	3.12	0.58	1.52	0.210	1.24	0.196	2.6	0.86	< 0.5	< 0.05	6	< 0.1	0.84	0.31
2.5	9.4	22.1	2.99	13.6	3.48	1.19	3.40	0.58	3.15	0.56	1.51	0.209	1.26	0.189	2.5	0.83	< 0.5	< 0.05	< 3	< 0.1	0.84	0.29
3.0	9.4	22.5	2.98	14.2	3.55	1.19	3.44	0.56	3.05	0.56	1.54	0.208	1.25	0.188	2.4	0.83	0.7	< 0.05	7	< 0.1	0.86	0.30
3.5	10.4	25.0	3.35	15.4	3.70	1.31	3.76	0.61	3.29	0.60	1.58	0.218	1.32	0.204	2.7	0.91	< 0.5	< 0.05	7	< 0.1	1.03	0.32
4.0	10.8	25.5	3.39	15.6	3.86	1.34	3.91	0.62	3.55	0.66	1.72	0.237	1.44	0.217	2.9	0.99	< 0.5	< 0.05	12	< 0.1	0.98	0.36
>4.0	11.4	27.4	3.68	17.3	4.37	1.51	4.32	0.71	3.89	0.72	1.90	0.256	1.50	0.228	3.2	1.09	< 0.5	< 0.05	22	0.1	1.08	0.37
Detection Limit	0.05	0.05	0.01	0.05	0.01	0.005	0.01	0.01	0.01	0.01	0.01	0.005	0.01	0.002	0.1	0.01	0.5	0.05	3	0.1	0.05	0.01

Concentrations in ppm, see Table 4.A-3 for analysis method symbols.

Table 4.A-5. Grain size distribution for comminuted and sorted analog sediments.

Grain size		Cima			Kilauea		
ϕ	μm	weight (g)	frequency (%)	cumulative %	weight (g)	frequency (%)	cumulative %
-3.0	8000.0	0.00	0.00	0.00	1.38	0.20	0.20
-2.5	5656.9	0.00	0.00	0.00	22.31	3.27	3.47
-2.0	4000.0	137.37	11.67	11.67	32.63	4.79	8.26
-1.5	2828.4	186.19	15.81	27.48	135.73	19.91	28.17
-1.0	2000.0	205.68	17.47	44.95	141.48	20.75	48.92
-0.5	1414.2	152.59	12.96	57.91	99.40	14.58	63.50
0.0	1000.0	105.03	8.92	66.84	62.05	9.10	72.60
0.5	707.1	76.25	6.48	73.31	45.91	6.73	79.33
1.0	500.0	54.65	4.64	77.95	34.16	5.01	84.35
1.5	353.6	44.09	3.74	81.70	27.59	4.05	88.39
2.0	250.0	37.31	3.17	84.87	20.74	3.04	91.43
2.5	176.8	28.60	2.43	87.30	13.32	1.95	93.39
3.0	125.0	29.41	2.50	89.80	11.46	1.68	95.07
3.5	88.4	23.70	2.01	91.81	7.55	1.11	96.18
4.0	62.5	32.20	2.74	94.54	7.23	1.06	97.24
> 4.0	< 62.5	64.24	5.46	100.00	18.84	2.76	100.00
total		1177.31	100.00		681.78	100.00	
loss		1.25	0.11		1.47	0.22	

Table 4.A-6. Density measurements for Cima and Kilauea basalt

measurement	number of grains	mass (g)	Δ volume (mL)	ρ density (g/mL)
Cima rock				
1	3	20.53	7.5	2.74
2	3	20.53	7.0	2.93
mean				2.84
Kilauea rock				
1	1	15.70	6.2	2.53
2	1	15.40	6.0	2.57
3	2	11.73	4.5	2.61
4	2	15.39	5.7	2.70
mean				2.60

Table 4.A-7. Conditions for calculating particle threshold friction velocities.

Parameter	Symbol	Units	Value	Source
Interparticle cohesion	A_N		0.0123	Shao and Lu, 2000
Electrostatic force	γ	kg s^{-2}	3 x 10^{-4}	Shao and Lu, 2000
Atmospheric density	ρ	kg m^{-3}	1.54 x 10^{-2} (6.1 mb, 209 K)	Bridges et al., 2010
Gravity	g	m s^{-2}	3.69	Bridges et al., 2010
Particle density	ρ_p	kg m^{-3}	2835 (Cima)	
			2601 (Kilauea)	
			3270 (forsterite)	Roberts et al., 1990
			4390 (fayalite)	Roberts et al., 1990
			2690 (plagioclase)	Roberts et al., 1990

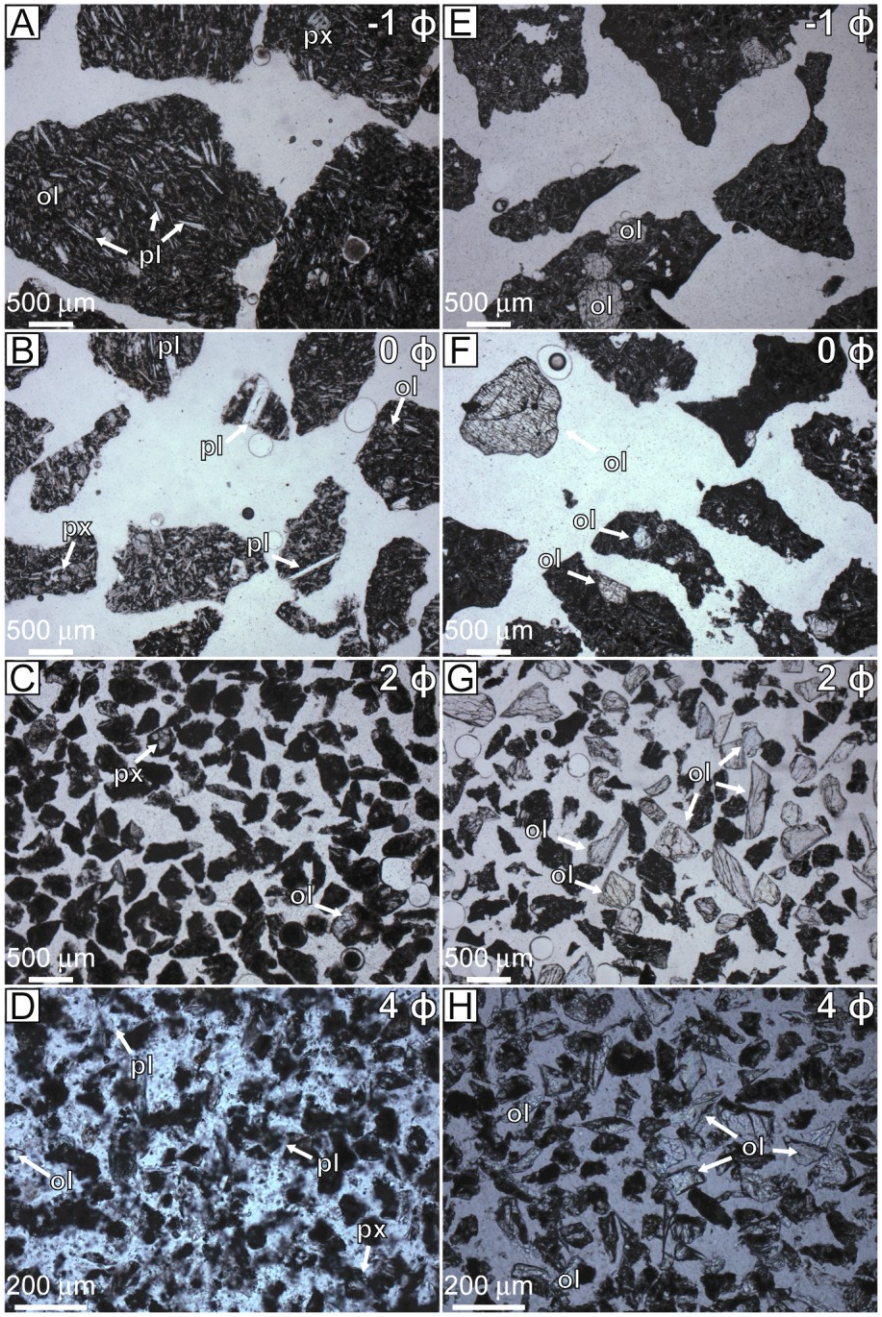

Figure 4.A-1. Plain and crossed polarized photomicrographs of Cima sediment. (A, B) Very fine cobbles (C, D) very coarse sand (E, F) medium sand and (G, H) very fine sand is comprised of rock fragments with few microphenocrysts available for selective sorting.

Vita

Ian McGlynn obtained a Bachelors of Science degree from the Department of Earth and Environmental Sciences at George Washington University and minor in Computer Science, while gaining research experience in LA-ICPMS zircon geochemistry. A Master of Science degree was obtained from the Department of Environmental Sciences at the University of Virginia on a Presidential Fellowship. Research focused on remote sensing and geomorphic studies of aeolian transport and dryland degradation in arid regions of Chihuahuan Desert of New Mexico and Kalahari Desert of Sub-Saharan Africa. Dissertation research conducted at the Department of Earth and Planetary Sciences and Planetary Geosciences Institutes at the University of Tennessee resolved the origin and alteration histories of sediment on the surface of Mars using insights made possible by the NASA Mars Exploration Rovers Spirit and Opportunity. He defended his Doctor of Philosophy degree in Geology in April 2012.